

Doctoral Thesis

Determination of Complex Permittivities of
Two-layer Materials Based on
Hybrid Electromagnetic Methods

March 2016

Doctoral Program in Advanced Electrical, Electronic and
Computer Systems

Graduate School of Science and Engineering

Ritsumeikan University

MOHAMAD Shaiful Bin Abdul Karim

Doctoral Thesis reviewed
by Ritsumeikan University

Determination of Complex Permittivities of Two-layer Materials

Based on Hybrid Electromagnetic Methods

(ハイブリッド電磁界解析法を用いた
二層材料の複素誘電率評価法)

March 2016

2016 年 3 月

Doctoral Program in Advanced Electrical, Electronic and Computer Systems
Graduate School of Science and Engineering
Ritsumeikan University
立命館大学大学院理工学研究科
電子システム専攻博士課程後期課程

MOHAMAD Shaiful Bin Abdul Karim

モハマド シャイフル ビン アブドル カリム

Supervisor: Professor HARAFUJI Kenji

研究指導教員：服藤 憲司 教授

Abstract

An accurate and efficient measurement method is proposed to determine the individual complex permittivities of two-layer materials. This method is a transmission-line method using waveguide and provides frequency-dependent permittivities by measuring only the complex transmission parameters. The sample under test fills only a part of the waveguide cross-section unlike in the case of conventional transmission-line method and the precise machining of the sample is not required. The size of sample is adjusted according to sample loss and permittivity so that an accurate assessment of high-loss material is affordable. The partial loading of sample provides further significant advantage in consort with inhomogeneous field distribution of the waveguide mode. The complex transmission parameter is very influenced by the position of loaded sample in waveguide. This effect can be used advantageously to determine simultaneously the unknown complex permittivities of each layer. This can be realized by using the accurate, efficient and versatile electromagnetic method instead of simple conventional transmission-line theory. The method proposed in this paper is based on hybrid electromagnetic method. The method combines extended spectral domain approach with mode-matching method whose formulation does not include any approximation for simplicity. In the formulation, aperture electric fields or magnetic fields are introduced as source quantities and electromagnetic fields over all regions are related to these source quantities. Numerical method is developed based on Galerkin's procedure to obtain the complex transmission parameters, where source quantities are expressed in terms of basis functions. Thorough investigation is conducted for various materials loaded at different positions in waveguide. The numerical computations are accurate and efficient and the present numerical method has a superiority over conventional methods, such as mode-matching method and finite element method, for use in material assessment.

Based on this hybrid electromagnetic analysis, an effective material assessment algorithm is developed to determine the complex permittivities of each layer of sample. For the material assessment, complex transmission parameters are measured for two different locations and/or orientations of the two-layer sample. The material assessment algorithm uses a bootstrap technique, that is, at first the transmission parameter of one loaded position is used to optimize the permittivity of one layer, and then with this optimized permittivity the transmission parameter of the other loaded position is used to optimize the permittivity of the other layer. These separate processes are repeated alternately until the differences of the measured and calculated transmission parameters fall below the tolerance.

Virtual experiments are performed to examine the material assessment algorithm with various initial values and confirm the robustness of the algorithm. Also a rapid convergence is observed with only several repetition even when the initial value largely mismatches from the true value. Virtual experiments demonstrate the accuracy, versatility, efficiency and robustness of the present method. Virtual experiments also show that the errors due to the uncertainties during material evaluation such as deviation in sample location, length and thickness are less influenced.

Real experiments are performed to evaluate the complex permittivities of two-layer sample at X -band with and without the use of calibration. Actual experiment shows the practicality and accuracy of the proposed method.

Table of Contents

Chapter 1	Introduction	1
Chapter 2	Hybrid Electromagnetic Analytical Theory as a Basis for Material Evaluation	5
2.1	Overview of electromagnetic theory	5
2.2	Analytical model and introduction of source quantities	10
2.3	Electromagnetic field equations in waveguide regions	13
2.4	Electromagnetic fields in homogeneous input and output regions	16
2.5	Electromagnetic fields in inhomogeneous sample holding region	22
2.6	Integral equations on source quantities	30
2.7	Derivation of scattering parameters	32
Chapter 3	Numerical Procedure and Computational Accuracy	33
3.1	Numerical procedure based on Galerkin's method	34
3.2	Basis functions	37
3.3	Investigation of numerical precision	39
Chapter 4	Material Assessment Based on Numerical Analysis	57
4.1	Preliminary investigation into possibility of material assessment	62
4.2	Material estimation algorithm and virtual experiment	66
4.3	Robustness analysis of material estimation	70
4.4	Error analysis of material estimation	75
Chapter 5	Measurement Verification	81
5.1	Sample preparation and measurement setup	82

5.2	Calibration	86
5.3	Measured results	88
5.4	Discussion of applicability of present material assessment	93
Chapter 6	Conclusions	96
References	99
Appendix	102
Appendix 1	Derivation of amplitudes R , T , A_m and D_m	102
Appendix 2	Derivation of eq. (14)	103
Appendix 3	Derivation of determinantal equation of eigenvalues [eq. (22)] and continuity of phase at the boundaries	104
Appendix 4	Orthogonality and normalization of eigenfunction	106
Appendix 5	Derivation of eq. (34)	110

Microwave technologies have been used widely in communication, radar, sensor etc., and even recently find new applications such as in driving support system (self-driving car). These microwave applications use a lot of microwave integrated circuits and planar antennas. The transmission characteristics of microstrips and coplanar lines used in microwave integrated circuit, and radiation characteristics (directivity, gain and operating frequency) of planar antennas are strongly dependent on the electrical property (permittivity) of printed circuit board. Hence, an accurate evaluation technique of electrical property becomes ever more important. Also, microwave technology comes into wider use such as microwave heating [1], food sterilization [2], atomic power [3], microwave chemistry [4], agricultural [5] and medical applications [6]. Materials used in these applications include substantial microwave losses as opposed to low loss materials in conventional applications such as communications, radars and sensors. With the rapid expansion of microwave application, electromagnetic compatibility (EMC) becomes serious problem. Electromagnetic wave absorber is a typical EMC device which can reduce unnecessary reflection wave or suppress unnecessary resonance inside the electronic devices. These devices require the new materials with various (mid-high) losses. The electrical property of a material with loss is represented by complex permittivity. Therefore, an accurate assessment of material's electrical property (permittivity) over wide variety of materials covering from low loss until high loss materials is necessary.

Many measurement methods have been reported during the past few decades for the frequency-dependent electromagnetic properties of lossy materials based on the transmission-line method using waveguides or coaxial lines [7]-[16]. If the transmission-line is filled completely with a homogeneous sample, the reference-plane

dependency of the complex reflection parameter, S_{11} , can be eliminated by using the transmission-line theory and the reference-plane invariant measurement is possible [15], [16]. However, when the measurement method is based on a simple transmission-line theory which assumes a single mode of propagation in the guide, the sample has to be formed precisely to fill up the whole cross-section of the guiding structure [7]-[9]. An air gap between the guide wall and sample or deformation due to the loading of an oversized soft sample gives rise to the higher order mode propagation and causes measurement errors [10]. The transmission-line theory using waveguides is modified to eliminate these problems; the sample fills only a part of the waveguide cross-section, and electromagnetic theory is employed to analyze the scattering characteristics of the partially loaded waveguide [11]-[14]. The materials under test are assumed to be homogeneous in most of these evaluation methods. The permittivity determination of inhomogeneous/layered materials has been treated by various methods including modified sequential quadratic programming and a genetic algorithm [17], the integral equation and Contrast Source Inversion technique [18], iterative method [19], and flanged rectangular waveguides technique [20]. The samples are loaded uniformly over the cross-section in these techniques. In the case of the sample with a lossy and/or high permittivity layer, the measured amplitude of the transmission parameter, S_{21} , becomes very weak and causes the degradation of the accuracy of material assessment. As with single-layered homogeneous samples [11]-[14], partial loading of layered samples in the waveguide cross-section is advantageous for the evaluation of the samples with a lossy layer. If the permittivity of only one of layers is to be evaluated [21], the measurement of the complex S_{21} or S_{11} is sufficient to determine the permittivity. However, the complex S_{11} as well as S_{21} are required to determine the individual complex permittivities of layered sample in the conventional methods. Measurement of complex S_{11} is difficult compared to that of complex S_{21} due to the difficulty of defining the calibration reference to measure phase measurement of S_{11} .

In this paper, an effective measurement method is proposed for assessment of the two-layer sample without measuring S_{11} , where the sample is loaded only partially in the waveguide. The size of sample can be adjusted according to sample loss, therefore the high precision of machining of sample can be sustained and an accurate

evaluation of high-loss material is possible. Also partial loading of the sample is used advantageously to estimate the individual complex permittivities of a two-layer sample. The field intensity in rectangular waveguide is not homogeneous but has its maximum at the center of waveguide and decreases to zero at the guide wall, so the different sample installation leads the different complex transmission even for same sample. The unknown complex permittivity of each layer can be determined simultaneously by measuring the complex transmission (scattering) parameters, S_{21} , of two different locations and/or orientations of the sample and by fitting the measured value to the calculated value with changing the permittivities. Numerical method which relates the scattering parameters to the complex permittivities of the sample must be accurate to evaluate precisely the change in the complex transmission parameters S_{21} of different installations of samples. Therefore numerical method should be based on the electromagnetic field analytical method rather than the simple transmission-line theory. Also numerical method should be versatile and be applicable to the low- and high-dielectric constant material of various sizes (thickness and length) with low- to high-losses. The method must also enhance the efficiency for the iterative process of fitting the parameters to the measured data.

The electromagnetic field analytical method used in this evaluation is a hybrid electromagnetic (EM) method combining the extended spectral domain approach [22], [23] with the mode matching method [24], and the method is extended to analyze two-layer sample loaded in the waveguide [25]. In the formulation of the hybrid EM method, the aperture electric fields have been used as source quantities, and electromagnetic fields in whole region are expressed by these aperture fields. The formulation does not include any approximation for simplicity but in numerical calculation the aperture fields are expressed in terms of a finite number of basis functions. More accurate result is expected by increasing the number of basis functions, but CPU time increases nearly with the square of the number of basis functions. It is required to investigate the convergence characteristic of the number of basis functions and to clarify the necessary number of basis functions for satisfactory accuracy. Aperture magnetic fields are used as source quantities instead of aperture electric fields and scattering electromagnetic fields are performed. Then the error range of numerical

computations is established by combining the results by both aperture electric and magnetic fields.

An effective algorithm is developed based on this accurate EM analysis to determine the complex permittivities of each layer of sample from measurement of complex transmission parameters. Virtual experiments are performed using the material assessment algorithm to investigate the initial value dependence and confirm the robustness of the algorithm. Also virtual experiments based on the accurate EM analysis can be used to investigate the sensitivity of material assessment to deviations in sample location, thickness and width. A measurement system is constructed in the *X*-band and real experiments are performed using sample composed of commercially available materials.

The formulation procedure is explained in chapter II. Chapter III discusses the numerical procedure and computational accuracy. Chapter IV is devoted to the material evaluation procedure based on numerical computations. The validity and robustness of the present method is confirmed by virtual experiments. Actual experimental verifications are given in chapter V. Finally, conclusions and some comments are presented.

Chapter 2 Hybrid Electromagnetic Analytical Theory as a Basis for Material Evaluation

- 2.1 Overview of electromagnetic theory
 - 2.2 Analytical model and introduction of source quantities
 - 2.3 Electromagnetic field equations in waveguide regions
 - 2.4 Electromagnetic fields in homogeneous input and output regions
 - 2.5 Electromagnetic fields in inhomogeneous sample holding region
 - 2.6 Integral equations on source quantities
 - application of remaining boundary conditions-
 - 2.7 Derivation of scattering parameters
-

Chapter 2 Hybrid Electromagnetic Analytical Theory as a Basis for Material Evaluation

2.1 Overview of electromagnetic theory

Fig. 2-1 shows the field intensity of dominant TE_{10} mode of rectangular waveguide where the vector of electric field is represented by circular cone. The field intensity varies greatly in a transverse (x) direction. This inhomogeneous field distribution is used effectively to evaluate material properties. The different complex transmission parameters are observed for the same sample loaded in different location in

the guide (Fig. 2-1). These complex transmission parameters can be used for the simultaneous determination of the electric and magnetic properties of one-layer sample [26], [27] or for the simultaneous determination of the electric properties of each layer of two-layer sample [25] by using a single sample. The determination of material properties is performed by minimizing the difference between the measured and the calculated complex transmission parameters obtained by the electromagnetic fields analysis. Therefore, the accurate and efficient field analytical method is necessary to evaluate the complex transmission parameters of sample loaded in arbitrary position of waveguide. There are many theoretical methods which can be applied to analyze the scattered electromagnetic waves induced by the incident wave. These methods are primarily classified as pure numerical techniques and semi-analytical techniques. Commonly-used numerical techniques are finite-difference time domain method (FDTD) and finite-element method (FEM). The determination of material properties requires the complex transmission parameters at certain frequencies. FEM affords the frequency-dependent transmission parameters, while FDTD performs the time domain analyses and provide only approximate frequency-dependent transmission parameters through fast Fourier transform (FFT). Also fields are interpolated by the continuous shape functions in FEM, while they are evaluated only at discrete lattice points in FDTD. Therefore, FEM solutions are more accurate than those by FDTD. However, these pure numerical techniques require the discretization of entire analytical region into a number of lattices or elements, which requires enormous memory and a lot of CPU time in numerical computation. The workstation with large-capacity memory is required to obtain accurate complex transmission parameters of sample loaded in waveguide as will be shown in chapter 3. An efficient numerical method, which can be performed on

standard PC connected to the network analyzer, is preferable to the material characterization.

Semi-analytical techniques, such as point-matching [28] and mode-matching method [29], require theoretical formulation and coding for specific problems, but do not require fine discretization of the whole analytical region and efficient numerical computations with light numerical burden. Point-matching method satisfy boundary conditions between sub-region only at discrete points, while mode-matching method satisfy continuity conditions over the boundaries and provides more accurate results than those by point-matching method. However, mode-matching method treats the larger matrices with number of eigenfunctions, and the number of eigenfunctions has to

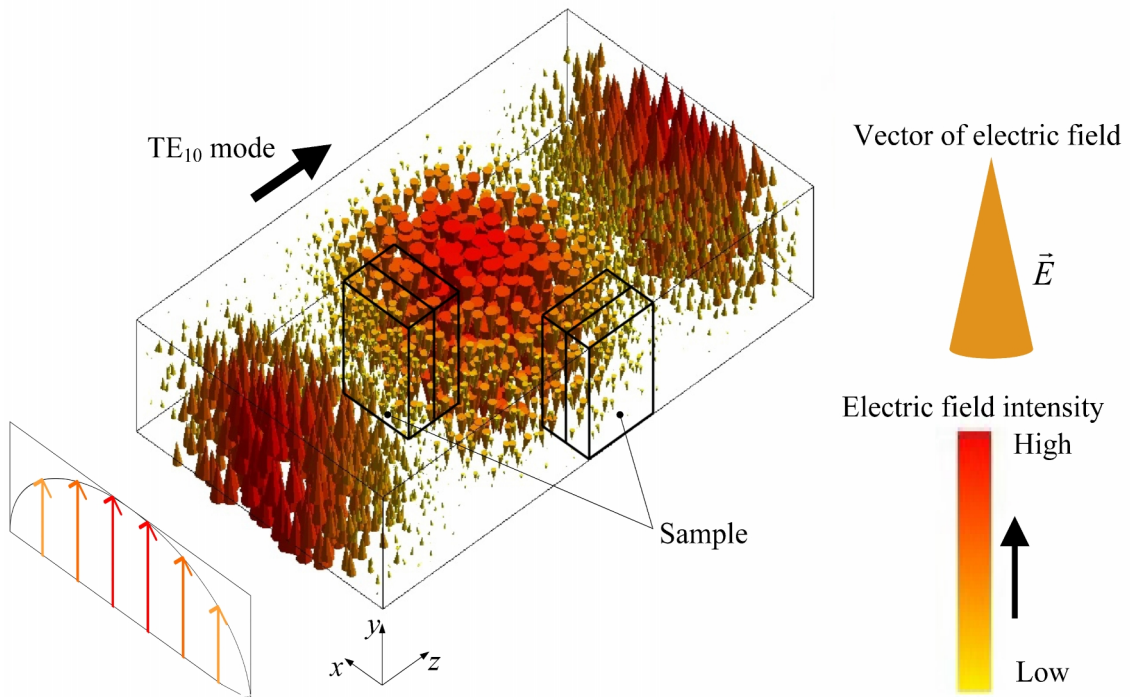


Fig. 2-1 Electric field intensity of dominant TE_{10} mode.

be chosen with extreme care avoiding the problem of ‘relative convergence’ [30], which degrades seriously the versatility of mode-matching method. These conventional electromagnetic methods are not relevant for proposed material evaluation that requires high precision, efficiency, and versatility.

An analytical method was proposed by combining extended spectral domain approach (ESDA) and mode-matching method [24]. In ESDA, the whole analytical space is divided into finite number of regions, and source quantities are introduced at the boundaries between regions. Then fields in each region can be treated independently by resorting to the equivalence theorem of electromagnetic fields [31]. Therefore ESDA is not suffered from the relative convergence, and fields in each region can be expressed accurately in terms of sufficient number of eigenfunction. However, conventional ESDA requires each region to be homogeneous [32] so that eigenfunctions in the region have orthogonality. Inhomogeneous region, such as waveguide partially-loaded with sample material, can be included into ESDA by introducing mode-matching scheme and constructing the bi-orthogonal eigenfunctions in inhomogeneous region. The matrix size used in the method is the number of basis functions which are used to present the source quantities, instead of the number of eigenfunctions and is much smaller than that in the mode-matching method and FEM.

The aperture electric fields have been used as source quantities at boundaries in ESDA and conventional hybrid method [14], [23]-[25], [27], [32]. These aperture fields are expressed in terms of basis functions, and highly accurate scattering parameters can be obtained by increasing the number of basis functions, but the computation time will increase at the square of the number of basis functions. The criteria are required to

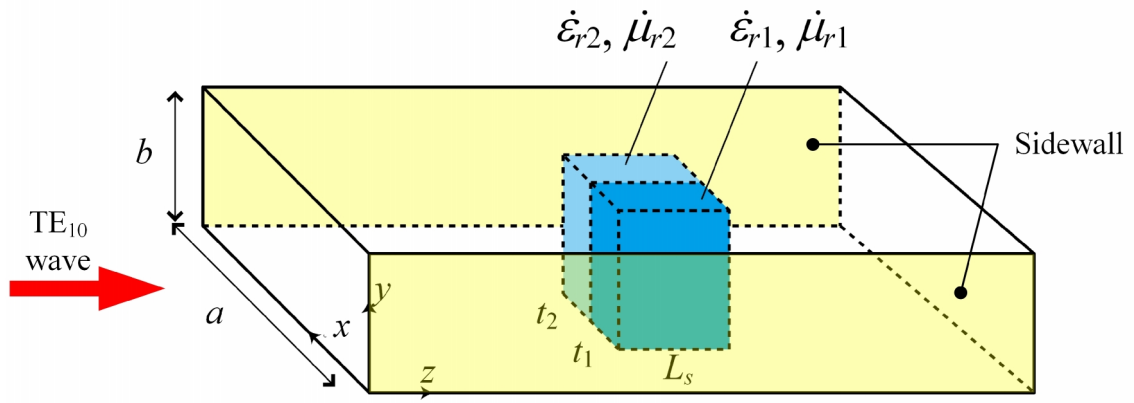
choose the adequate number of basis functions for accurate computation without an excessive computation time. If the aperture magnetic fields are introduced as source quantities instead of the aperture electric fields in conventional methods and complementary formulation procedure is developed, then a true value will be situated between the numerical results by the aperture electric and magnetic fields. Values by both aperture fields would define the error margin of scattering parameters.

In the following, the complementary source quantities, that is aperture electric and magnetic fields, are used in the hybrid electromagnetic formulations. Formulation procedure will be explained for the case with aperture magnetic fields and only resultant formula will be shown for the case with aperture electric fields.

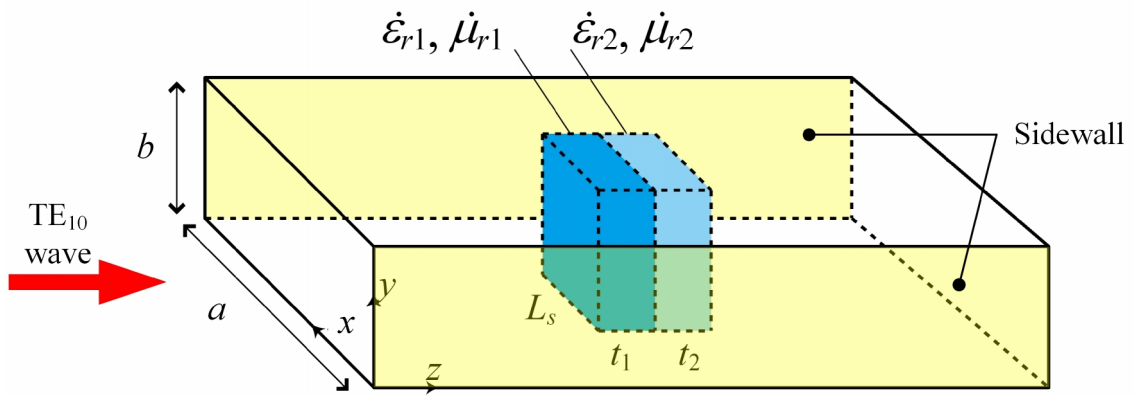
2.2 Analytical model and introduction of source quantities

Fig. 2-2 shows a two-layer sample with thicknesses t_1, t_2 and length L_s is placed in a rectangular waveguide with width a and height b . Each layer of the sample may be dielectric and/or magnetic material and they may be lossless or lossy. Therefore, permittivities and permeabilities of the two layers are complex and denoted by $\hat{\epsilon}_{r1}, \hat{\epsilon}_{r2}$ and $\hat{\mu}_{r1}, \hat{\mu}_{r2}$, respectively. The dominant TE₁₀ wave is incident upon the sample. The formulation procedure is explained in the following for the two-layer sample placed parallel to the sidewalls of waveguide as shown in Fig. 2-2(a) (termed ‘layout A’). The formulation for the sample placed transverse to the waveguide [termed ‘layout B’: Fig. 2-2(b)] could be developed similarly.

The tangential electric or magnetic fields at interfaces between regions are introduced as the source quantities to satisfy the continuities of the electric fields or magnetic fields across the interfaces, respectively. Fig. 2-3(a) shows the aperture magnetic fields $h_a(x)$ and $h_b(x)$ at $z = z_1$ and $z = z_2$, respectively. The whole analytical region is divided into 3 regions, (I) the input waveguide region, (II) the sample holding region $z_1 \leq z \leq z_2 = z_1 + L_s$, and (III) the output waveguide region as shown in Fig. 2-3(b). Each region can be treated independently by using the equivalence theorem [31].



(a) Layout A.



(b) Layout B.

Fig. 2-2 Two-layer sample placed in waveguide.

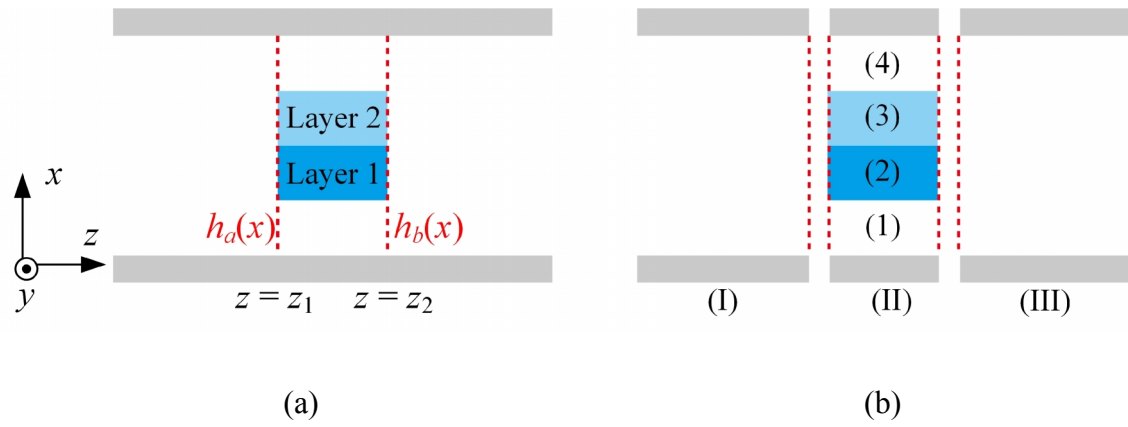


Fig. 2-3 Cross-section of waveguide with two-layer sample. (a) Introduction of aperture magnetic fields. (b) Partitioned regions.

2.3 Electromagnetic field equations in waveguide regions

The electromagnetic fields in each region of waveguide are described by Maxwell's equation

$$\nabla \times \mathbf{E} = -j\omega\dot{\mu}\mathbf{H}, \quad (1-a)$$

$$\nabla \times \mathbf{H} = j\omega\dot{\epsilon}\mathbf{E}, \quad (1-b)$$

where $\dot{\epsilon}$ and $\dot{\mu}$ are complex permittivity and complex permeability, respectively and they are ϵ_0 and μ_0 in the air, and $\dot{\epsilon}_{ri}\epsilon_0$ ($\dot{\epsilon}_{ri}$ is relative permittivity) and $\dot{\mu}_{ri}\mu_0$ ($\dot{\mu}_{ri}$ is relative permeability) in the sample, respectively.

Only the dominant TE₁₀ wave can propagate in the input waveguide. TE₁₀ wave has E_y , H_x , and H_z components and these fields have no variation in y -axis. When the dominant TE₁₀ wave is incident upon the sample, the scattered waves generated are TE modes with E_y , H_x , and H_z with no variation in y -axis. Then the Maxwell's equation can be reduced to

$$-\frac{\partial}{\partial z}E_y = -j\omega\dot{\mu}_iH_x, \quad (2-a)$$

$$\frac{\partial}{\partial x}E_y = -j\omega\dot{\mu}_iH_z, \quad (2-b)$$

$$\frac{\partial}{\partial z}H_x - \frac{\partial}{\partial x}H_z = j\omega\dot{\epsilon}_iE_y. \quad (2-c)$$

H_x and H_z can be expressed in term of E_y by eqs. (2-a) and (2-b), and these relations are substituted into eq. (2-c) to obtain the following partial differential equation (Helmholtz equation) for E_y ,

$$\frac{\partial^2}{\partial x^2} E_y + \frac{\partial^2}{\partial z^2} E_y + \omega^2 \epsilon_i \mu_i E_y = 0. \quad (3)$$

E_y has no y -dependence and can be expressed as

$$E_y(x, z) = \sum_{m=1}^{\infty} X_m(x) \tilde{E}_m(z), \quad (4)$$

where $X_m(x)$ are eigenfunctions which satisfy the boundary conditions at sidewalls of waveguide and interfaces between sample and air. Other field components are expressed as

$$\begin{aligned} H_x(x, z) &= \frac{1}{j\omega\mu_i} \frac{\partial}{\partial z} E_y = \sum_{m=1}^{\infty} X_m(x) \left\{ \frac{1}{j\omega\mu_i} \frac{\partial}{\partial z} \tilde{E}_m(z) \right\} \\ &= \sum_{m=1}^{\infty} X_m(x) \tilde{H}_m(z), \end{aligned} \quad (5-a)$$

$$\tilde{H}_m(z) = \frac{1}{j\omega\mu_i} \frac{\partial}{\partial z} \tilde{E}_m(z), \quad (5-b)$$

$$H_z(x, z) = \frac{-1}{j\omega\mu_i} \frac{\partial}{\partial x} E_y = \sum_{m=1}^{\infty} \left\{ \frac{-1}{j\omega\mu_i} \frac{\partial}{\partial x} X_m(x) \right\} \tilde{E}_m(z). \quad (5-c)$$

In the following, the formulation technique of electromagnetic fields is explained using the aperture magnetic fields as source quantities (Fig. 2-3). The aperture magnetic fields introduced are $h_a(x)$ at the boundary between region (I) and region (II), and $h_b(x)$ at the boundary between region (II) and region (III) as shown in Fig. 2-3(a).

Then electromagnetic fields in each region can be treated independently by resorting to the equivalence theorem of electromagnetic fields, and they can be expressed by the aperture magnetic fields easily in the spectral domain.

2.4 Electromagnetic fields in homogeneous input and output regions

Region (I) and (III) are homogeneous regions, where the fields can be expanded in the series of eigenfunctions $X_m(x)$, that is, simple sinusoidal functions which satisfy the boundary condition at the waveguide sidewalls at $x=0$ and a (Fig. 2-4),

$$X_m(x) = F_m(x) = \sqrt{\frac{2}{a}} \sin\left(\frac{m\pi}{a}x\right); \quad m = 1, 2, 3, \dots \quad (6)$$

These eigenfunctions $F_m(x)$ have the orthogonality,

$$\int_0^a F_m(x) F_n(x) dx = \delta_{mn}. \quad (7)$$

By using these eigenfunctions $F_m(x)$, the electromagnetic fields in region (I) ($z \leq z_1$) can be expressed as

$$\begin{aligned} E_y^{(I)}(x, z) = & E_0 F_1(x) e^{-j\beta_1(z-z_1)} + R E_0 F_1(x) e^{+j\beta_1(z-z_1)} \\ & + \sum_{m=2}^{\infty} A_m E_0 F_m(x) e^{+\gamma_m(z-z_1)}, \end{aligned} \quad (8-a)$$

$$\begin{aligned} H_x^{(I)}(x, z) = & \frac{-\beta_1}{\omega\mu_0} E_0 F_1(x) e^{-j\beta_1(z-z_1)} + R \frac{\beta_1}{\omega\mu_0} E_0 F_1(x) e^{+j\beta_1(z-z_1)} \\ & + \sum_{m=2}^{\infty} A_m E_0 \frac{\gamma_m}{j\omega\mu_0} F_m(x) e^{+\gamma_m(z-z_1)}. \end{aligned} \quad (8-b)$$

In above equations, the first term is the incident wave (TE₁₀ wave) with amplitude E_0 , the second term is the reflected wave (TE₁₀ wave), and the series sum of third term is the higher-order scattered waves in the $-z$ direction. R and A_m represent the complex

reflection coefficient and complex amplitude of higher-order scattered waves, respectively. Since the input and output regions have the same characteristic impedance, the complex reflection coefficient becomes the scattering parameter, S_{11} . The phase constant, β_1 of TE_{10} wave is defined as

$$\beta_1 = \sqrt{\omega^2 \varepsilon_0 \mu_0 - \left(\frac{\pi}{a}\right)^2}. \quad (9)$$

In the input and output regions, the dominant TE_{10} mode is only propagating mode, and all higher-order modes become cutoff modes with a real propagation (attenuation) constants

$$\gamma_m = \alpha_m = \sqrt{\left(\frac{m\pi}{a}\right)^2 - \omega^2 \varepsilon_0 \mu_0} \quad m \geq 2. \quad (10)$$

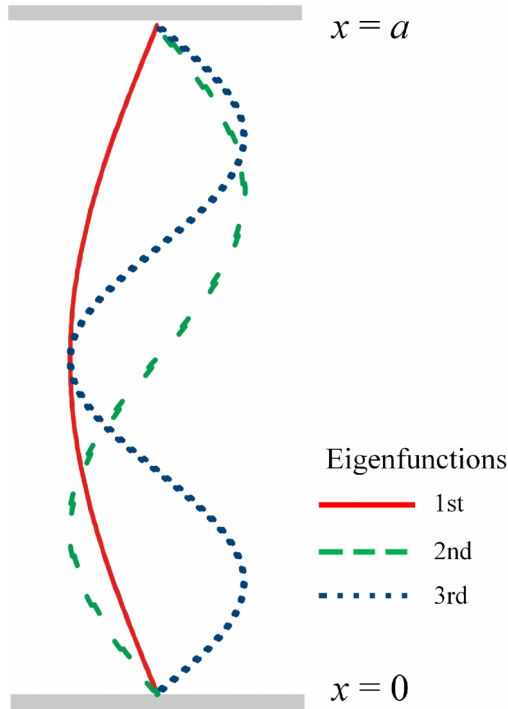


Fig. 2-4 First few eigenfunctions in the input and output waveguide regions.

The electromagnetic fields in output region [region (III): $z \geq z_2$] can be written as

$$E_y^{(III)}(x, z) = TE_0 F_1(x) e^{-j\beta_1(z-z_2)} + \sum_{m=2}^{\infty} D_m E_0 F_m(x) e^{-\gamma_m(z-z_2)}, \quad (11-a)$$

$$H_x^{(III)}(x, z) = -T \frac{\beta_1}{\omega\mu_0} E_0 F_1(x) e^{-j\beta_1(z-z_2)} - \sum_{m=2}^{\infty} D_m E_0 \frac{\gamma_m}{j\omega\mu_0} F_m(x) e^{-\gamma_m(z-z_2)}, \quad (11-b)$$

where the first term is the transmitted TE₁₀ wave, and the series sum of second term represents the higher-order scattered (attenuated) wave in the $+z$ direction. T and D_m represent the complex transmission coefficient and complex amplitude of higher-order attenuated wave, respectively.

The unknown amplitude R , T , A_m and D_m in eqs. (8) and (11) are expressed in terms of the aperture magnetic fields (source fields) easily in spectral domain as follows. The continuity of the magnetic fields at $z = z_1 - 0$, $H_x^{(I)}(x, z = z_1) = h_a(x)$, and at $z = z_2 + 0$, $H_x^{(III)}(x, z = z_2) = h_b(x)$, are imposed and magnetic field expressions in eq. (11-b) and eq. (8-b) are substituted as

$$(-1 + R) \frac{\beta_1}{\omega\mu_0} E_0 F_1(x) + \sum_{m=2}^{\infty} A_m E_0 \frac{\gamma_m}{j\omega\mu_0} F_m(x) = h_a(x), \quad (12-a)$$

$$-T \frac{\beta_1}{\omega\mu_0} E_0 F_1(x) - \sum_{m=2}^{\infty} D_m E_0 \frac{\gamma_m}{j\omega\mu_0} F_m(x) = h_b(x). \quad (12-b)$$

These equations are transformed into spectral domain by using the orthogonality of $F_m(x)$ shown in eq. (7), and the unknown are determined as (Appendix 1)

$$R = \frac{\omega\mu_0}{\beta_1 E_0} \int_0^a h_a(x) F_1(x) dx + 1, \quad (13-a)$$

$$A_m = \frac{j\omega\mu_0}{\gamma_m E_0} \int_0^a h_a(x) F_m(x) dx, \quad (13-b)$$

$$T = \frac{\omega\mu_0}{\beta_1 E_0} \int_0^a h_b(x) F_1(x) dx, \quad (13-c)$$

$$D_m = \frac{j\omega\mu_0}{\gamma_m E_0} \int_0^a h_b(x) F_m(x) dx. \quad (13-d)$$

These coefficients are substituted into eq. (8) and eq. (11), the electromagnetic fields in region (I) and (III) can be expressed as (Appendix 2)

$$E_y^{(I)}(x, z) = E^{inc}(x, z) + \int_0^a Z^{(I)}(x, z | x', z_1) h_a(x') dx', \quad (14-a)$$

$$H_x^{(I)}(x, z) = H^{inc}(x, z) + \int_0^a T_m^{(I)}(x, z | x', z_1) h_a(x') dx', \quad (14-b)$$

$$E_y^{(III)}(x, z) = \int_0^a Z^{(III)}(x, z | x', z_2) h_b(x') dx', \quad (14-c)$$

$$H_x^{(III)}(x, z) = \int_0^a T_m^{(III)}(x, z | x', z_2) h_b(x') dx', \quad (14-d)$$

where $E^{inc}(x, z)$ and $H^{inc}(x, z)$ are given as

$$E^{inc}(x, z) = 2E_0 F_1(x) \cos\{\beta_1(z - z_1)\}, \quad (15-a)$$

$$H^{inc}(x, z) = j2 \frac{\beta_1}{\omega\mu_0} E_0 F_1(x) \sin\{\beta_1(z - z_1)\}. \quad (15-b)$$

$Z^{(i)}(x, z | x', z')$ and $T_m^{(i)}(x, z | x', z')$ are impedance Green's functions and magnetic-transfer Green's functions, respectively,

$$Z^{(I)}(x, z | x', z_1) = \sum_{m=1}^{\infty} \frac{j\omega\mu_0}{\gamma_m} F_m(x) F_m(x') \exp\{\gamma_m(z - z_1)\}, \quad (16-a)$$

$$T_m^{(I)}(x, z | x', z_1) = \sum_{m=1}^{\infty} F_m(x) F_m(x') \exp\{\gamma_m(z - z_1)\}, \quad (16-b)$$

$$Z^{(III)}(x, z | x', z_2) = \sum_{m=1}^{\infty} \frac{j\omega\mu_0}{\gamma_m} F_m(x) F_m(x') \exp\{-\gamma_m(z - z_2)\}, \quad (16-c)$$

$$T_m^{(III)}(x, z | x', z_2) = \sum_{m=1}^{\infty} F_m(x) F_m(x') \exp\{-\gamma_m(z - z_2)\}. \quad (16-d)$$

If the aperture electric fields $e_a(x)$ and $e_b(x)$ are introduced as source quantities (shown in Fig. 2-5) instead of aperture magnetic fields $h_a(x)$ and $h_b(x)$, and the formulation procedure is developed in complementary way, then the unknown in eqs. (8-a) and (11-a) are determined as

$$R = \frac{1}{E_0} \int_0^a e_a(x) F_1(x) dx - 1, \quad (17-a)$$

$$A_m = \frac{1}{E_0} \int_0^a e_a(x) F_m(x) dx, \quad (17-b)$$

$$T = \frac{1}{E_0} \int_0^a e_b(x) F_1(x) dx, \quad (17-c)$$

$$D_m = \frac{1}{E_0} \int_0^a e_b(x) F_m(x) dx, \quad (17-d)$$

and the fields in region (I) and (III) can be expressed as

$$E_y^{(I)}(x, z) = E^{inc}(x, z) + \int_0^a T_e^{(I)}(x, z | x', z_1) e_a(x') dx', \quad (18-a)$$

$$H_x^{(I)}(x, z) = H^{inc}(x, z) + \int_0^a Y^{(I)}(x, z | x', z_1) e_a(x') dx', \quad (18-b)$$

$$E_y^{(III)}(x, z) = \int_0^a T_e^{(III)}(x, z | x', z_2) e_b(x') dx', \quad (18-c)$$

$$H_x^{(III)}(x, z) = \int_0^a Y^{(III)}(x, z | x', z_2) e_b(x') dx', \quad (18-d)$$

where $T_e^{(i)}(x, z | x', z')$ and $Y^{(i)}(x, z | x', z')$ are electric-transfer Green's functions and admittance Green's functions, respectively,

$$T_e^{(I)}(x, z | x', z_1) = \sum_{m=1}^{\infty} \frac{2}{a} F_m(x) F_m(x') \exp\{\gamma_m(z - z_1)\}, \quad (19-a)$$

$$Y^{(I)}(x, z | x', z_1) = \sum_{m=1}^{\infty} \frac{\gamma_m}{j\omega\mu_0} \frac{2}{a} F_m(x) F_m(x') \exp\{\gamma_m(z - z_1)\}, \quad (19-b)$$

$$T_e^{(III)}(x, z | x', z_2) = \sum_{m=1}^{\infty} \frac{2}{a} F_m(x) F_m(x') \exp\{-\gamma_m(z - z_2)\}, \quad (19-c)$$

$$Y^{(III)}(x, z | x', z_2) = \sum_{m=1}^{\infty} \frac{\gamma_m}{j\omega\mu_0} \frac{2}{a} F_m(x) F_m(x') \exp\{-\gamma_m(z - z_2)\}. \quad (19-d)$$

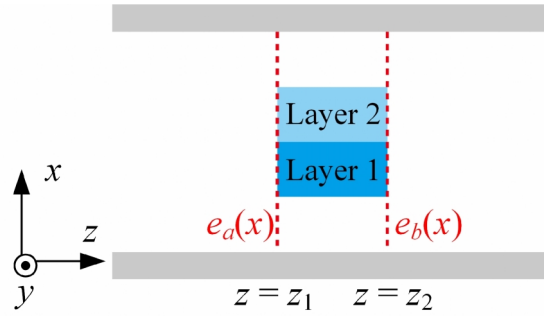


Fig. 2-5 Introduction of aperture electric fields.

2.5 Electromagnetic fields in inhomogeneous sample holding region

The electromagnetic fields in region (II) are also expressed in terms of the eigenfunction $X_m(x) = \Phi_m(x)$ as shown in eqs. (4) and (5),

$$E_y(x, z) = \sum_{m=1}^{\infty} \Phi_m(x) \tilde{E}_m(z), \quad (20-a)$$

$$H_x(x, z) = \sum_{m=1}^{\infty} \Phi_m(x) \tilde{H}_m(z), \quad (20-b)$$

$$\tilde{H}_m(z) = \frac{1}{j\omega\mu_i} \frac{d}{dz} \tilde{E}_m(z). \quad (20-c)$$

However, unlike input and output homogeneous regions [regions (I) and (III)], sample holding region [region (II)] containing sample and air is inhomogeneous and electromagnetic fields in the region cannot be expressed by simple sinusoidal functions. Eigenfunctions in this region can be constructed using mode-matching method. Region (II) is divided further into four subregions (1)-(4) as shown Fig. 2-6, where W_2 and W_3 are the widths of the layered sample [corresponding to t_1 and t_2 in Fig. 2-2(a)], and W_1 and W_4 are the widths of airspace on either side of the sample ($W_1 + W_2 + W_3 + W_4 = a$). Then, by considering the boundary condition at the sidewalls of waveguide, the eigenfunctions in these four subregions can be expressed as

$$\Phi_m(x) = \begin{cases} c_{1m} \frac{\sin(\alpha_{1m}x)}{\cos(\alpha_{1m}W_1)} & (0 \leq x \leq W_1), \\ \frac{c_{21m} \cos\{\alpha_{2m}(x-W_1)\} + c_{22m} \sin\{\alpha_{2m}(x-W_1)\}}{\cos(\alpha_{2m}W_2)} & (W_1 \leq x \leq W_1 + W_2), \\ \frac{c_{31m} \cos\{\alpha_{3m}(x-W_1-W_2)\} + c_{32m} \sin\{\alpha_{3m}(x-W_1-W_2)\}}{\cos(\alpha_{3m}W_3)} & (W_1 + W_2 \leq x \leq a - W_4), \\ c_{4m} \frac{\sin\{\alpha_{4m}(x-a)\}}{\cos(\alpha_{4m}W_4)} & (a - W_4 \leq x \leq a), \end{cases} \quad (21)$$

where α_{1m} , α_{2m} , α_{3m} and α_{4m} are the unknown eigenvalues in each subregion, and c_{1m} , c_{21m} , c_{22m} , c_{31m} , c_{32m} and c_{4m} are unknown coefficients. These unknowns are determined by applying the continuity conditions at boundaries between subregions, which are expressed in matrix form as (Appendix 3)

$$\begin{bmatrix} A \end{bmatrix} \begin{bmatrix} c_{1m} \\ c_{21m} \\ c_{22m} \\ c_{31m} \\ c_{32m} \\ c_{4m} \end{bmatrix} = \mathbf{0}, \quad (22-a)$$

$$[A] = \begin{bmatrix} \tan(\alpha_{1m}W_1) & \frac{-1}{\cos(\alpha_{2m}W_2)} & 0 & 0 & 0 & 0 \\ 0 & 1 & \tan(\alpha_{2m}W_2) & \frac{-1}{\cos(\alpha_{3m}W_3)} & 0 & 0 \\ 0 & 0 & 0 & 1 & \tan(\alpha_{3m}W_3) & \tan(\alpha_{4m}W_4) \\ \frac{\alpha_{1m}}{\mu_1} & 0 & \frac{\alpha_{2m}}{\mu_2} \frac{-1}{\cos(\alpha_{2m}W_2)} & 0 & 0 & 0 \\ 0 & \frac{\alpha_{2m}}{\mu_2} \tan(\alpha_{2m}W_2) & -\alpha_{2m} & 0 & \frac{\alpha_{3m}}{\mu_3} \frac{1}{\cos(\alpha_{3m}W_3)} & 0 \\ 0 & 0 & 0 & \frac{\alpha_{3m}}{\mu_3} \tan(\alpha_{3m}W_3) & -\frac{\alpha_{3m}}{\mu_3} & \frac{\alpha_{4m}}{\mu_4} \end{bmatrix}. \quad (22-b)$$

For these simultaneous equations to have non trivial solution, the determinant of the coefficient matrix $[A]$ should be zero,

$$\det[A] = 0. \quad (23)$$

The unknown eigenvalues α_{1m} , α_{2m} , α_{3m} and α_{4m} are obtained by solving the above equation numerically together with the continuity of phase at the boundaries (Appendix 3)

$$\sqrt{(\alpha_{1m})^2 - \omega^2 \epsilon_1 \mu_1} = \sqrt{(\alpha_{2m})^2 - \omega^2 \epsilon_2 \mu_2} = \sqrt{(\alpha_{3m})^2 - \omega^2 \epsilon_3 \mu_3} = \sqrt{(\alpha_{4m})^2 - \omega^2 \epsilon_4 \mu_4}. \quad (24)$$

Once eigenvalues are obtained, eigenfunctions in each subregions eq. (21) can be determined. These eigenfunctions do not satisfy ordinary orthogonality eq. (7), but satisfy the following biorthogonal relation over the entire sample holding region with the permeabilities in subregions μ_{ri} as the weight function,

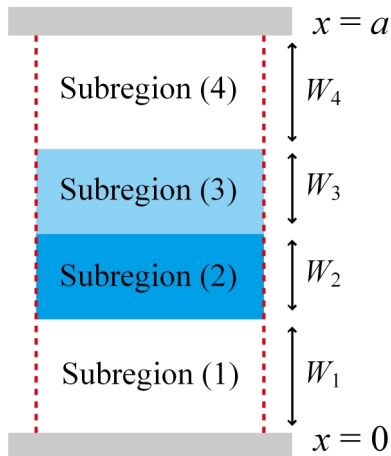


Fig. 2-6 Subregions of sample holding region.

$$\begin{aligned}
\int_0^a \frac{\Phi_m(x) \Phi_n(x)}{\mu_{r_i}} dx &= \int_0^{W_1} \frac{\Phi_m(x) \Phi_n(x)}{\mu_{r_1}} dx + \int_{W_1}^{W_1+W_2} \frac{\Phi_m(x) \Phi_n(x)}{\mu_{r_2}} dx \\
&+ \int_{W_1+W_2}^{a-W_4} \frac{\Phi_m(x) \Phi_n(x)}{\mu_{r_3}} dx + \int_{a-W_4}^a \frac{\Phi_m(x) \Phi_n(x)}{\mu_{r_4}} dx = 0 \quad (m \neq n).
\end{aligned}
\tag{25}$$

The proof of orthogonality $\Phi_m(x)$ is given in Appendix 4. The unknown coefficients c_{1m} , c_{21m} , c_{22m} , c_{31m} , c_{32m} and c_{4m} in eq. (22-a) are the solutions of inhomogeneous equations [eq. (21)] and could be determined to satisfy the normalization,

$$\begin{aligned}
&\int_0^a \frac{\{\Phi_m(x)\}^2}{\mu_{r_i}} dx \\
&= \int_0^{W_1} \frac{\{\Phi_m(x)\}^2}{\mu_{r_1}} dx + \int_{W_1}^{W_1+W_2} \frac{\{\Phi_m(x)\}^2}{\mu_{r_2}} dx + \int_{W_1+W_2}^{a-W_4} \frac{\{\Phi_m(x)\}^2}{\mu_{r_3}} dx + \int_{a-W_4}^a \frac{\{\Phi_m(x)\}^2}{\mu_{r_4}} dx = 1 \\
&\quad (m = n).
\end{aligned}
\tag{26}$$

Fig. 2-7 shows an example of eigenfunctions of two-layer sample loaded in waveguide. Permittivities of each layers are $\epsilon_{r1}=10.0$ and $\epsilon_{r2}=2.0$, respectively, and permeabilities are kept to be 1 for both layers. It should be noted that the eigenfunctions are deformed from sinusoidal functions as electric fields are localized in the layer with higher permittivity.

By utilizing the biorthogonal relation [eq. (25)] of $\Phi_m(x)$, the electromagnetic fields in the inhomogeneous region can be transformed into a spectral domain (transform domain) as in the homogeneous input and output waveguide regions. Also Helmholtz equation [eq. (3)], which is a partial differential equation governing

electromagnetic fields, is transformed into spectral domain and becomes an ordinary differential equation as

$$\frac{d^2}{dz^2} \tilde{E}_m(z) - \left\{ (\alpha_m)^2 - \omega^2 \varepsilon \mu \right\} \tilde{E}_m(z) = 0. \quad (27)$$

The differential equation is solved in the sample-loaded region $z_2 \geq z \geq z_1$, and the general solution of this differential equation can be written by changing variable from (z) to $(z - z_1)$ as

$$\tilde{E}_m(z) = P_m \frac{\cosh\{\gamma_m(z - z_1)\}}{\cosh(\gamma_m L_s)} + Q_m \frac{\sinh\{\gamma_m(z - z_1)\}}{\sinh(\gamma_m L_s)}, \quad (28)$$

where P_m and Q_m are unknown coefficients and γ_m is propagation constant in region (II),

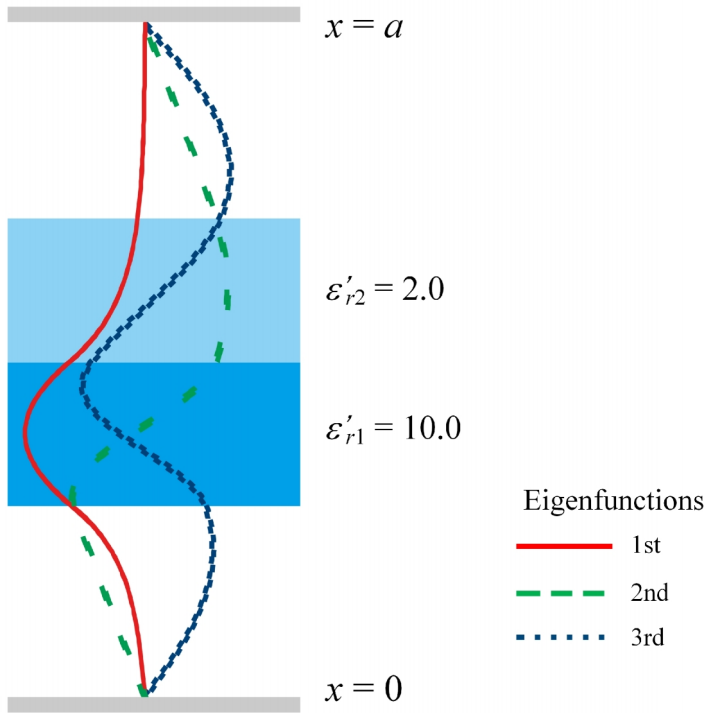


Fig. 2-7 First few eigenfunctions in the sample-loaded region.

$$\gamma_m = \sqrt{(\alpha_m)^2 - \omega^2 \varepsilon_i \mu_i} . \quad (29)$$

$\tilde{H}_m(z)$ is the transform of magnetic field as shown in (20-c) and obtained as

$$\begin{aligned} \tilde{H}_m(z) &= \frac{1}{j\omega\dot{\mu}_i} \frac{d}{dz} \tilde{E}_m(z) \\ &= \frac{\gamma_m}{j\omega\dot{\mu}_i} \left[P_m \frac{\sinh\{\gamma_m(z-z_1)\}}{\cosh(\gamma_m L_s)} + Q_m \frac{\cosh\{\gamma_m(z-z_1)\}}{\sinh(\gamma_m L_s)} \right]. \end{aligned} \quad (30)$$

Unknown coefficients P_m and Q_m in eqs. (28) and (30) can be determined by applying the boundary conditions at input $z = z_1$ and output $z = z_2$ of region (II).

The boundary conditions in space domain (before transformation) are

$$H_x^{(2)}(x, z = z_1 + 0) = \sum_{m=1}^{\infty} \Phi_m(x) \tilde{H}_m(z_1 + 0) = h_a(x) \quad \text{at input } z = z_1, \quad (31\text{-a})$$

$$H_x^{(2)}(x, z = z_2 - 0) = \sum_{m=1}^{\infty} \Phi_m(x) \tilde{H}_m(z_2 - 0) = h_b(x) \quad \text{at output } z = z_2, \quad (31\text{-b})$$

and they are transformed by using the biorthogonal relation [eq. (25)] into spectral domain as

$$\tilde{H}_m(t = z_1 + 0) = \int_0^a h_a(x) \frac{\Phi_m(x)}{\mu_i} dx, \quad (32\text{-a})$$

$$\tilde{H}_m(t = z_2 - 0) = \int_0^a h_b(x) \frac{\Phi_m(x)}{\mu_i} dx. \quad (32\text{-b})$$

By substituting eq. (30) into above eqs. (32), P_m and Q_m can be obtained as,

$$P_m = \frac{j\omega\dot{\mu}_i}{\gamma_m} \frac{\cosh(\gamma_m L_s)}{\sinh(\gamma_m L_s)} \left[-\cosh(\gamma_m L_s) \int_0^a h_a(x) \frac{\Phi_m(x)}{\mu_i} dx + \int_0^a h_b(x) \frac{\Phi_m(x)}{\mu_i} dx \right], \quad (33-a)$$

$$Q_m = \sinh(\gamma_m L_s) \frac{j\omega\dot{\mu}_i}{\gamma_m} \int_0^a h_a(x) \frac{\Phi_m(x)}{\mu_i} dx, \quad (33-b)$$

where L_s is the sample length (Fig. 2-2). Then, by substituting P_m and Q_m into eqs. (28) and (30) and making the inverse transformation into space domain, the electric and magnetic fields in sample holding region [region (II)] can be related to the aperture magnetic fields as (Appendix 5)

$$E_y^{(II)}(x, z) = -\int_0^a Z^{(II)}(x, z | x', z_1) \frac{h_a(x')}{\mu_i} dx' + \int_0^a Z^{(II)}(x, z | x', z_2) \frac{h_b(x')}{\mu_i} dx', \quad (34-a)$$

and

$$H_x^{(II)}(x, z) = \int_0^a T_m^{(II)}(x, z | x', z_1) \frac{h_a(x')}{\mu_i} dx' + \int_0^a T_m^{(II)}(x, z | x', z_2) \frac{h_b(x')}{\mu_i} dx', \quad (34-b)$$

respectively, where $Z^{(II)}$ and $T_m^{(II)}$ are impedance and magnetic-transfer Green's functions in region (II), respectively,

$$Z^{(II)}(x, z | x', z') = \sum_{m=1}^{\infty} \frac{j\omega\dot{\mu}_i}{\gamma_m} \frac{\cosh\{\gamma_m (L_s - |z - z'|)\}}{\sinh(\gamma_m L_s)} \Phi_m(x) \Phi_m(x'), \quad (35-a)$$

$$T_m^{(II)}(x, z | x', z') = \sum_{m=1}^{\infty} \frac{\sinh\{\gamma_m (L_s - |z - z'|)\}}{\sinh(\gamma_m L_s)} \Phi_m(x) \Phi_m(x'). \quad (35-b)$$

When the aperture electric fields $e_a(x)$ and $e_b(x)$ are used as source quantities instead of aperture magnetic fields $h_a(x)$ and $h_b(x)$, the electric and magnetic fields in region (II) can be expressed as,

$$E_y^{(II)}(x, z) = \int_0^a T_e^{(II)}(x, z | x', z_1) \frac{e_a(x')}{\mu_i} dx' + \int_0^a T_e^{(II)}(x, z | x', z_2) \frac{e_b(x')}{\mu_i} dx', \quad (36-a)$$

$$H_x^{(II)}(x, z) = -\int_0^a Y^{(II)}(x, z | x', z_1) \frac{e_a(x')}{\mu_i} dx' + \int_0^a Y^{(II)}(x, z | x', z_2) \frac{e_b(x')}{\mu_i} dx', \quad (36-b)$$

where $T_e^{(II)}$ and $Y^{(II)}$ are electric-transfer and admittance Green's functions in region (II), respectively

$$T_e^{(II)}(x, z | x', z') = \sum_{m=1}^{\infty} \frac{\sinh\{\gamma_m(L_s - |z - z'|)\}}{\sinh(\gamma_m L_s)} \Phi_m(x) \Phi_m(x'), \quad (37-a)$$

$$Y^{(II)}(x, z | x', z') = \sum_{m=1}^{\infty} \frac{\gamma_m}{j\omega\mu_i} \frac{\cosh\{\gamma_m(L_s - |z - z'|)\}}{\sinh(\gamma_m L_s)} \Phi_m(x) \Phi_m(x'). \quad (37-b)$$

2.6 Integral equations on source quantities

In sec. 2.3 and sec 2.4, the electromagnetic fields in whole region are expressed in terms of aperture magnetic or electric fields in sec. 2.4 and 2.5. If an aperture magnetic fields is introduced at the interface and the tangential magnetic fields of both side of the interface are equated with the aperture magnetic field, then the continuity of tangential magnetic fields is certified at the interface as shown in Fig. 2-8. Therefore, the remaining boundary conditions to be satisfied are the continuity of tangential electric fields at the interface. Applying these remaining conditions to the field expressions of eqs. (14-a), (14-c), (34-a), the integral equations on the aperture magnetic fields can be obtained as

$$\begin{aligned} E^{inc}(x, z_1) + \int_0^a Z^{(I)}(x, z_1 | x', z_1) h_a(x') dx' \\ = - \int_0^a Z^{(II)}(x, z_1 | x', z_1) \frac{h_a(x')}{\mu_i} dx' + \int_0^a Z^{(II)}(x, z_1 | x', z_2) \frac{h_b(x')}{\mu_i} dx', \end{aligned} \quad (38-a)$$

$$\begin{aligned} - \int_0^a Z^{(II)}(x, z_2 | x', z_1) \frac{h_a(x')}{\mu_i} dx' + \int_0^a Z^{(II)}(x, z_2 | x', z_2) \frac{h_b(x')}{\mu_i} dx' \\ = \int_0^a Z^{(III)}(x, z_2 | x', z_2) h_b(x') dx'. \end{aligned} \quad (38-b)$$

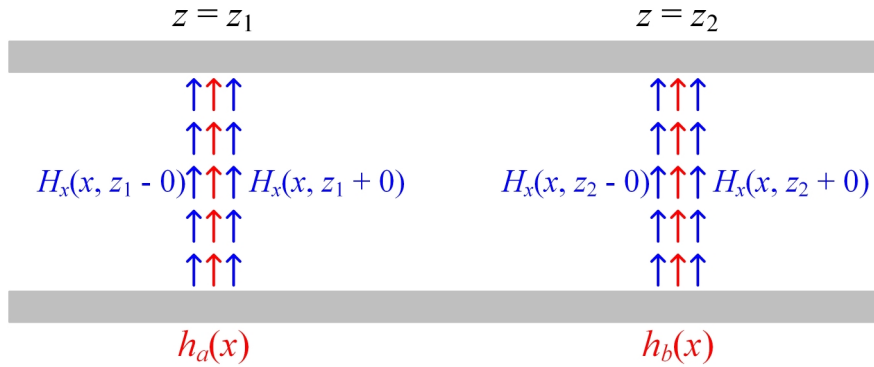


Fig. 2-8 Continuity of tangential magnetic fields.

When the aperture electric fields $e_a(x)$ and $e_b(x)$ are used in the formulation, the integral equations on the aperture electric fields are obtained as,

$$H^{inc}(x, z_1) + \int_0^a Y^{(I)}(x, z | x', z_1) e_a(x') dx' \\ = - \int_0^a Y^{(II)}(x, z | x', z_1) e_a(x') dx' + \int_0^a Y^{(II)}(x, z | x', z_2) e_b(x') dx', \quad (39-a)$$

$$- \int_0^a Y^{(II)}(x, z | x', z_1) e_a(x') dx' + \int_0^a Y^{(II)}(x, z | x', z_2) e_b(x') dx' \\ = \int_0^a Y^{(III)}(x, z | x', z_1) e_b(x') dx'. \quad (39-b)$$

These integral equations can be solved by applying Galerkin's procedure and the unknown aperture magnetic or electric fields are determined. Numerical procedure based on the Galerkin's procedure will be explained in chapter 3.

2.7 Derivation of scattering parameters

Once aperture magnetic or electric fields are determined, the complex reflection coefficient R and transmission coefficient T are obtained by eqs. (13) or (17). When input and output ports are located at L_1 and L_2 away from the sample (Fig. 2-9), then the scattering parameters, S_{11} observed at input port, and S_{21} at output port are obtained as

$$S_{11} = R e^{-j2\beta_1 L_1} = \left\{ \frac{j\omega\mu_0}{\beta_1 E_0} \int_0^a h_a(x) F_1(x) dx + 1 \right\} e^{-j2\beta_1 L_1}, \quad (40-a)$$

$$S_{21} = T e^{-j\beta_1(L_1+L_2)} = \frac{j\omega\mu_0}{\beta_1 E_0} \int_0^a h_b(x) F_1(x) dx e^{-j\beta_1(L_1+L_2)}, \quad (40-b)$$

for aperture magnetic fields, and

$$S_{11} = R e^{-j2\beta_1 L_1} = \left\{ \frac{1}{E_0} \int_0^a e_a(x) F_1(x) dx - 1 \right\} e^{-j2\beta_1 L_1}, \quad (41-a)$$

$$S_{21} = T e^{-j\beta_1(L_1+L_2)} = \frac{1}{E_0} \int_0^a e_b(x) F_1(x) dx e^{-j\beta_1(L_1+L_2)}, \quad (41-b)$$

for aperture electric fields.

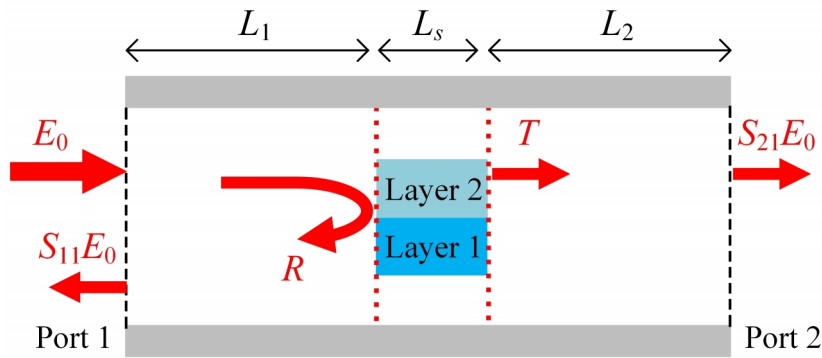


Fig. 2-9 Waveguide with input and output ports.

Chapter 3 Numerical Procedure and Computational Accuracy

3.1 Numerical procedure based on Galerkin's method

3.2 Basis functions

3.3 Investigation of numerical precision

Chapter 3 Numerical Procedure and Computational Accuracy

In previous chapter, the hybrid electromagnetic analytical method was presented by combining extended spectral domain approach (ESDA) and mode-matching method. This analytical method does not include any approximation for simplicity and the method is able to evaluate the scattering characteristics of wide variety of two-layer samples with the high or low permittivities, and high or low losses. The sample size may be electrically large or small. Electromagnetic fields in whole region are expressed in terms of aperture magnetic or electric fields in this method. These unknown aperture fields are determined by applying Galerkin's procedure to integral eqs. (38) and (39). In this chapter, a numerical procedure for calculating the scattering parameters is explained. The validation and accuracy of the numerical procedure is investigated by using the complementary source fields, which are aperture magnetic or electric fields.

3.1 Numerical procedure based on Galerkin's method

The integral equations on aperture magnetic fields [eq. (38)] or electric fields [eq. (39)] are solved by Galerkin's method. In the following the numerical procedure is explained for the integral equations on aperture magnetic fields $h_i(x)$

$$\begin{aligned} E^{inc}(x, z_1) + \int_0^a Z^{(I)}(x, z_1 | x', z_1) h_a(x') dx' \\ = - \int_0^a Z^{(II)}(x, z_1 | x', z_1) \frac{h_a(x')}{\mu_i} dx' + \int_0^a Z^{(II)}(x, z_1 | x', z_2) \frac{h_b(x')}{\mu_i} dx', \end{aligned} \quad (42-a)$$

$$\begin{aligned} - \int_0^a Z^{(II)}(x, z_2 | x', z_1) \frac{h_a(x')}{\mu_i} dx' + \int_0^a Z^{(II)}(x, z_2 | x', z_2) \frac{h_b(x')}{\mu_i} dx' \\ = \int_0^a Z^{(III)}(x, z_2 | x', z_2) h_b(x') dx'. \end{aligned} \quad (42-b)$$

The unknown aperture magnetic fields $h_i(x)$ are expanded in terms of the adequate basis functions $\xi_{rj}(x)$ as

$$h_a(x) = \sum_{j=1}^N a_j \xi_j(x), \quad (43-a)$$

$$h_b(x) = \sum_{j=1}^N b_j \xi_j(x), \quad (43-b)$$

where a_j, b_j are the unknown parameters. After substitution of these aperture fields, the integral eq. (42) can be expressed as

$$\begin{aligned} E^{inc}(x, z_1) + \sum_{j=1}^N a_j \int_0^a Z^{(I)}(x, z_1 | x', z_1) \xi_j(x') dx' \\ = - \sum_{j=1}^N a_j \int_0^a Z^{(II)}(x, z_1 | x', z_1) \frac{\xi_j(x')}{\mu_i} dx' + \sum_{j=1}^N b_j \int_0^a Z^{(II)}(x, z_1 | x', z_2) \frac{\xi_j(x')}{\mu_i} dx', \end{aligned} \quad (44-a)$$

$$\begin{aligned}
& -\sum_{j=1}^N a_j \int_0^a Z^{(II)}(x, z_2 | x', z_1) \frac{\xi_j(x')}{\mu_i} dx' + \sum_{j=1}^N b_j \int_0^a Z^{(II)}(x, z_2 | x', z_2) \frac{\xi_j(x')}{\mu_i} dx' \\
& = \sum_{j=1}^N b_j \int_0^a Z^{(III)}(x, z_2 | x', z_2) \xi_j(x') dx'. \quad (44-b)
\end{aligned}$$

When eqs. (44-a) and (44-b) are multiplied by $\xi_i(x)$ and integrated over the aperture surface $(0, a)$, they can be written as

$$\begin{aligned}
& \int_0^a \xi_i(x) E^{inc}(x, z_1) dx + \sum_{j=1}^N a_j \int \int_0^a \xi_i(x) Z^{(I)}(x, z_1 | x', z_1) \xi_j(x') dx' dx \\
& = -\sum_{j=1}^N a_j \int \int_0^a \xi_i(x) Z^{(II)}(x, z_1 | x', z_1) \frac{\xi_j(x')}{\mu_i} dx' dx \\
& \quad + \sum_{j=1}^N b_j \int \int_0^a \xi_i(x) Z^{(II)}(x, z_1 | x', z_2) \frac{\xi_j(x')}{\mu_i} dx' dx, \quad (45-a)
\end{aligned}$$

$$\begin{aligned}
& -\sum_{j=1}^N a_j \int \int_0^a \xi_i(x) Z^{(II)}(x, z_2 | x', z_1) \frac{\xi_j(x')}{\mu_i} dx' dx \\
& \quad + \sum_{j=1}^N b_j \int \int_0^a \xi_i(x) Z^{(II)}(x, z_2 | x', z_2) \frac{\xi_j(x')}{\mu_i} dx' dx \\
& = \sum_{j=1}^N b_j \int \int_0^a \xi_i(x) Z^{(III)}(x, z_2 | x', z_2) \xi_j(x') dx' dx, \quad (45-b)
\end{aligned}$$

$$i=1, 2, \dots, N.$$

The above simultaneous equations with $2N$ unknowns a_j, b_j are expressed in matrix form as

$$\begin{bmatrix} G_{11} & G_{12} \\ G_{21} & G_{22} \end{bmatrix} \begin{bmatrix} a \\ b \end{bmatrix} = \begin{bmatrix} I \\ 0 \end{bmatrix}, \quad (46)$$

where a, b and I are N -dimensional vectors with components a_j, b_j and

$$I_i = -\int_0^a \xi_i(x) E^{inc}(x, z_1) dx, \quad (47)$$

respectively. Matrix elements of G_{mn} are

$$\begin{aligned} [G_{11}]_{ij} = & \int \int_0^a \xi_i(x) Z^{(I)}(x, z_1 | x', z_1) \xi_j(x') dx' dx \\ & - \int \int_0^a \xi_i(x) Z^{(II)}(x, z_1 | x', z_1) \frac{\xi_j(x')}{\mu_i} dx' dx, \end{aligned} \quad (48-a)$$

$$[G_{12}]_{ij} = -\int \int_0^a \xi_i(x) Z^{(II)}(x, z_1 | x', z_2) \frac{\xi_j(x')}{\mu_i} dx' dx, \quad (48-b)$$

$$[G_{21}]_{ij} = -\int \int_0^a \xi_i(x) Z^{(II)}(x, z_2 | x', z_1) \frac{\xi_j(x')}{\mu_i} dx' dx, \quad (48-c)$$

$$\begin{aligned} [G_{22}]_{ij} = & -\int \int_0^a \xi_i(x) Z^{(II)}(x, z_2 | x', z_2) \frac{\xi_j(x')}{\mu_i} dx' dx \\ & + \int \int_0^a \xi_i(x) Z^{(III)}(x, z_2 | x', z_2) \xi_j(x') dx' dx, \end{aligned} \quad (48-d)$$

The similar simultaneous equations can be derived from the integral equations on aperture electric fields [eq. (39)]. The integrals in eqs. (38) and (39) are evaluated analytically and simultaneous equations [eq. (45)] can be solved once the proper basis functions $\xi_i(x)$ are selected. The matrix size in this method is the order of the total number of basis functions as shown in eq. (22-a) which is a few hundred at most, and the size is much smaller than that of the conventional mode-matching method [29], whose matrix size is the order of the number of the eigenfunctions. It is required several thousand eigenfunctions to express the electromagnetic fields as accurately as the present method.

3.2 Basis functions

The flexible sub-sectional basis functions are utilized to express the aperture fields in this work to adapt wide varieties of objects, lossless or lossy materials, loaded in arbitrary position of waveguide. For example, the aperture magnetic fields of a two-layer sample in the waveguide can be expressed in terms of rooftop functions expressed as (Fig. 3-1)

$$\begin{aligned}\xi_j(x) &= \frac{1}{\Delta x_1} \left\{ \Delta x_1 + (x - x_j) \right\} & (x_j - \Delta x_1 \leq x \leq x_j) \\ &= \frac{1}{\Delta x_2} \left\{ \Delta x_2 - (x - x_j) \right\} & (x_j < x < x_j + \Delta x_2).\end{aligned}\quad (49)$$

When these rooftop functions are used as basis functions, all integrals included in eq.

(48) are evaluated analytically. Integrals in regions (I) and (III) are $\int_0^a F_m(x) \xi_j(x) dx$

and integrals in region (II) are $\int_0^a \Phi_m(x) \xi_j(x) dx$, and a typical instance is

$$\begin{aligned}& \int_0^a \sin(\alpha_n x) \xi_j(x) dx \\ &= \frac{1}{\Delta x_1} \int_{x_j - \Delta x_1}^{x_j} \sin(\alpha_n x) \left\{ \Delta x_1 + (x - x_j) \right\} dx + \frac{1}{\Delta x_2} \int_{x_j}^{x_j + \Delta x_2} \sin(\alpha_n x) \left\{ \Delta x_2 - (x - x_j) \right\} dx \\ &= \frac{1}{\Delta x_1} \left[\sin(\alpha_n x_j) - \sin\{\alpha_n (x_j - \Delta x_1)\} - \frac{1}{\alpha_n} \Delta x_1 \cos(\alpha_n x_j) + \frac{1}{\alpha_n} \right] \\ &+ \frac{1}{\Delta x_2} \left[-\sin\{\alpha_n (x_j + \Delta x_2)\} + \sin(\alpha_n x_j) - \frac{1}{\alpha_n} 2\Delta x_1 \cos\{\alpha_n (x_j + \Delta x_2)\} + \frac{1}{\alpha_n} \Delta x_1 \cos(\alpha_n x_j) \right].\end{aligned}\quad (50)$$

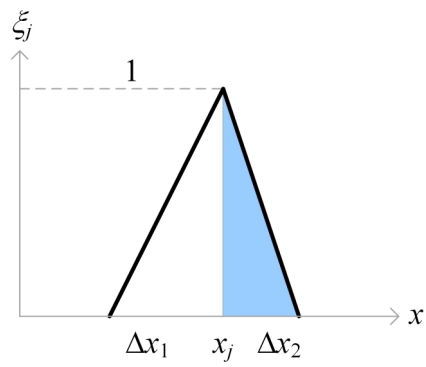
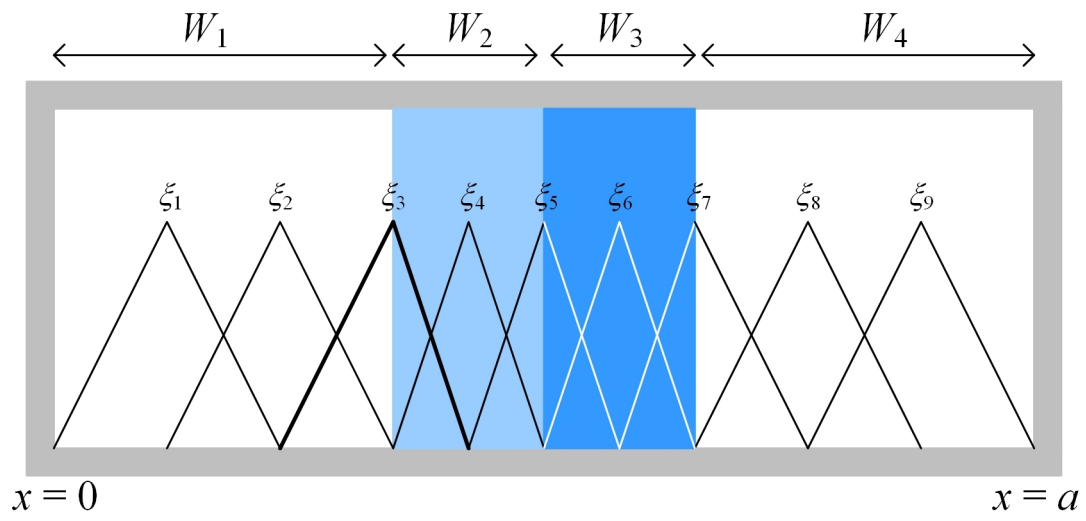


Fig. 3-1 Rooftop functions used as basis functions.

3.3 Investigation of numerical precision

In the numerical computation, unknown aperture fields are expressed in terms of a finite number of basis functions. More accurate result is expected by increasing the number of basis functions, but CPU time and memory requirement associated with the computation increase nearly with the square of the number of basis functions. It is required to investigate the convergence characteristic of the number of basis functions and to clarify the necessary number of basis functions for satisfactory accuracy. Convergence test would be easy for problems with exact solutions, but it is not possible in general to get the exact solution for scattering parameters of sample-loaded waveguide. Therefore, alternative procedures are utilized for the convergence test in this work. Two types of numerical computations are performed by dual formulations with the complementary source quantities, i.e., aperture electric and magnetic fields explained in chapter 2. The determining equations of aperture magnetic fields [eq. (38)] include the impedance Green's functions, while those of aperture electric fields [eq. (39)] include the admittance Green's functions. Therefore, the unknown exact value is expected to locate between the values calculated by these two dual formulations, and margin of error could be obtained numerically.

First, simple structure is analyzed by the present method in Fig. 3-2(a), where one-layer sample occupies the whole cross-section of the waveguide. The complex transmission parameter \dot{S}_{21} of the sample with the complex permittivity $\dot{\epsilon}_r = 8.0 - j2.0$ and permeability $\dot{\mu}_r = 2.0 - j0.7$ is calculated by using both source quantities with the number of basis functions up to 1000 to test convergence. Fig. 3-2(b)

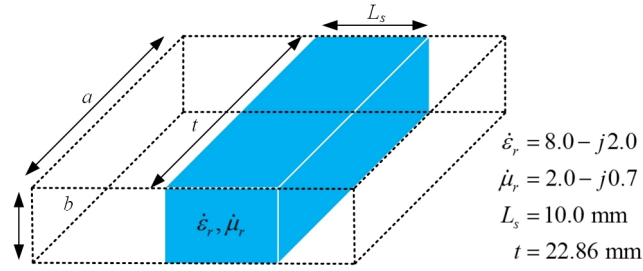
and (c) show the convergence of $|\dot{S}_{21}|$ and $\angle \dot{S}_{21}$, respectively. The phase of complex transmission parameter $\angle \dot{S}_{21}$ is evaluated by the phase delay of the complex transmission parameter of loaded waveguides with respect to the unloaded cases $\angle \dot{S}_{21} = \angle \dot{S}_{21}^L - \angle \dot{S}_{21}^U$. The rigorous analysis is available by applying the simple transmission-line theory to this structure and the exact value is also included in the figure.

If transmission parameter would be real number and could be presented in a stationary expression, then numerical values of transmission parameter are always larger or smaller than the exact value. However, the transmission parameter \dot{S}_{21} of the present case is complex number and cannot be presented in a stationary expression, so the numerical value of its magnitude $|\dot{S}_{21}|$ and phase $\angle \dot{S}_{21}$ do not constitute the upper and lower bound of true value. Therefore, the calculated values of $|\dot{S}_{21}|$ and $\angle \dot{S}_{21}$ suffer a big fluctuation for insufficient number of basis functions ($N < 10$). Especially the value of $|\dot{S}_{21}|$ computed using the aperture electric fields as source quantities fluctuates up and down around the exact value [see Fig. 3-2(b)]. However, when the number of basis functions is increased sufficiently to represent the aperture fields ($N \geq 10$), the values computed by both source quantities converge monotonously with the number of basis functions N . $|\dot{S}_{21}|$ and $\angle \dot{S}_{21}$ computed using aperture electric fields are approaching the exact value from above, while those computed using aperture magnetic fields are approaching from below, and the exact values are limited between the values computed by both source quantities. This can be explained as follows. The complementary aperture electric and magnetic fields are used as source quantities, also dual formulations are developed for two different aperture fields. Formulation based on

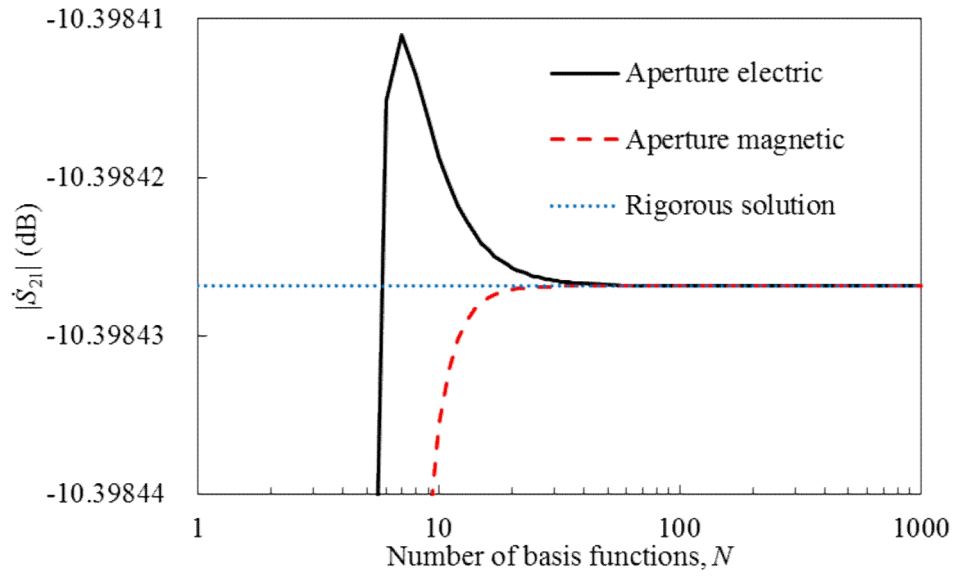
aperture electric fields leads to the integral equation [eq. (39)] with the kernels formed by admittance Green's functions $Y^{(i)}(x, z | x', z')$ [2], while formulation based on aperture magnetic fields leads to the integral kernels formed by impedance Green's functions $Z^{(i)}(x, z | x', z')$. When numerical values are obtained by these dual approaches, one gives larger and the other gives smaller values than exact value.

The differences of $|\dot{S}_{21}|$ between rigorous solution and the value computed by present method are less than $5.86 \times 10^{-6} \%$ using aperture electric fields with $N \geq 25$ and $7.69 \times 10^{-7} \%$ using aperture magnetic fields with $N \geq 25$, which matches until eighth digit. The corresponding difference of $\angle \dot{S}_{21}$ is less than $9.88 \times 10^{-4} \%$ and $4.02 \times 10^{-6} \%$, respectively, which matches fifth digit. These differences monotonously decrease until $N = 1000$, and an excellent convergence (9 digit accuracy) can be observed. The distributions of aperture electric and magnetic fields are same $(\sin(\frac{\pi}{a}x))$ for the sample which occupies the whole cross-section of the waveguide, but numerical values using aperture magnetic fields converge faster than those using aperture electric fields. The difference in convergence comes from the fact that the scattering fields are TE modes with three field components, E_y , H_x , and H_z , that is magnetic field has two components (H_x, H_z) , while electric field has only one component (E_y) . When aperture electric fields are used as source quantities and they are approximated in terms of finite number of basis functions, order of approximation of electric field is the same as that of aperture electric fields. When aperture magnetic fields are used as source quantities, only one component of magnetic field H_x has the

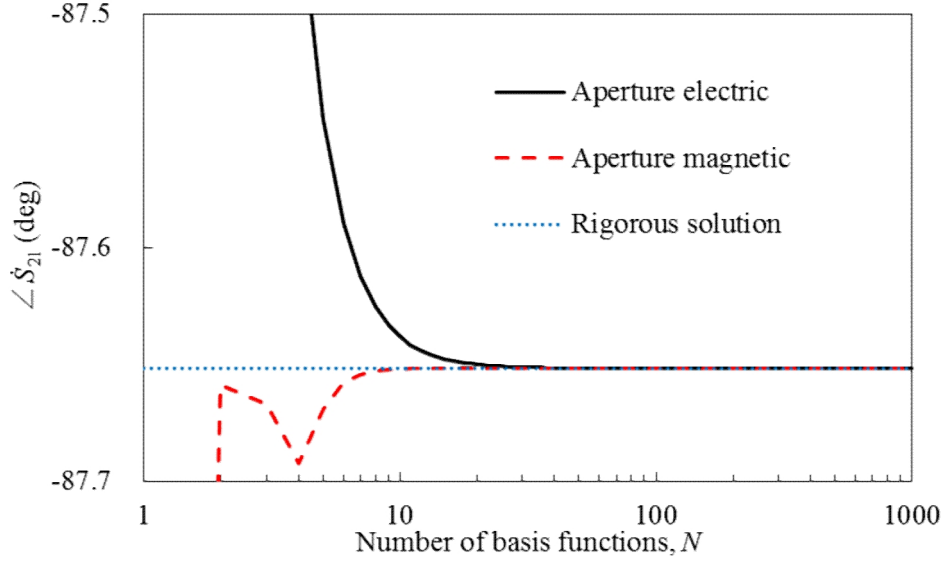
same order of approximation as aperture magnetic fields and order of approximation of the other component H_z is improved by variational nature of Galerkin's procedure.



(a) One-layer sample filling whole cross-section of waveguide.



(b) Convergence of magnitude of complex transmission parameter $|S_{21}|$ with number of basis functions.



(c) Convergence of phase of complex transmission parameter $\angle \dot{S}_{21}$ with number of basis functions.

Fig. 3-2 Convergence of complex transmission parameter \dot{S}_{21} with number of basis functions (sample occupies whole cross-section of waveguide). $a = 22.86\text{mm}$, $\epsilon_r = 8.0 - j2.0$, $\mu_r = 2.0 - j0.7$, $L_s = 10.0\text{mm}$, $f = 10.5\text{GHz}$.

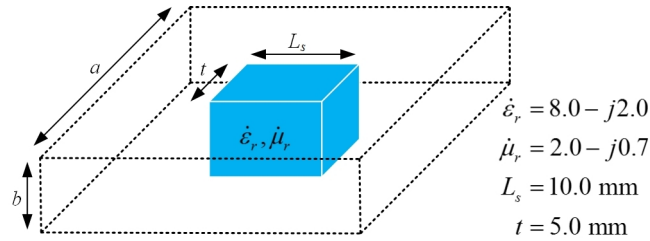
Next, numerical computations are performed for one-layer sample that has the same permittivity and permeability as those in Fig. 3-2 but it occupies only the part of guide cross-section [Fig. 3-3(a)]. The sample is located at the center of waveguide, and $|\dot{S}_{21}|$ and $\angle \dot{S}_{21}$ are evaluated by varying the number of basis functions N until 1007, as shown in Fig. 3-3(b), and (c), respectively. The difference of values by both source quantities decreases uniformly to $2.7 \times 10^{-5} \%$ in $|\dot{S}_{21}|$ and $4.2 \times 10^{-6} \%$ in $\angle \dot{S}_{21}$, respectively for $N = 1007$. It is difficult to get the rigorous solution for this case, and the reference \dot{S}_{21} values are computed by a commercial simulator (Murata Software FEMTET ver. 2014.1.5.51204 64 bit) based on finite element method (FEM) for

comparison. The accuracy of numerical values by FEM using adaptive mesh refinement is checked in Fig. 3-4, where the number of mesh is increased until 307,038, memory capacity bound of workstation [Intel(R) Xeon(R) CPU E5-2660 v2 @ 2.20 GHz 64.00 GB]. Calculated $|\dot{S}_{21}|$ and $\angle \dot{S}_{21}$ with the number of mesh 307,038 are adopted as the reference value and included in Fig. 3-3 (dotted line).

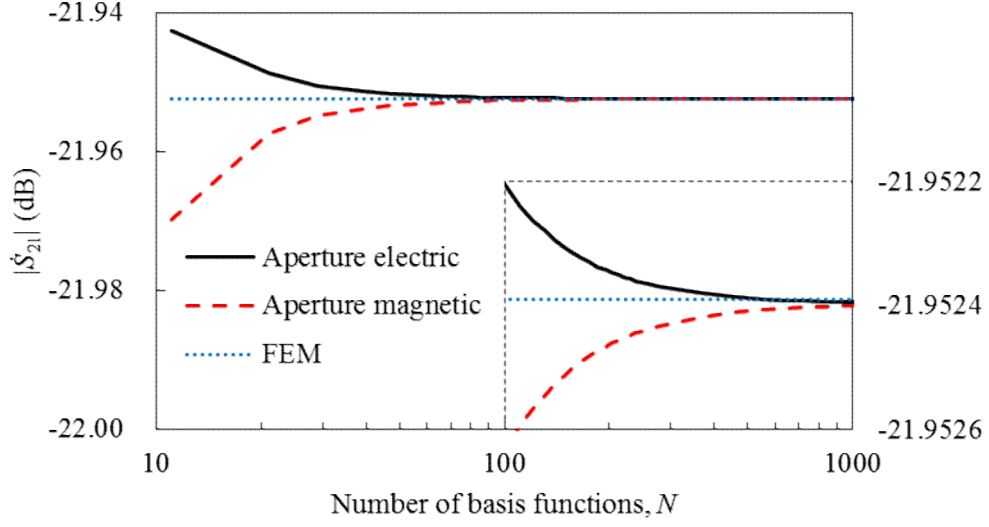
The reference FEM value is located in the range between values by both source quantities until $N = 551$ and deviate slightly upward from the range (enlarged figure in Fig. 3-3). The deviation is very small, that is $|\dot{S}_{21}|$ and $\angle \dot{S}_{21}$ by FEM are $1.82 \times 10^{-5} \%$ (match until sixth digit) and $1.71 \times 10^{-4} \%$ (match until fifth digit) higher than those by aperture electric fields, respectively. This small deviation is due mainly to a shortage of mesh division in FEM calculation as shown in Fig. 3-4. The other reason is the need to introduce the input and output ports in FEM calculation to limit the analytical model to a small area. In FEM calculations of Fig. 3-4, the ports are set to be only 50 mm away from the sample because of limitation in computer memory. Therefore, higher-mode waves generated at sample do not attenuate completely, and come down to the input and output ports, which causes errors in FEM calculation of reflection and transmission parameters.

The computation time of \dot{S}_{21} is 658 seconds by FEM (the number of mesh is 307,038) using the workstation Intel(R) Xeon(R), while it is 0.06 seconds by present method (number of basis functions N is 103) using the small personnel computer Intel(R) Core i7 @ 3.4 GHz, and 58.88 seconds when N is 1007.

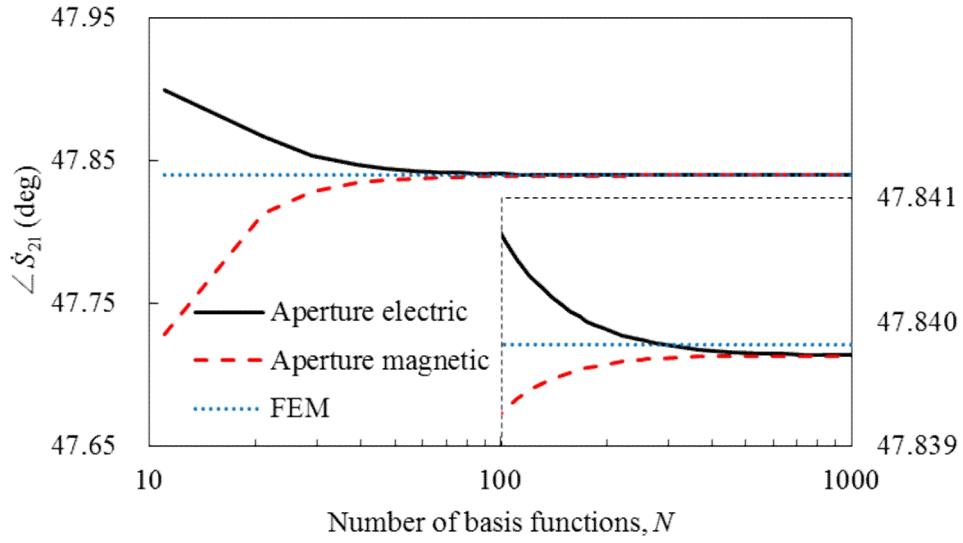
The hybrid EM analytical method is applicable to wide variety of materials. It is required to clarify the difference of convergence according to the material characteristics of loaded sample. Numerical results $|\dot{S}_{21}|$ of non-magnetic dielectric sample ($\dot{\mu}_r = 1$) and virtual magnetic sample $\dot{\epsilon}_r = 1$ at the center of waveguide are shown in Fig. 3-5. When the dielectric sample is loaded, electric fields are concentrated in the sample and the distribution of aperture electric fields is highly distorted so that the convergence of numerical values using aperture electric fields becomes slower [Fig. 3-5(a)] than that using aperture magnetic fields. Similarly, when the virtual magnetic sample is loaded, magnetic fields are concentrated in the sample and the convergence using aperture magnetic fields becomes slower [Fig. 3-5(b)].



(a) One-layer sample loaded at the center.



(b) Convergence of magnitude of complex transmission parameter $|\dot{S}_{21}|$ with number of basis functions.



(c) Convergence of phase of complex transmission parameter $\angle \dot{S}_{21}$ with number of basis functions.

Fig. 3-3 Convergence of complex transmission parameter \dot{S}_{21} with number of basis functions of one-layer sample loaded at the center of waveguide. $\epsilon_r = 8.0 - j2.0$, $\mu_r = 2.0 - j0.7$, $L_s = 10.0$ mm, $t = 5.0$ mm.

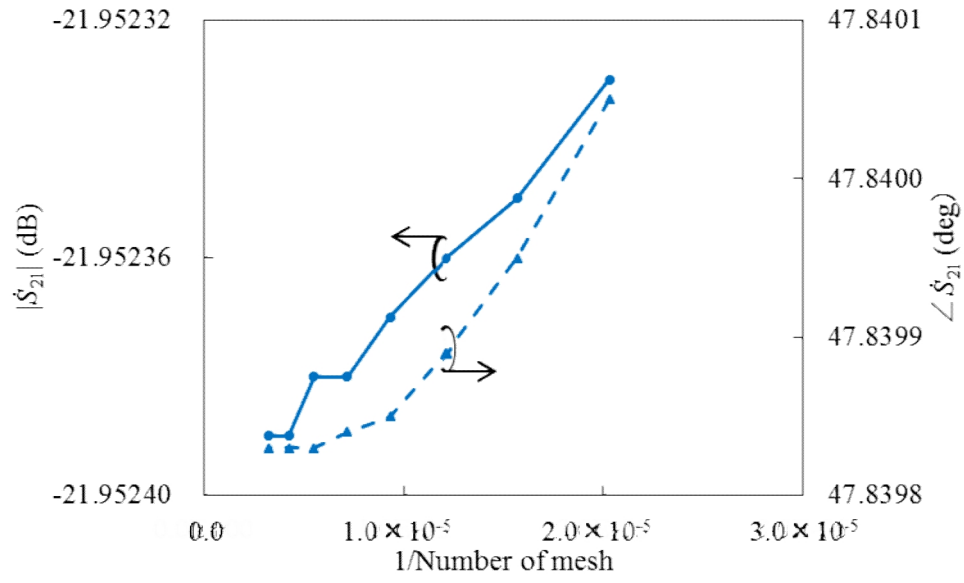
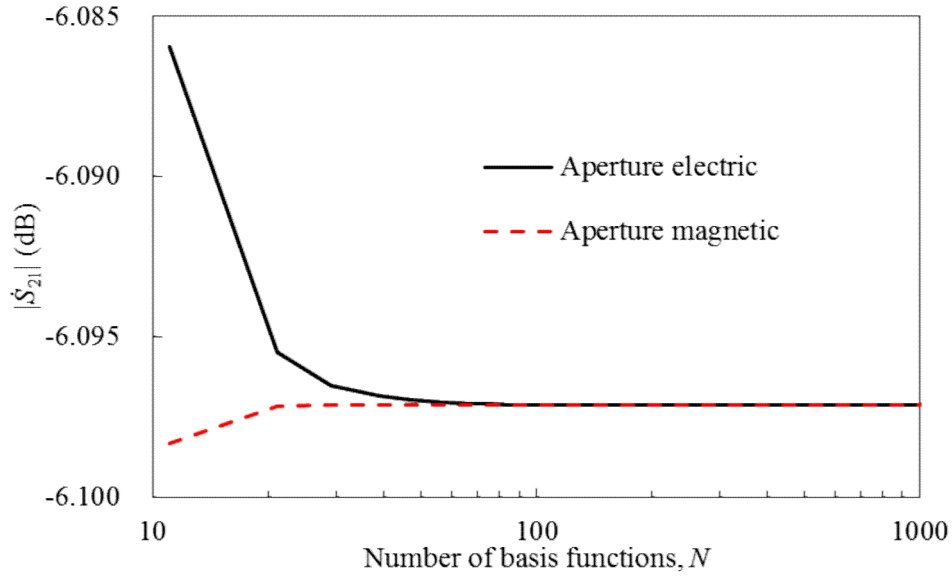
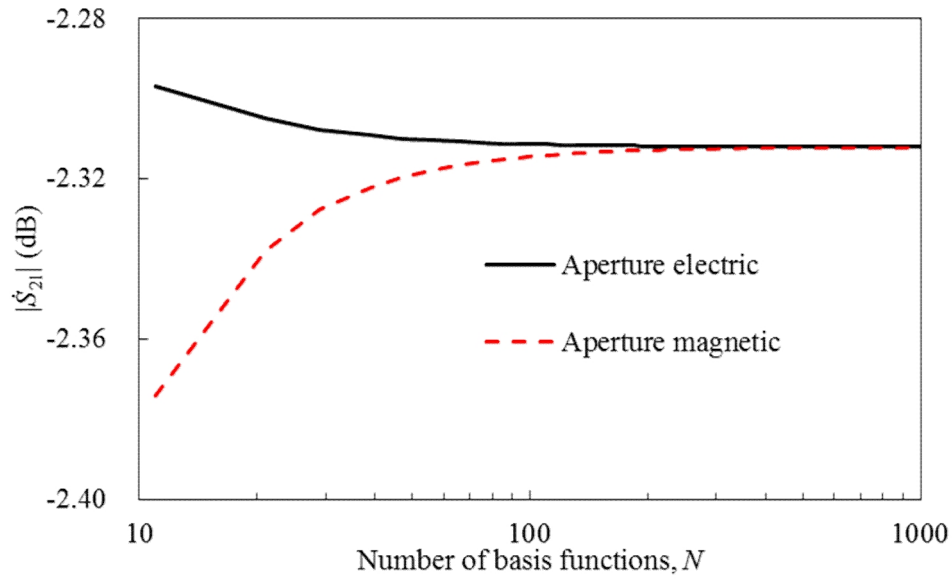


Fig. 3-4 Variation of complex transmission parameter \dot{S}_{21} with number of finite elements in FEM of one-layer sample loaded at the center of waveguide. Dimensions are the same as those in Fig. 3-3.



(a) Dielectric sample ($\dot{\epsilon}_r = 8.0 - j0.8$, $\dot{\mu}_r = 1.0 - j0.0$).

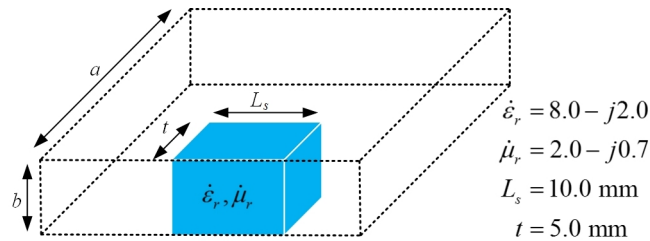


(b) Virtual magnetic sample ($\dot{\epsilon}_r = 1.0 - j0.0$, $\dot{\mu}_r = 8.0 - j0.8$).

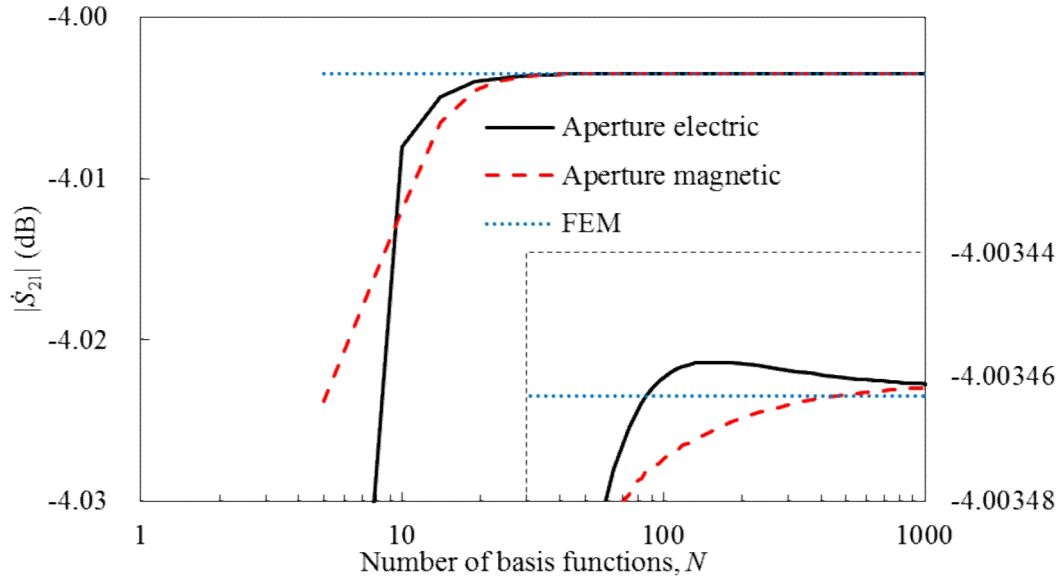
Fig. 3-5 Convergence of transmission parameter $|Ṡ_{21}|$ of one-layer sample with different material parameters loaded at the center of waveguide. $L_s = 10.0$ mm, $t = 5.0$ mm.

Different installation positions of sample are utilized effectively in this measurement method. Convergence characteristics of $|\dot{S}_{21}|$ and $\angle\dot{S}_{21}$ of the sample loaded at the sidewall of waveguide are investigated in Figs. 3-6, where $|\dot{S}_{21}|$ and $\angle\dot{S}_{21}$ are evaluated by increasing the number of basis functions N until 1006. For $N = 1006$, the deviation of $|\dot{S}_{21}|$ and $\angle\dot{S}_{21}$ are less than $7.5 \times 10^{-5} \%$, and an excellent convergence can be observed. The reference values are obtained by FEM with the number of mesh varied until 313,625 ($1 / 313,625 = 0.319 \times 10^{-5}$) as shown in Fig. 3-7. The deviation of values by both source quantities with FEM of $|\dot{S}_{21}|$ and $\angle\dot{S}_{21}$ are less than $7.5 \times 10^{-5} \%$, which is very small as shown in Fig. 3-6.

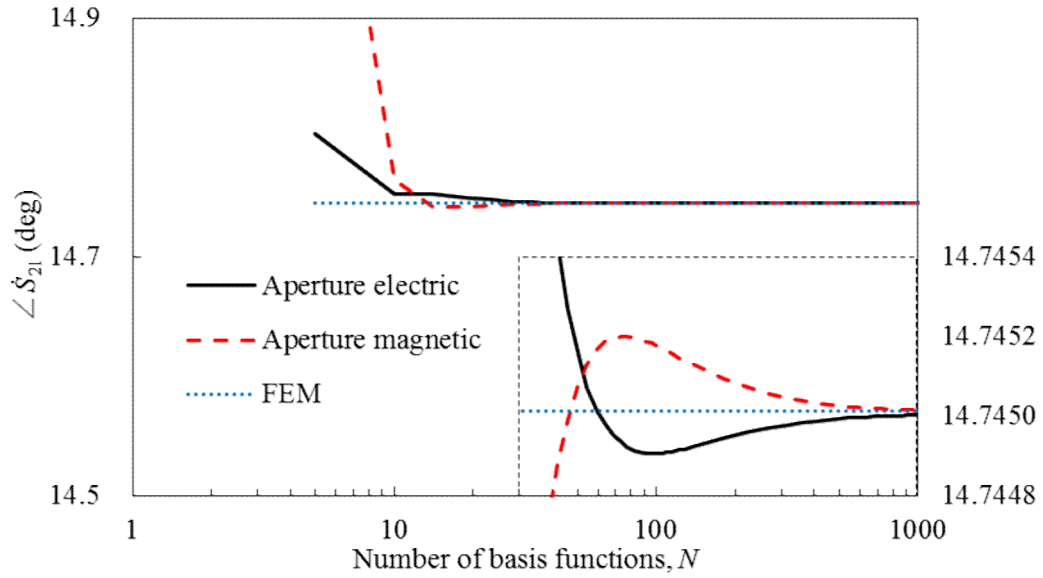
To investigate the material dependency of convergence, non-magnetic dielectric sample ($\dot{\mu}_r = 1$) and virtual magnetic sample $\dot{\epsilon}_r = 1$ are loaded at sidewall. As is the case in the samples loaded at center, the computation using aperture magnetic fields shows faster convergence for dielectric sample [Fig. 3-8(a)], while the computation using aperture electric fields shows faster convergence for magnetic sample [Fig. 3-8(b)].



(a) One-layer sample loaded adjacent to the sidewall.



(b) Convergence of magnitude of complex transmission parameter $|\dot{S}_{21}|$ with number of basis functions.



(c) Convergence of phase of complex transmission parameter $\angle \dot{S}_{21}$ with number of basis functions.

Fig. 3-6 Convergence of complex transmission parameter \dot{S}_{21} with number of basis functions of one-layer sample loaded adjacent to the sidewall of waveguide. Dimensions are the same as those in Fig. 3-3.

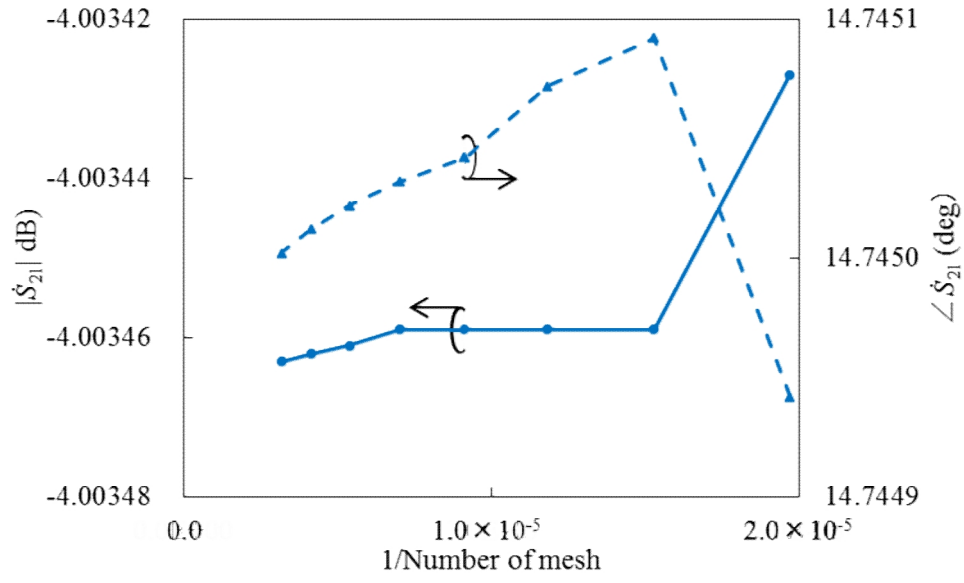
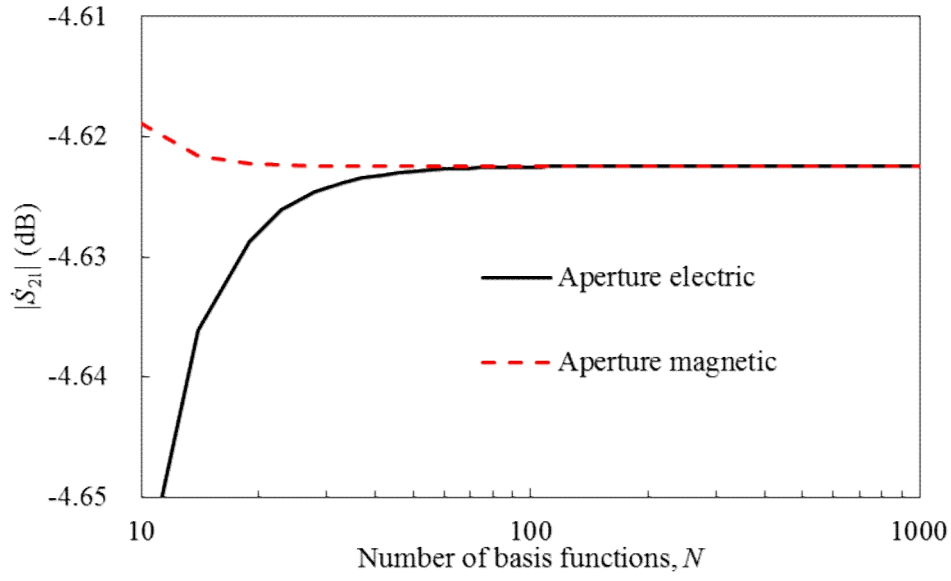
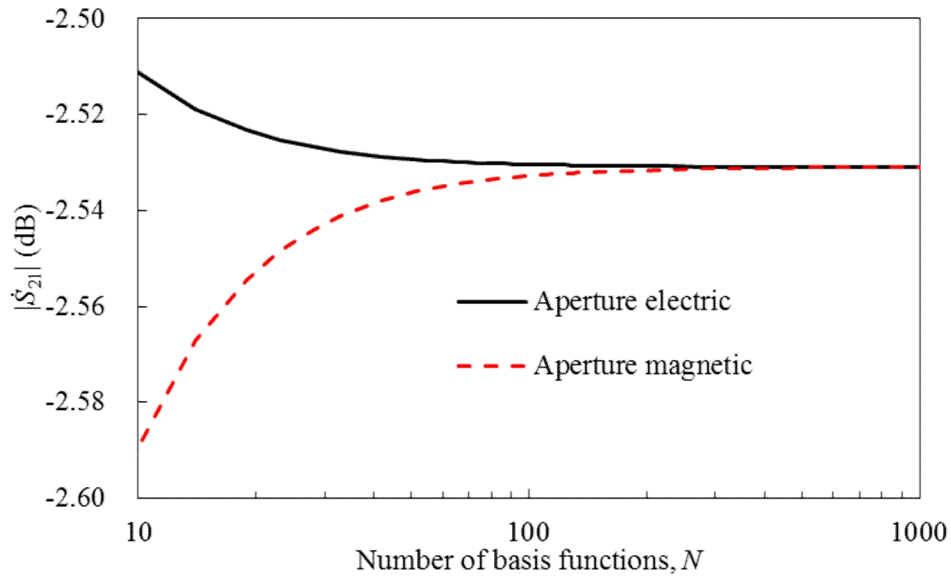


Fig. 3-7 Variation of complex transmission parameter \dot{S}_{21} with number of finite elements in FEM of one-layer sample loaded adjacent to the sidewall of waveguide. Dimensions are the same as those in Fig. 3-3.



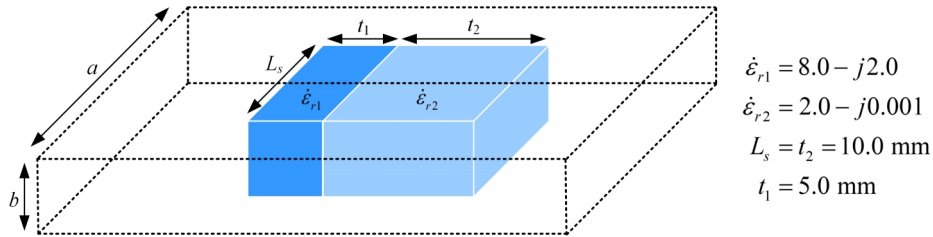
(a) Dielectric sample ($\dot{\epsilon}_r = 8.0 - j 2.0$, $\dot{\mu}_r = 1.0 - j 0.0$).



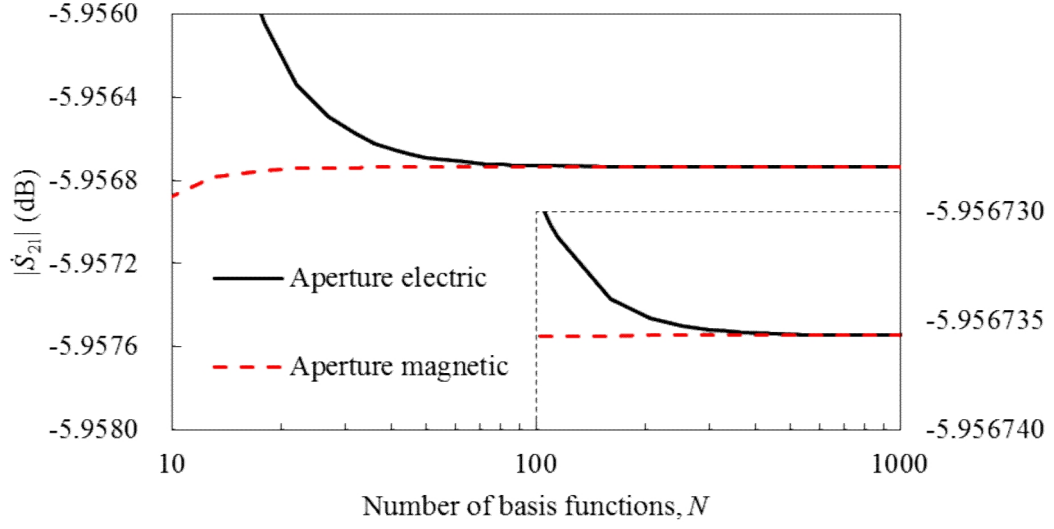
(b) Virtual magnetic sample ($\dot{\epsilon}_r = 1.0 - j 0.0$, $\dot{\mu}_r = 8.0 - j 2.0$).

Fig. 3-8 Convergence of transmission parameter $|S_{21}|$ of one-layer sample with different material parameters loaded adjacent to the sidewall of waveguide. $L_s = 10.0$ mm, $t = 5.0$ mm.

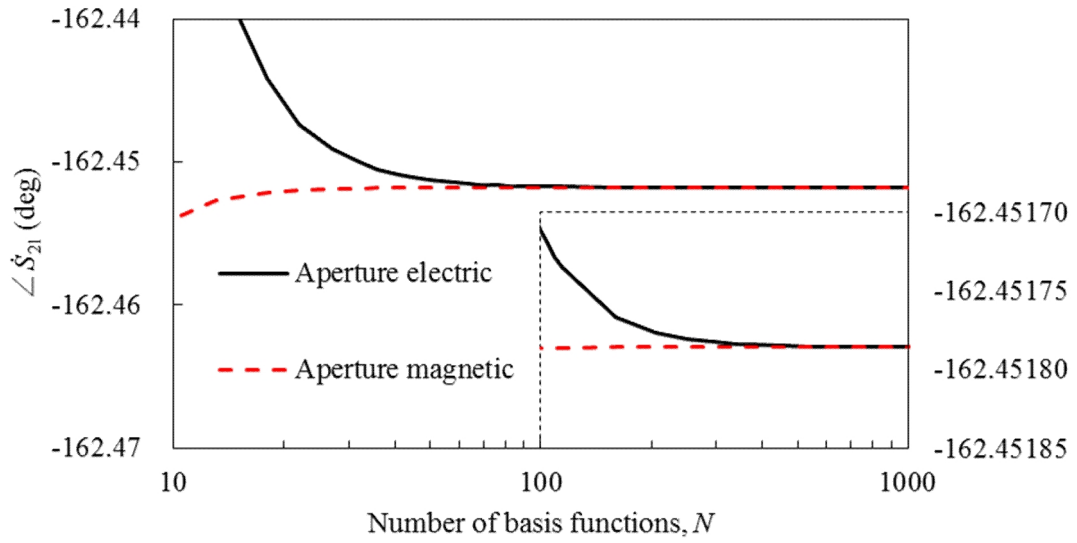
Finally, numerical computations are performed for two-layer sample. The sample consists of a material with higher $\dot{\epsilon}_{r1} = 8.0 - j2.0$ and a material with lower $\dot{\epsilon}_{r2} = 2.0 - j0.001$. As will be explained later in Chapter 4, the transmission parameters of the sample loaded at the center [layout B: Fig. 3-9(a)] and loaded adjacent to the wall [layout X: Fig. 3-10(a)] are measured for determining the permittivities of two-layer sample. For layout B, the convergence characteristics of $|\dot{S}_{21}|$ and $\angle \dot{S}_{21}$ are investigated by increasing the number of basis functions N until 1005. An excellent convergence can be observed as shown in Fig. 3-9, and when N is 1005, the deviation of $|\dot{S}_{21}|$ and $\angle \dot{S}_{21}$ are less than $1.68 \times 10^{-7} \%$. Similarly, for layout X, the convergence characteristics are investigated by increasing the number of basis functions N until 1164. Again an excellent convergence can be observed in Fig. 3-10, and the deviation of $|\dot{S}_{21}|$ and $\angle \dot{S}_{21}$ are less than $1.95 \times 10^{-9} \%$ for $N = 1164$. Similar accuracy and efficiency of numerical computations are observed for a variety of material of varying size, so this hybrid electromagnetic analysis is applicable to various material assessment.



(a) Two-layer sample loaded at the center.

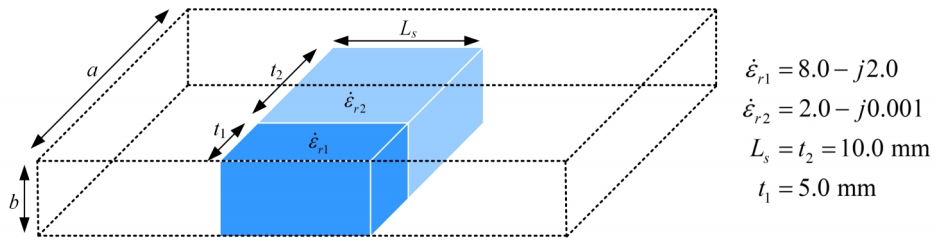


(b) Convergence of magnitude of complex transmission parameter $|\dot{S}_{21}|$ with number of basis functions.

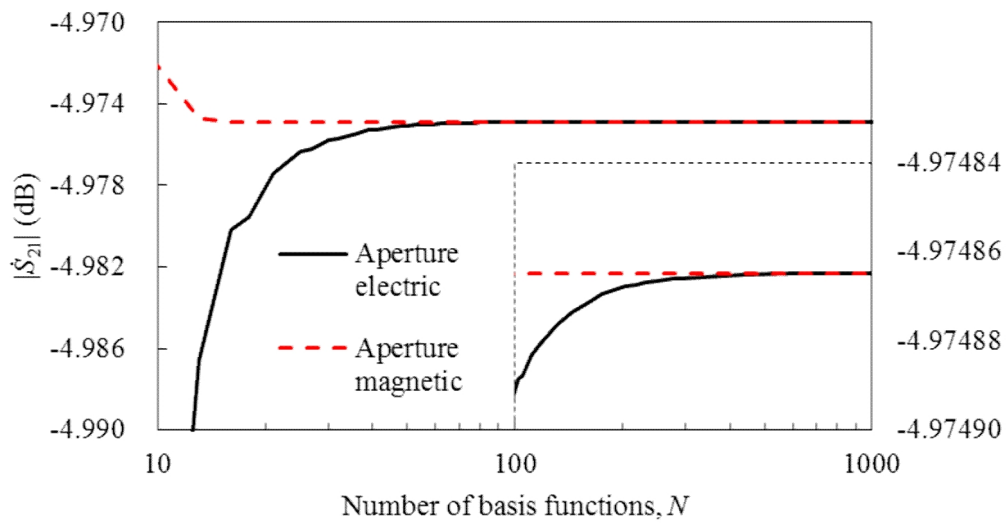


(c) Convergence of phase of complex transmission parameter $\angle \dot{S}_{21}$ with number of basis functions.

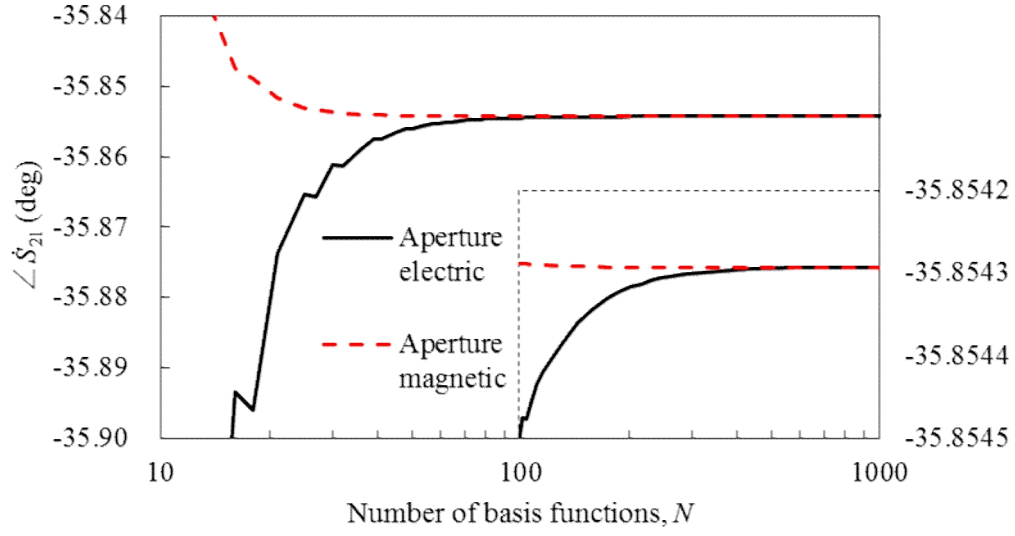
Fig. 3-9 Convergence of complex transmission parameter \dot{S}_{21} with number of basis functions of two-layer sample loaded at the center of waveguide. $\epsilon_{r1} = 8.0 - j2.0$, $\epsilon_{r2} = 2.0 - j0.001$, $L_s = t_1 = 5.0$ mm, $t_2 = 10.0$ mm.



(a) Two-layer sample loaded adjacent to the wall.



(b) Convergence of magnitude of complex transmission parameter $|S_{21}|$ with number of basis functions.



(c) Convergence of phase of complex transmission parameter $\angle \dot{S}_{21}$ with number of basis functions.

Fig. 3-10 Convergence of complex transmission parameter \dot{S}_{21} with number of basis functions of one-layer sample loaded adjacent to the sidewall of waveguide. $\epsilon_{r1} = 8.0 - j2.0$, $\epsilon_{r2} = 2.0 - j0.001$, $L_s = t_1 = 5.0$ mm, $t_2 = 10.0$ mm.

Chapter 4 Material Assessment Based on Numerical Analysis

- 4.1 Preliminary investigation into possibility of material assessment
 - 4.2 Material estimation algorithm and virtual experiment
 - 4.3 Robustness analysis of material estimation
 - 4.4 Error analysis of material estimation
-

Chapter 4 Material Assessment Based on Numerical Analysis

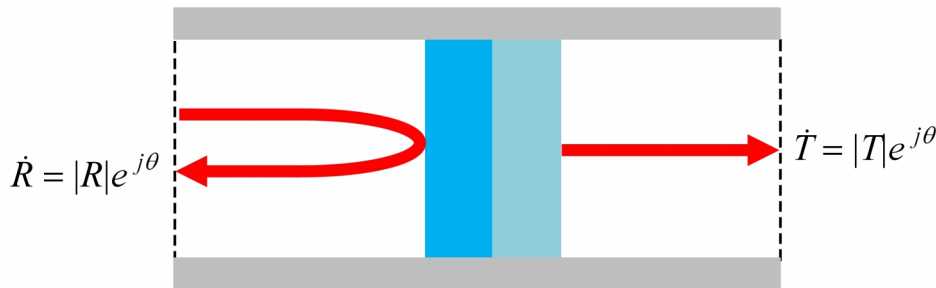
Based on the hybrid electromagnetic analysis method explained in previous chapters, a material evaluation procedure is developed in this chapter to determine the complex permittivities of each layer of two-layer dielectric sample. The frequency-dependent complex permittivity of single-layer material has been determined mainly by the transmission-line method using waveguide or coaxial cable [7]-[16], where only the complex reflection parameter or transmission parameter is measured to determine the complex permittivity. Magnitude and phase of the complex reflection parameter or transmission parameter, which means that two real values, are measured to determine two unknowns, real and imaginary parts of complex permittivity. While to determine two unknown complex permittivities of two-layer sample (four real unknown values), it requires to measure two complex numerical values (four real measured values). They may be measurement values of both complex reflection and transmission

parameters [Fig. 4-1(a)] [33], or those of the complex transmission parameters of two set samples with different dimension [Fig. 4-1(b)]. However, accurate measurement of complex reflection parameter is more difficult than that of complex transmission parameter. The calibration reference to measure complex reflection parameter is difficult to define and error in reference plane Δz causes error in phase of reflection parameter $\Delta\phi$ (Fig. 4-2). Therefore the phase measurement of complex reflection parameter is susceptible to position error (Fig. 4-2). Meanwhile when two different samples are used to determine the material characteristics [Fig. 4-1(b)], an error is caused by the sample inhomogeneity and also machining error in sample preparation is superimposed.

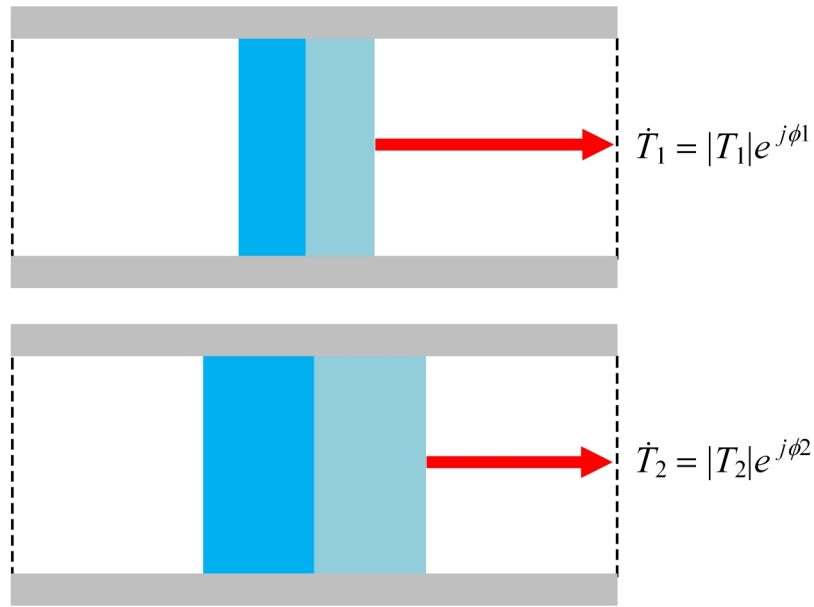
A measurement method is expected to determine the complex permittivities of two-layer sample using only one set of sample without measurement of reflection parameter. New material evaluation procedure is developed in the following where the complex transmission parameters are measured for two different locations and/or orientations of single sample.

First, transmission characteristics are numerically investigated for different locations and/or orientations of two-layer sample in section 4.1 to determine the best combination of sample locations and/or orientations. The present method is intended to realize broadband measurement of complex permittivities. For this purpose, sample locations which have no drastic changes in complex transmission parameters over the measured frequency range should be selected. Second, an iterative route searching algorithm is developed in section 4.2 to determine the complex permittivities of each layer of two-layer sample. This material assessment uses the measured complex

transmission parameters of two different locations of sample as shown in Fig. 4-3. The optimized complex permittivities of each layer are determined so as to minimize the differences of the measured and calculated transmission parameters for both locations. The algorithm uses a bootstrap technique, that is, at first one location is used to optimize the permittivity of one layer [Fig. 4-3(a): first process], and then the other location is used to optimize the permittivity of the other layer [Fig. 4-3(b): second process]. These separate processes are repeated alternately until the differences of the measured and calculated transmission parameters fall below the tolerance. Virtual experiments as well as real experiments are performed to verify the accuracy, versatility, efficiency and robustness of the material estimation procedure. In virtual experiments, the measured complex transmission parameters are generated by using a commercial FEM simulator for the same structure as real experiment. The iterative route searching algorithm of permittivities starts with an initial value and the choice of the initial value is important in this material estimation process. Next, the iterative algorithm is examined numerically by performing virtual experiments in section 4.3 and robustness of the method is examined. Section 4.4 will investigate the sensitivity of permittivities to deviations in sample location, length and thickness.



(a) Measurement method using both complex reflection and transmission parameters.



(b) Measurement method using two set samples with different dimension.

Fig. 4-1 Measurement method of two-layer sample.

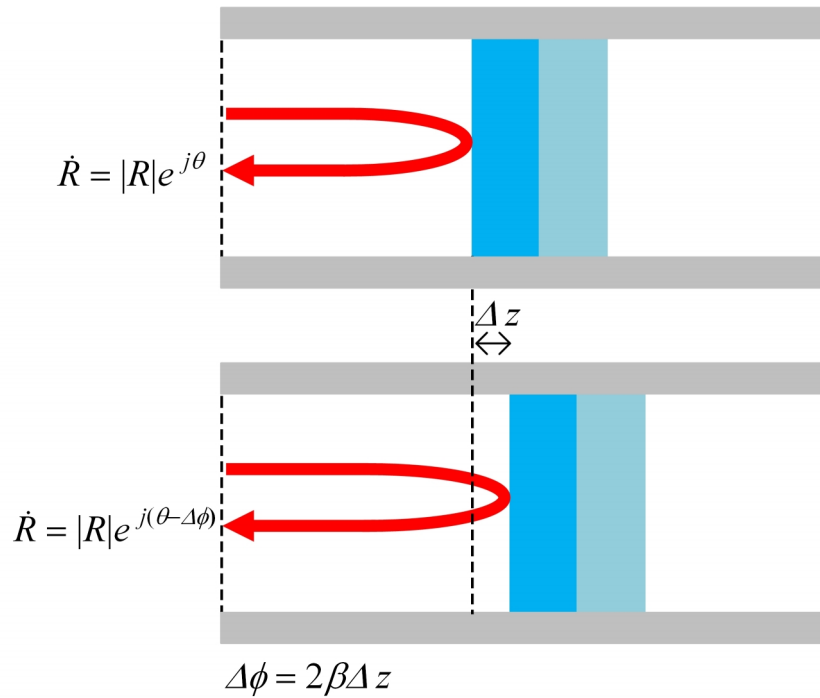
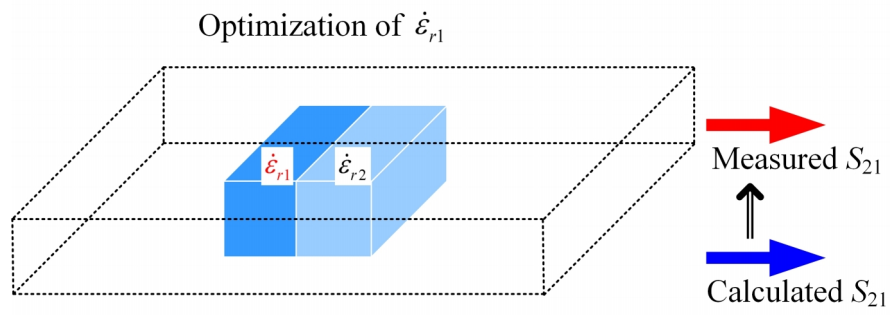
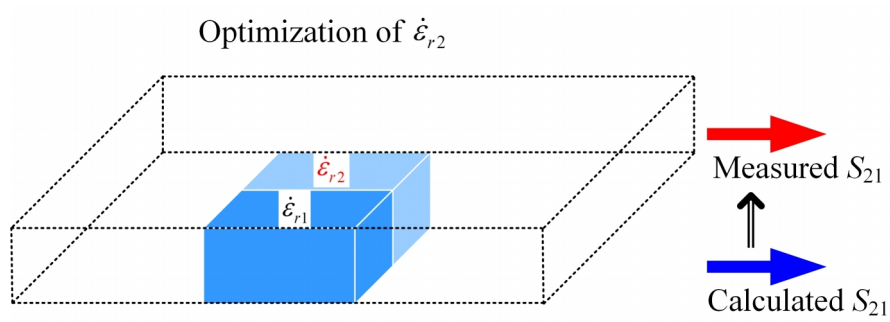


Fig. 4-2 Fluctuation of calibration reference in reflection measurement.



(a) First process of the iterative algorithm.



(b) Second process of the iterative algorithm.

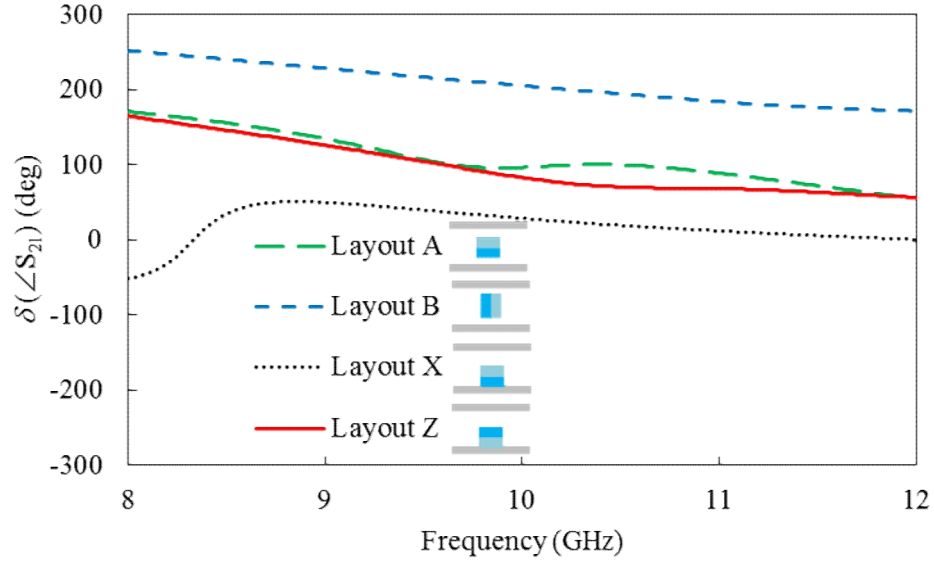
Fig. 4-3 Iterative algorithm to determine complex permittivities of two-layer sample.

4.1 Preliminary investigation into possibility of material assessment

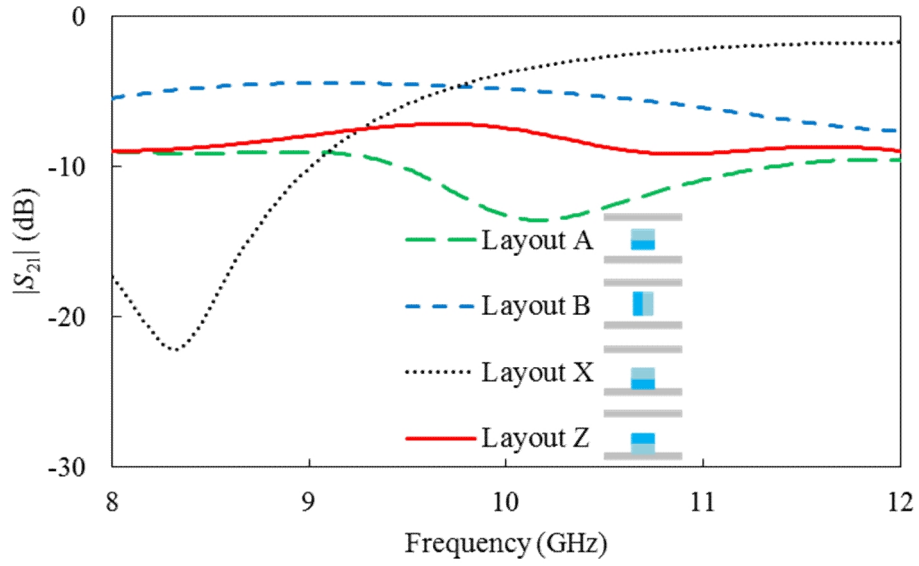
Preliminary computations are carried out to investigate feasibility of this evaluation method and determine the optimum combination of sample positioning. A two-layer sample with complex permittivities $\hat{\epsilon}_{r1}$, $\hat{\epsilon}_{r2}$ and widths W_1 , W_2 is placed at four different layouts in the waveguide as shown in Fig. 4-4, where the dark blue layer represents higher permittivity layer and the light blue layer represents lower permittivity layer. In layouts A and B, sample is loaded at center of waveguide but their sample orientations are different. In layouts X and Z sample is set along the sidewall of waveguide, and layer with higher permittivity faces the sidewall in layout X, while layer with lower permittivity faces the sidewall in layout Z. Frequency-dependent transmission characteristics are calculated for these layouts by the hybrid EM method. The phase delay of the transmission parameters of loaded waveguides with respect to the unloaded cases $\delta(\angle S_{21}) = \angle S_{21}^L - \angle S_{21}^U$ is shown in Fig. 4-4(a) and the amplitude of the transmission parameters $|S_{21}|$ is shown in Fig. 4-4(b). There exist resonances in layout A and X, where transmission parameters change significantly and material assessment may be less accurate. Layout B and Z do not have significant resonance compared with layout A and X. Layout B and Z are chosen for material assessment of this sample. In many practical situations, combination of other layouts may be preferable to avoid resonance. The resonant frequency changes with the permittivity and length of sample and the resonance can be removed from the measured frequency range by adjusting the length of sample L_s . The sample length L_s can be chosen arbitrarily in the present method as there is no need to fill up the whole cross-section of the waveguide unlike in the case of conventional measurement method. Also the resonance

in layouts A and X can be moved by displacing the installation position of sample slightly.

The transmission parameters of layout B and Z are compared with those by a commercial FEM simulator (Murata Software FEMTET) and are in excellent agreement over the operating frequency range of *X*-band waveguide (Fig. 4-5). It is observed that the phase delay of layout B is much larger than that of layout Z. The fact that the phase delay shifts greatly for the different installation locations and/or orientations of the two-layer sample in the waveguide works better in determination of the real part of complex permittivity, while a significant change in the magnitude works better in determination of the imaginary part of complex permittivity.

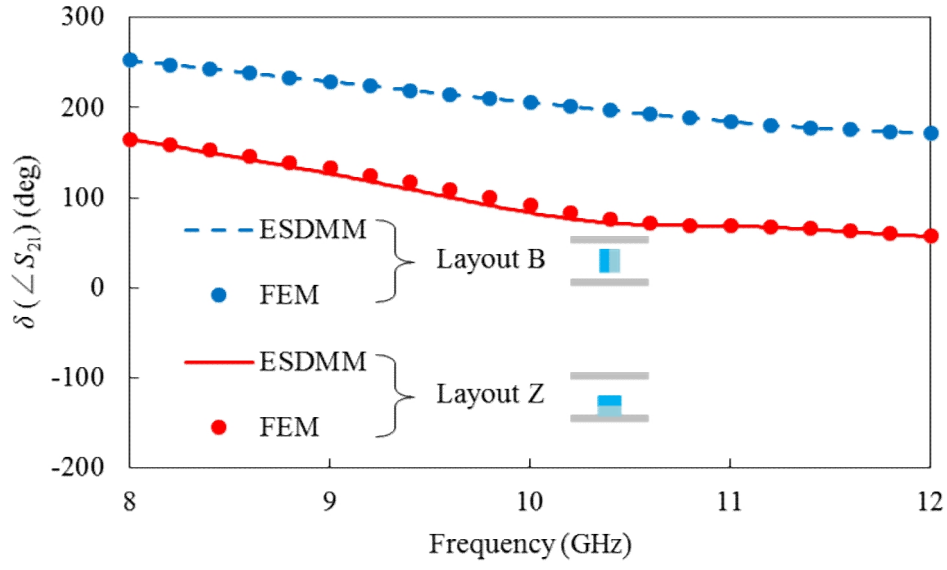


(a) Phase delay of S_{21} .

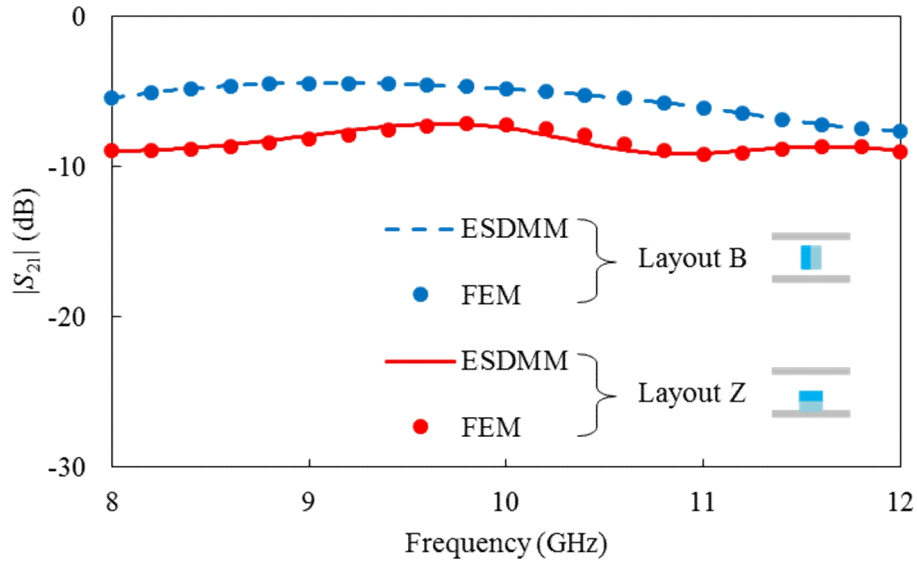


(b) Amplitude of S_{21} .

Fig. 4-4 Transmission characteristics with different layouts of sample. $\epsilon_{r1} = 10.0 - j2.0$, $\epsilon_{r2} = 2.0 - j0.001$, $L_s = 10.0$ mm, $t_1 = t_2 = 5.0$ mm.



(a) Phase delay of S_{21} .



(b) Amplitude of S_{21} .

Fig. 4-5 Complex transmission parameters of layout B and Z for material assessment.

4.2 Material estimation algorithm and virtual experiment

An efficient and stable iterative algorithm is used to determine the complex permittivities of two-layer sample from the measured complex transmission parameters for two different locations and/or orientations of single sample. The iterative route searching algorithm is shown in flow diagram of Fig. 4-6, where the difference in complex transmission parameters of different installation is used advantageously.

An error tolerance specification is set and initial guess is chosen for permittivities of each layer. Regarding the selection of the initial values, various cases may be possible in real measurements. For instance, in one measurement case, the initial value of one of two layers can be predicted or guessed and in the other measurement cases, initial values of both layers are completely unpredictable. The initial value dependence of the evaluation process will be investigated in next section.

The estimated values which meet the error tolerance specifications can be found by alternately performing the following two processes. In the first process, ϵ_{r2} is fixed at its initial value and S_{21} is calculated by the hybrid electromagnetic method for layout B varying only ϵ_{r1} around its initial value to obtain the minimum difference between the calculated and measured S_{21} . Next, ϵ_{r1} is fixed at its optimal value, and only ϵ_{r2} is varied to get the minimum difference between the calculated and measured S_{21} values for layout Z. These separate processes are repeated alternately until the minimum differences of the calculated and measured S_{21} are less than the set tolerance value both for layout B and Z.

A virtual experiment is performed to investigate the practical use of the above estimation process. The virtual experiment is constructed as follows. First, the virtual

measured S_{21} are generated by setting the permittivities of the sample to $\dot{\epsilon}_{r1}^p$ and $\dot{\epsilon}_{r2}^p$ (preassigned), and evaluate complex transmission parameters of two different sample layouts by the commercial FEM simulator using the preassigned $\dot{\epsilon}_{r1}^p$ and $\dot{\epsilon}_{r2}^p$. Hereafter, these complex transmission parameters are regarded as the virtually measured S_{21} . The permittivities $\dot{\epsilon}_{r1}$ and $\dot{\epsilon}_{r2}$ are treated as unknowns and they are estimated by using the above process.

Table 4-1 shows the preassigned $\dot{\epsilon}_{r1}^p$ and $\dot{\epsilon}_{r2}^p$ of four samples of two-layer materials and their estimated $\dot{\epsilon}_{r1}$ and $\dot{\epsilon}_{r2}$ which are obtained after five iterations. Each iterative step consists of the fitting of $\dot{\epsilon}_{r1}$ for layout B and the fitting of $\dot{\epsilon}_{r2}$ for layout Z. The dimensions of the sample 1, 2, 3 and 4 are same, which are $t_1 = 5.00$ mm, $t_2 = 5.00$ mm and $L_s = 10.00$ mm, except for the sample 3 where $t_2 = 10.00$ mm. An accurate reproduction is observed in the table.

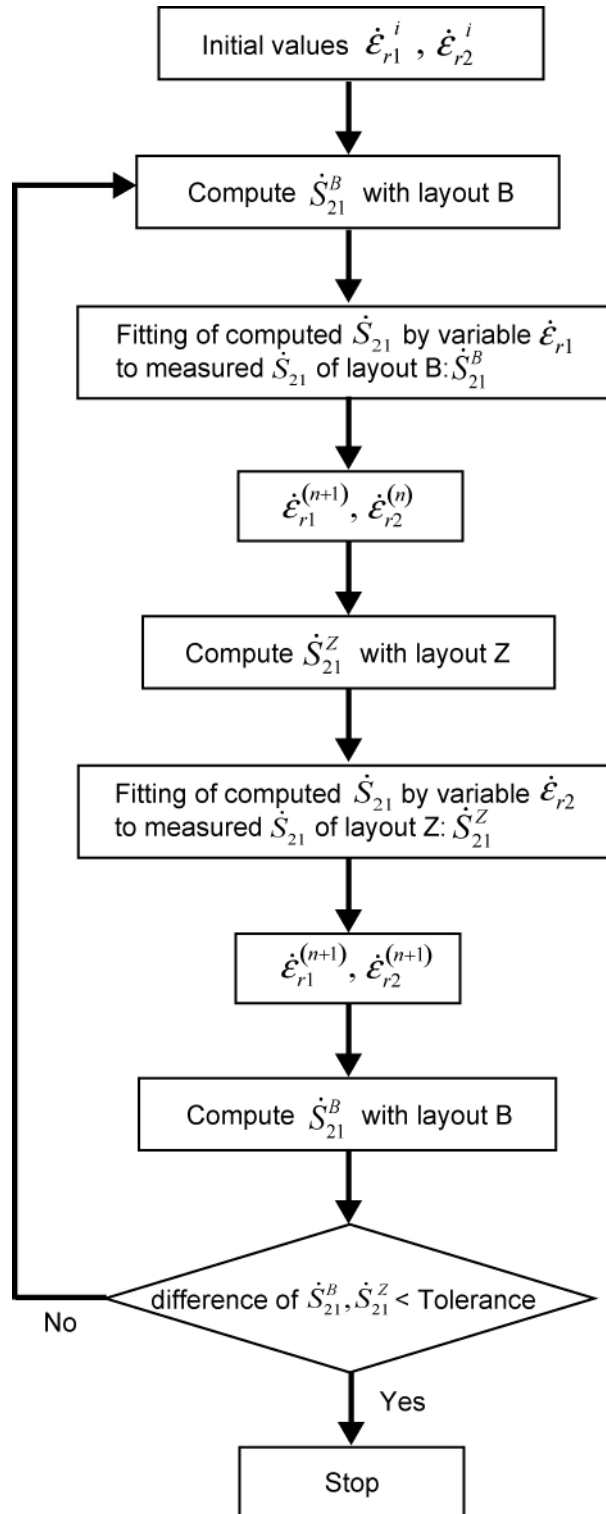


Fig. 4-6 Iterative procedure for determination of permittivities of two-layer sample $\dot{\epsilon}_{r1}$ and $\dot{\epsilon}_{r2}$.

Table 4-1 Virtual experiments using different two-layer samples.

		Preassigned	Estimated
Sample 1	Layer 1	$5.0 - j2.5 \times 10^{-3}$	$5.0 - j2.5 \times 10^{-3}$
	Layer 2	$2.0 - j1.0 \times 10^{-3}$	$2.0 - j1.0 \times 10^{-3}$
Sample 2	Layer 1	$10.0 - j2.0$	$10.0 - j2.0$
	Layer 2	$5.0 - j2.5 \times 10^{-3}$	$5.0 - j2.7 \times 10^{-3}$
Sample 3	Layer 1	$10.0 - j2.0$	$10.0 - j2.0$
	Layer 2	$2.0 - j1.0 \times 10^{-3}$	$2.0 - j1.0 \times 10^{-3}$
Sample 4	Layer 1	$10.0 - j2.0$	$10.0 - j2.0$
	Layer 2	$5.0 - j2.5 \times 10^{-1}$	$5.0 - j2.5 \times 10^{-1}$

4.3 Robustness analysis of material estimation

In the above evaluation process, the choice of the initial values (starting permittivity values) is important. A poor selection of the initial values would lead to slower convergence and may also give an erroneous value. It is important to investigate the initial value dependence of the evaluation process. Sample 3 in Table 4-1 is used for the investigation and material estimation is performed with a great change in initial values $\dot{\epsilon}_{r1}^i$ and $\dot{\epsilon}_{r2}^i$ in Fig. 4-7. The absolute value of initial complex permittivities $|\epsilon_{r1}^i/\epsilon_{r1}^p|$, $|\epsilon_{r2}^i/\epsilon_{r2}^p|$ are varied while loss tangents $\tan \delta_1 = \epsilon_{r1}''/\epsilon_{r1}'$, $\tan \delta_2 = \epsilon_{r2}''/\epsilon_{r2}'$ are kept constant in Fig. 4-7(a), where ϵ_{r1}'' , ϵ_{r2}'' are the imaginary part of complex permittivities, and the mark ‘○’ represents the reproduction of permittivities is available and ‘×’ represents the reproduction is unavailable. Accurate reproduction is observed in wide range, $0.5 \leq |\epsilon_{r1}^i/\epsilon_{r1}^p| \leq 1.5$ and $0.4 \leq |\epsilon_{r2}^i/\epsilon_{r2}^p| \leq 2.1$. Then, the loss tangent $\tan \delta_1 = \epsilon_{r1}''/\epsilon_{r1}'$, $\tan \delta_2 = \epsilon_{r2}''/\epsilon_{r2}'$ are varied while absolute values $|\epsilon_{r1}^i/\epsilon_{r1}^p|$, $|\epsilon_{r2}^i/\epsilon_{r2}^p|$ are kept constant in Fig. 4-7(b). When the initial value of loss tangents are in range $0.0 \leq \tan \delta_1 \leq 1.0$ and $0.0 \leq \tan \delta_2 \leq 0.0190$, the convergence to the preassigned values can be obtained. The robustness of initial value is confirmed, and a similarly good convergence is observed for sample 1, 2 and 4 in Table 4-1.

Fig. 4-8 shows the convergent processes of $\dot{\epsilon}_{r1}$ and $\dot{\epsilon}_{r2}$ values which start with the initial values and approach the preassigned value through iterative steps. The initial values of both complex permittivities are set to have great difference with preassigned values in Fig. 4-7(a), that is, the initial $\dot{\epsilon}_{r1}^i$ is set to be 50% higher ($1.5\dot{\epsilon}_{r1}^p$) or 50% lower ($0.5\dot{\epsilon}_{r1}^p$) than the preassigned value and $\dot{\epsilon}_{r2}^i$ is set to be 110% higher ($2.1\dot{\epsilon}_{r2}^p$) or 60% lower ($0.4\dot{\epsilon}_{r2}^p$) [red mark in Fig. 4-7(a)]. The preassigned values are

reconstructed within a tolerance of 1% after 15 steps for all cases. Rapid convergence even with these poor initial values shows the efficiency of the present method. The fitting process starts from layout B in material assessment above, but same convergence can be observed when the fitting process starts from layout Z.

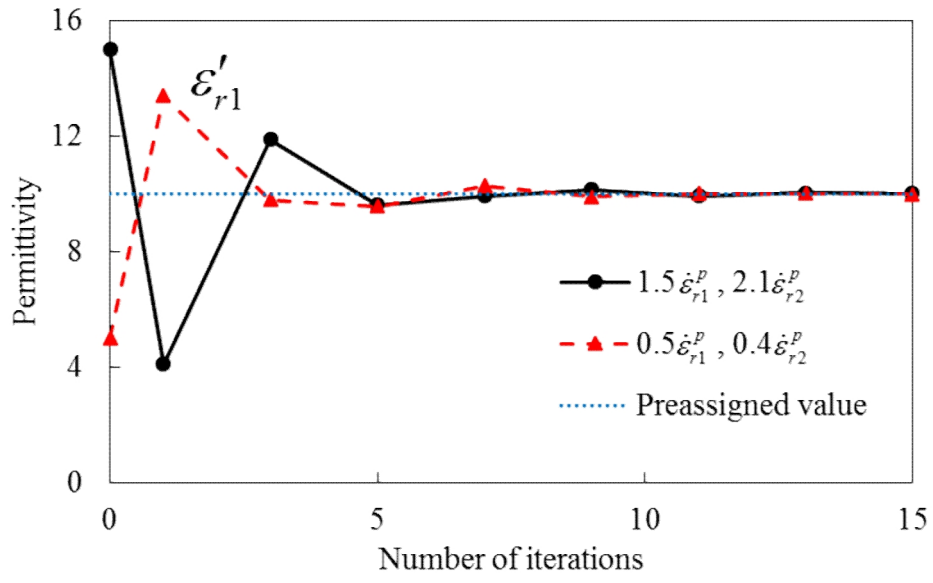
		$\epsilon_{r1}'^i / \epsilon_{r1}'^p$																
		0.1	0.2	0.3	0.4	0.5	0.6	0.7	0.8	0.9	1.0	1.1	1.2	1.3	1.4	1.5	1.6	1.7
$\epsilon_{r2}'^i / \epsilon_{r2}'^p$	0.1	×	×	×	×	×	×	×	×	×	×	×	×	×	×	×	×	×
	0.2	×	×	×	×	×	×	×	×	×	○	○	×	×	×	○	×	×
	0.3	×	×	×	○	×	×	○	×	○	○	○	○	○	○	○	○	○
	0.4	×	×	×	×	○	○	○	○	○	○	○	○	○	○	○	○	○
	0.5	×	×	×	×	○	○	○	○	○	○	○	○	○	○	○	○	○
	0.6	×	○	×	○	○	○	○	○	○	○	○	○	○	○	○	○	○
	0.7	○	○	×	○	○	○	○	○	○	○	○	○	○	○	○	○	○
	0.8	○	○	○	○	○	○	○	○	○	○	○	○	○	○	○	○	○
	0.9	○	○	×	×	○	○	○	○	○	○	○	○	○	○	○	○	○
	1.0	○	○	×	×	○	○	○	○	○	○	○	○	○	○	○	○	○
	1.1	○	○	○	○	○	○	○	○	○	○	○	○	○	○	○	○	○
	1.2	○	○	×	×	○	○	○	○	○	○	○	○	○	○	○	○	○
	1.3	○	○	○	×	○	○	○	○	○	○	○	○	○	○	○	○	○
	1.4	○	○	○	○	○	○	○	○	○	○	○	○	○	○	○	○	○
	1.5	○	○	○	○	○	○	○	○	○	○	○	○	○	○	○	○	○
	1.6	○	○	○	○	○	○	○	○	○	○	○	○	○	○	○	○	×
	1.7	○	×	○	○	○	○	○	○	○	○	○	○	○	○	○	○	×
	1.8	○	○	○	○	○	○	○	○	○	○	○	○	○	○	○	×	×
	1.9	○	○	○	○	○	×	○	○	○	○	○	○	○	○	○	×	×
	2.0	○	○	×	○	○	○	○	○	○	○	○	○	○	○	○	×	×
	2.1	○	○	○	○	○	○	○	○	○	○	○	○	○	○	○	×	×
	2.2	×	×	○	○	○	×	×	×	×	×	×	×	×	○	○	×	×

(a) Change in absolute value of initial complex permittivities with fixed $\tan \delta_1$ and $\tan \delta_2$.

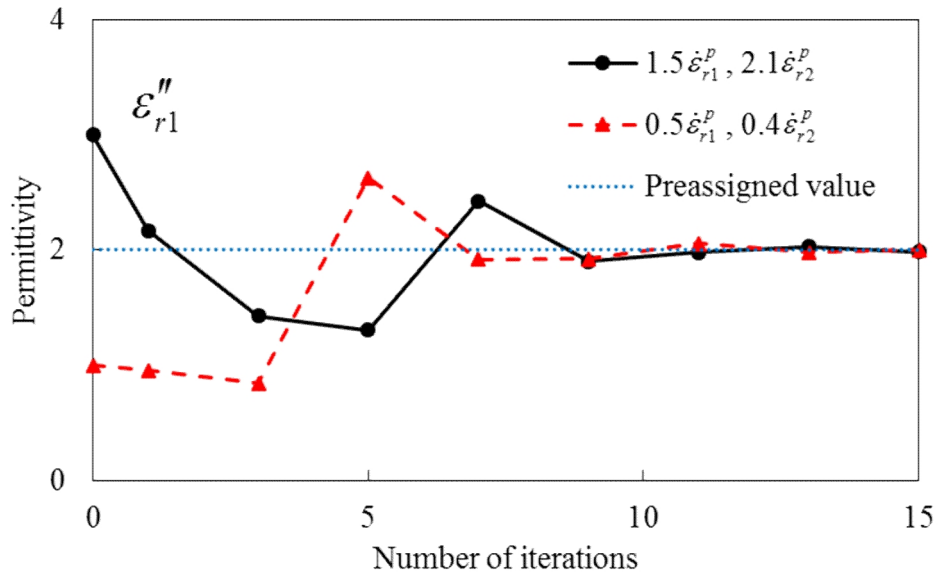
		$\tan \delta_1$											
		0.0	0.1	0.2	0.3	0.4	0.5	0.6	0.7	0.8	0.9	1.0	1.1
$\tan \delta_2$	0.0000	○	○	○	○	○	○	○	○	○	○	○	×
	0.0005	○	○	○	○	○	○	○	○	○	○	○	×
	0.0010	○	○	○	○	○	○	○	○	○	○	○	○
	0.0015	○	○	○	○	○	○	○	○	○	○	○	×
	0.0020	○	○	○	○	○	○	○	○	○	○	○	×
	0.0025	○	○	○	○	○	○	○	○	○	○	○	○
	0.0030	○	○	○	○	○	○	○	○	○	○	○	×
	0.0035	○	○	○	○	○	○	○	○	○	○	○	○
	0.0040	○	○	○	○	○	○	○	○	○	○	○	×
	0.0045	○	○	○	○	○	○	○	○	○	○	○	○
	0.0050	○	○	○	○	○	○	○	○	○	○	○	×
	⋮												
	0.0170	○	○	○	○	○	○	○	○	○	○	○	×
	0.0175	○	○	○	○	○	○	○	○	○	○	○	○
	0.0180	○	○	○	○	○	○	○	○	○	○	○	×
	0.0185	○	○	○	○	○	○	○	○	○	○	○	×
	0.0190	○	○	○	○	○	○	○	○	○	○	○	×
	0.0195	○	○	○	○	○	○	○	○	○	○	×	○

(b) Change in loss tangents of initial complex permittivities with fixed $\left| \varepsilon_{r1}^{\prime i} / \varepsilon_{r1}^{\prime p} \right|$ and $\left| \varepsilon_{r2}^{\prime i} / \varepsilon_{r2}^{\prime p} \right|$.

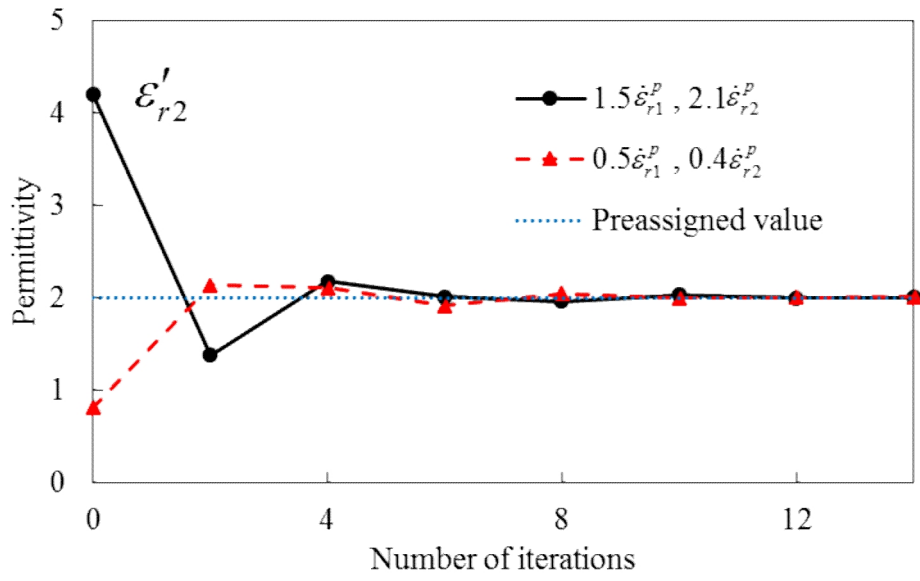
Fig. 4-7 Initial value dependence in material assessment.



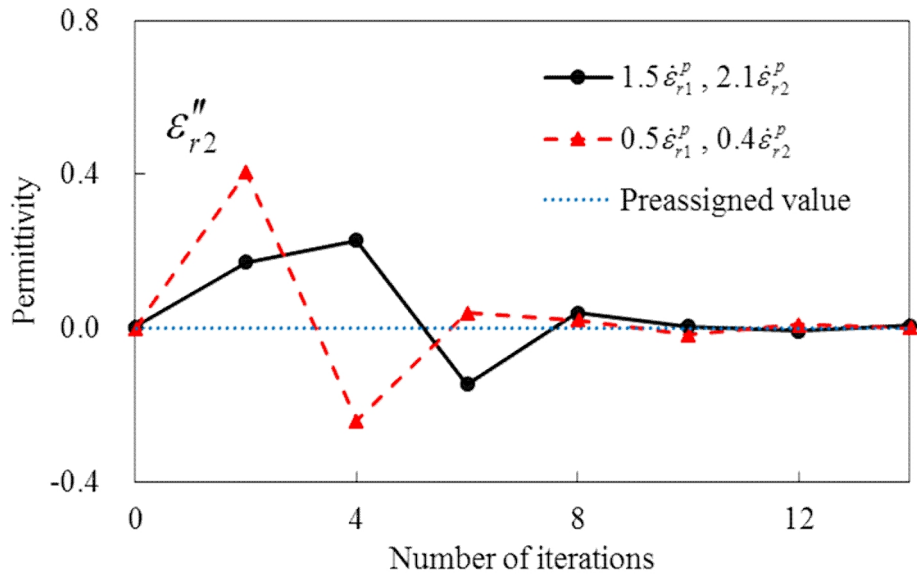
(a) Real part of $\dot{\epsilon}_{r1}$.



(b) Imaginary part of $\dot{\epsilon}_{r1}$.



(c) Real part of ϵ'_{r2} .



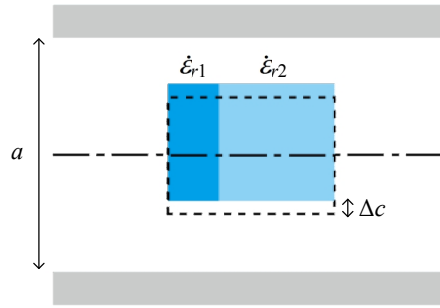
(d) Imaginary part of ϵ''_{r2} .

Fig. 4-8 Convergent process of ϵ_{r1} and ϵ_{r2} values during the fitting calculation.

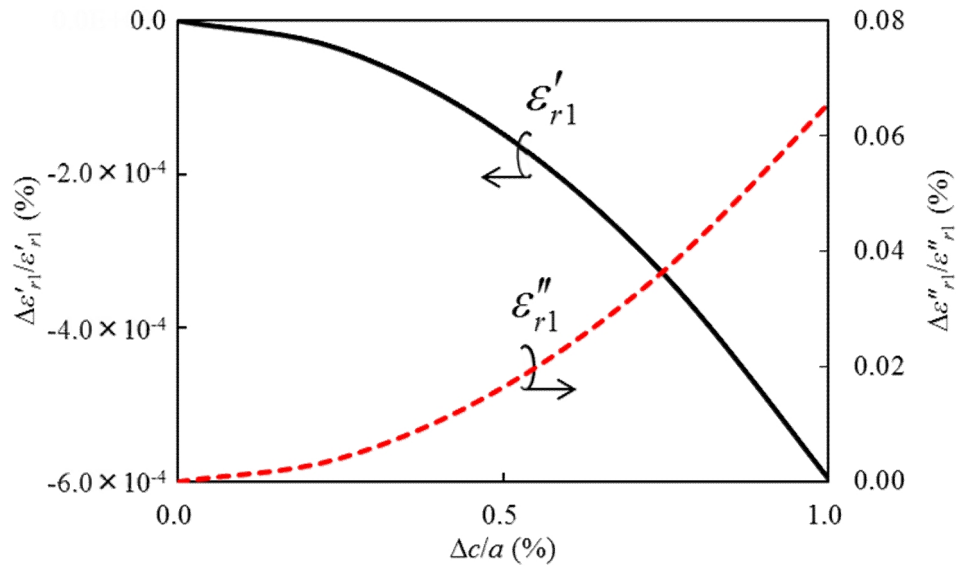
4.4 Error analysis of material estimation

In this evaluation method, the complex permittivities $\dot{\epsilon}_{r1}$ and $\dot{\epsilon}_{r2}$ of a two-layer sample are obtained by measuring the complex transmission parameters for different installation locations and/or orientations of the sample in the waveguide. Thus, it is required to estimate the errors due to uncertainties in the transverse-position, length and thickness measurements of the sample. The error analysis of the position is shown in Fig. 4-9, where the errors are caused by the deviation of the transverse position of the sample at layout B [Fig. 4-9(a)], while it is assumed that there is no deviation in position for the sample loaded adjacent to the sidewall (layout X; refer Fig. 4-4). The relative errors of the real ($\Delta\epsilon'_{r1}/\epsilon'_{r1}$) and imaginary ($\Delta\epsilon''_{r1}/\epsilon''_{r1}$) parts of the complex permittivity of the layer with higher loss (with higher $\tan \delta$) are $-5.97 \times 10^{-4}\%$ and $6.55 \times 10^{-2}\%$, respectively, for a 1% deviation in position $\Delta c/a$ ($\Delta c = 0.23$ mm), while $\Delta\epsilon'_{r2}/\epsilon'_{r2}$ and $\Delta\epsilon''_{r2}/\epsilon''_{r2}$ are $-6.36 \times 10^{-3}\%$ and 14.87% , respectively. The position errors of the complex permittivities of each layer are very small except for the imaginary part of $\dot{\epsilon}_{r2}$ of the low-loss layer ($\epsilon''_{r2} = 1.0 \times 10^{-3}$). Fig. 4-10 shows the relative error of the complex permittivities due to the deviation in sample length. For a 1% deviation in length $\Delta L_s/L_s$ ($\Delta L_s = 0.10$ mm), the relative error of $\Delta\epsilon'_{r1}/\epsilon'_{r1}$ and $\Delta\epsilon''_{r1}/\epsilon''_{r1}$ are 0.39% and 0.41% , respectively, while $\Delta\epsilon'_{r2}/\epsilon'_{r2}$ and $\Delta\epsilon''_{r2}/\epsilon''_{r2}$ are $-2.97 \times 10^{-2}\%$ and $-1.33 \times 10^2\%$, respectively. Fig. 4-11 shows the relative error of the complex permittivities due to the deviation in sample thickness. The relative error of $\Delta\epsilon'_{r1}/\epsilon'_{r1}$ and $\Delta\epsilon''_{r1}/\epsilon''_{r1}$ are 1.23% and -0.64% , respectively, while $\Delta\epsilon'_{r2}/\epsilon'_{r2}$ and $\Delta\epsilon''_{r2}/\epsilon''_{r2}$ are 0.47% and $6.02 \times 10^2\%$, respectively, for a 1% deviation in thickness $\Delta t_1/t_1$ ($\Delta t_1 = 0.05$ mm). The errors of the complex permittivities due to the sample

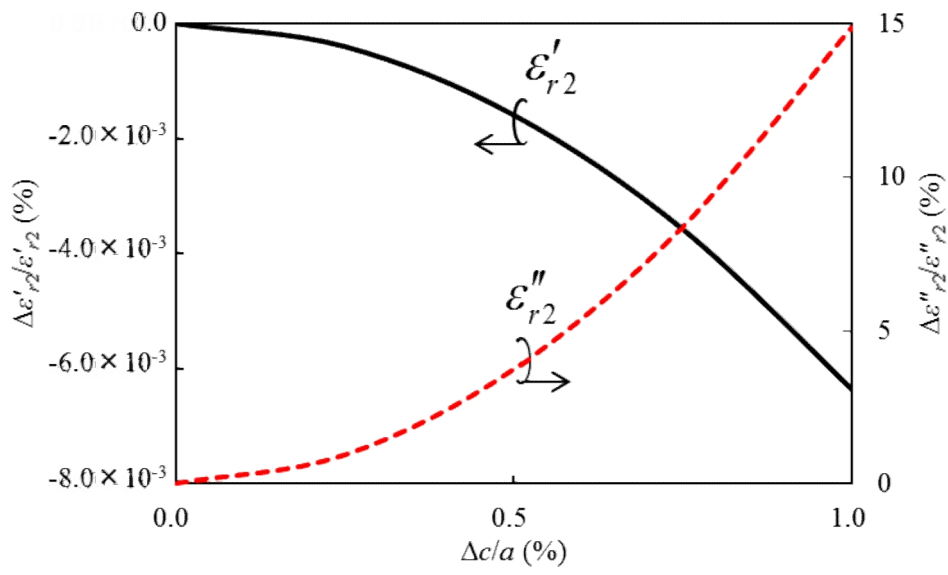
length deviation in Fig. 4-10 are smaller than those due to the sample thickness deviation in Fig. 4-11. This can be explained as follows. The electric field intensity has its maximum at the center of waveguide and decreases to zero at the sidewall (see Fig. 2-1). Therefore the increase in the sample size in a transverse (x) direction for layout B has less effect on the transmission parameters than that in the axial (z) direction does.



(a) Deviation of sample position.

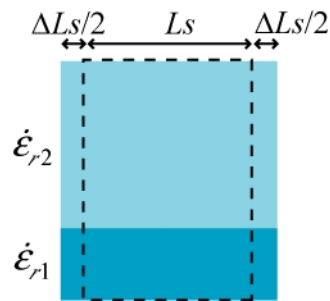


(b) Relative error of ϵ'_{r1} .

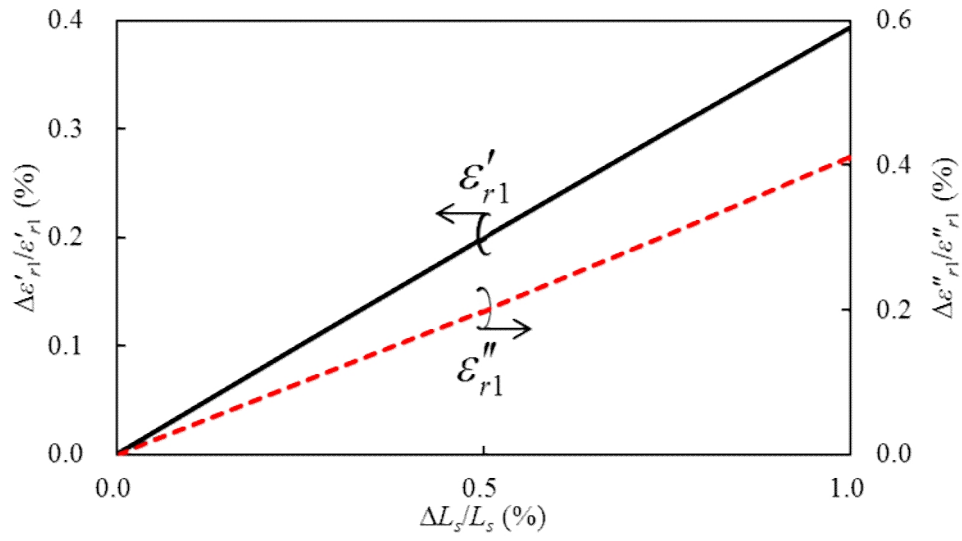


(c) Relative error of $\dot{\epsilon}_{r2}$.

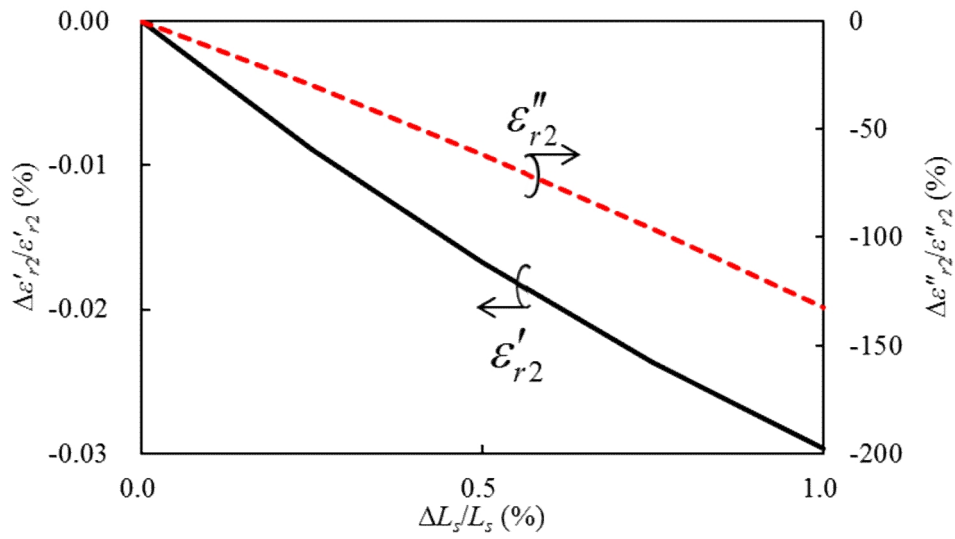
Fig. 4-9 Relative error of the complex permittivities caused by the deviation in position at 10 GHz. Sample size and permittivities are the same as sample 3 in Table 4-1.



(a) Deviation of sample length.

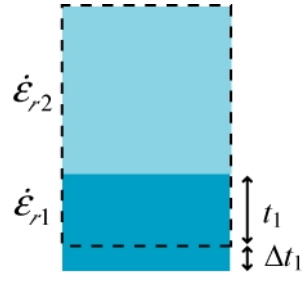


(b) Relative error of ϵ'_{r1} .

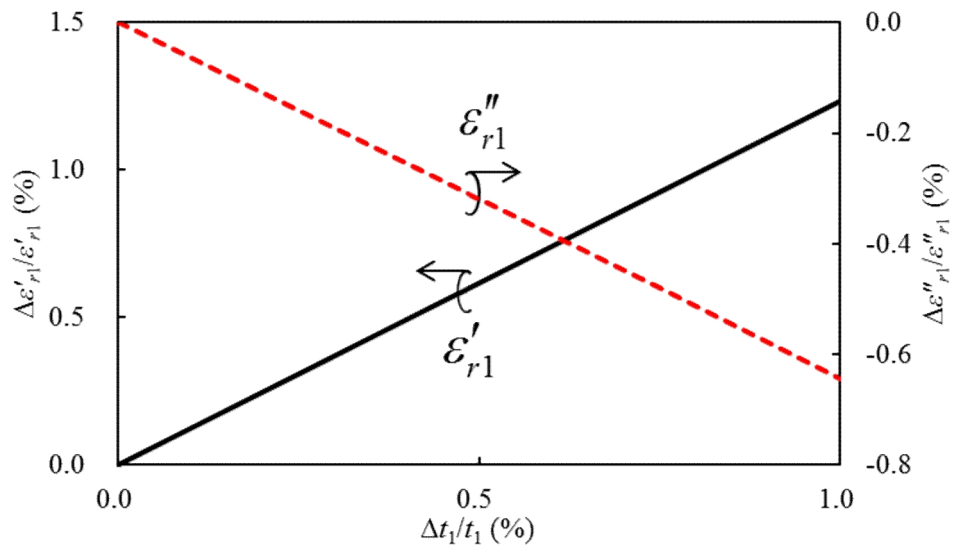


(c) Relative error of ϵ''_{r2} .

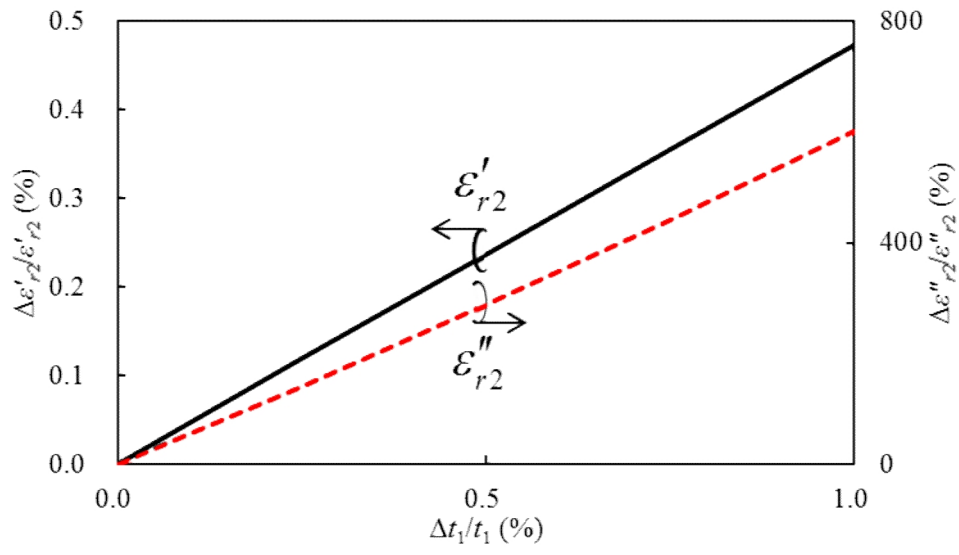
Fig. 4-10 Relative error of the complex permittivities caused by the deviation in sample length at 10 GHz. Sample size and permittivities are the same as sample 3 in Table 4-1.



(a) Deviation of sample thickness.



(b) Relative error of $\dot{\epsilon}_{r1}$.



(c) Relative error of ϵ'_{r2} .

Fig. 4-11 Relative error of the complex permittivities caused by the deviation in sample thickness at 10 GHz. Sample size and permittivities are the same as sample 3 in Table 4-1.

Chapter 5 Measurement Verification

5.1 Sample preparation and measurement setup

5.2 Calibration

5.3 Measured results

5.4 Discussion of applicability of present material assessment

Chapter 5 Measurement Verification

Real experiments are performed in this chapter to verify the material assessment procedure of the complex permittivities of a two-layer sample. The sample for measurement is composed of commercially available materials and measurement system is arranged by using the *X*-band waveguide and the waveguide to coax adapters (Section 5.1). Scattering parameters are measured by vector network analyzer (VNA) and calibration procedure for VNA is discussed in section 5.2. A measured result is reported in Section 5.3 and applicability of the material assessment procedure is discussed in section 5.4.

5.1 Sample preparation and measurement setup

A two-layer sample consisting of a 10.0-mm-thick teflon plate (EIKOH Co., LTD) and a commercially available 5.0-mm-thick microwave absorber is prepared manually as the sample under test (Fig. 5-1). The microwave absorber is a rubber plate containing carbon powder (TAKECHI Kogyogomu Co., LTD, Product no.: SI-100).

The experimental arrangement for the permittivity measurement is shown in Fig. 5-2(a) and specifications of experimental instruments are listed in Table 5-1. An *X*-band waveguide (type: WR-90; cross-section dimension: 22.86 mm \times 10.16 mm) is used as a sample holder, and top board can be detached and screwed tightly so that the sample can be located precisely [Fig. 5-2(b)]. Waveguide walls are coated with silver plating and the conductor loss is extremely small that average is -0.291 dB over frequency range 8 to 12 GHz for waveguide of 10 cm long. Also the effect of this conductor loss can be removed in this measurement method, which will be explained later. The cutoff frequencies of the dominant TE_{10} mode and the first higher-order (TE_{20}) mode of the empty waveguide are 6.56 and 13.11 GHz, respectively, and only the dominant TE_{10} mode propagates between these frequencies in the empty waveguide. The sample has the same height as the waveguide holder, so it settles in the waveguide and the measurement can be performed without the support structure. The sample-holding waveguide is connected to a vector network analyzer (Agilent 8719ET) via the coaxial-to-waveguide converters and cables. The waveguide is not equipped with a positioner for setting up the sample correctly, and thus a deviation in the transverse position is unavoidable. However, the error of the complex permittivities due to the deviation of the transverse-position is relatively small as shown in Fig. 4-9. To

determine the material parameters, the differences between S_{21} 's are measured with the sample loaded and unloaded instead of the values of S_{21} themselves, so that the position error in the axial direction is eliminated.

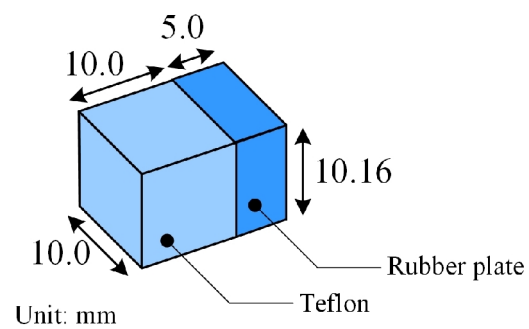
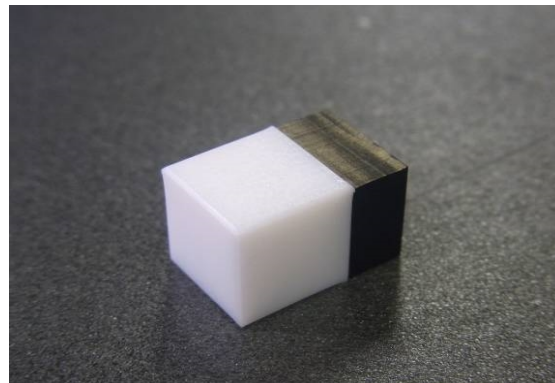
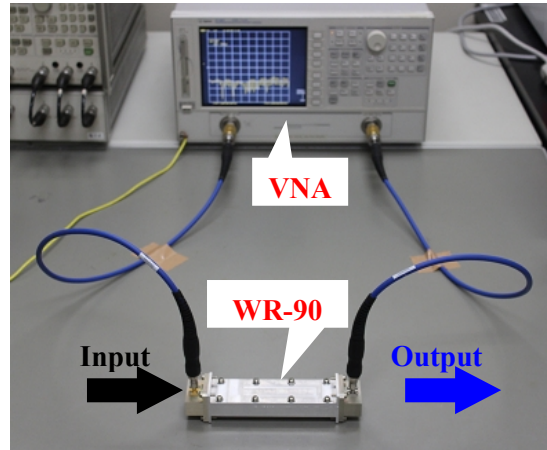
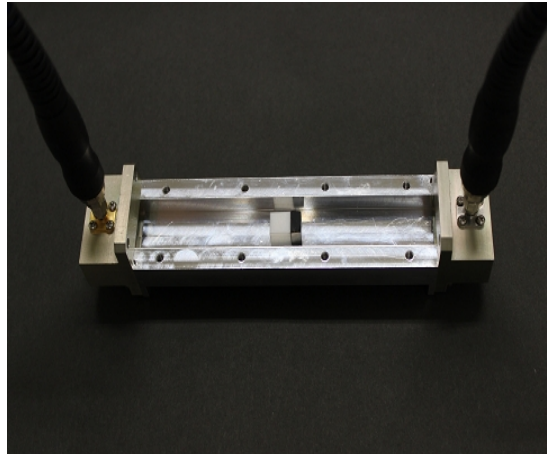


Fig. 5-1 Two-layer sample under test.



(a) *X*-band waveguide (WR-90) measurement system.



(b) Two-layer sample located inside sample holder.

Fig. 5-2 Experimental arrangement.

Table 5-1 Specification of experimental instruments.

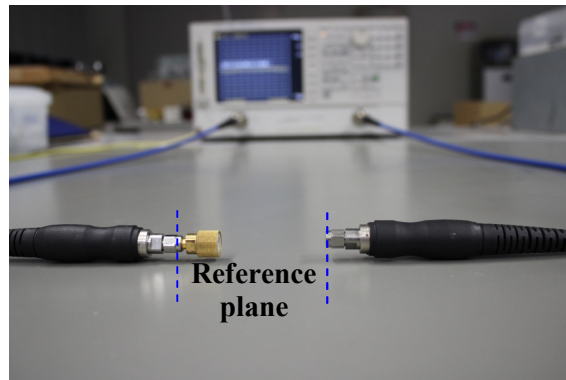
	Description
Vector network analyzer (VNA)	<p>Mfg.: Agilent Technologies</p> <p>Product no.: 8719ET</p> <p>Frequency range : 0.05 to 13.51 GHz</p> <p>Accuracy : ± 10 ppm</p> <p>Resolution : 1 Hz</p>
Coaxial cable	<p>Mfg.: Junkosha Inc.</p> <p>Product no.: MX122</p> <p>Characteristic impedance: 49.5 Ω</p> <p>Outer diameter: 6.5 mm</p> <p>Inner diameter: 3.5 mm</p> <p>Length: 1000 mm</p>
Coaxial-to-waveguide converters	<p>Mfg.: Pasternack Enterprises, Inc.</p> <p>Product no.: PE9804</p> <p>Frequency range: 8.2 to 12.4 GHz</p> <p>Connector impedance: 50 Ω</p> <p>Dimension: 25.4 \times 41.4 \times 41.4 mm</p>

5.2 Calibration

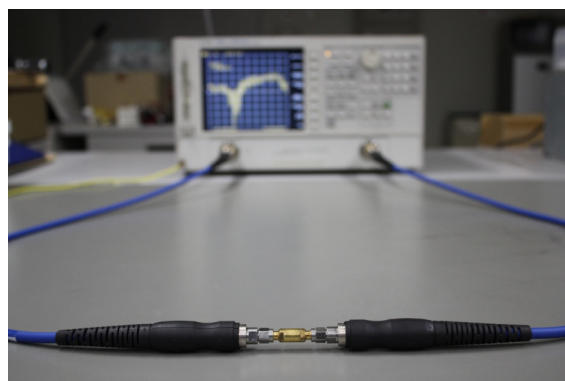
Scattering parameters can be measured by using vector network analyzer (VNA). However, accuracy of measurement is strongly dependent on the VNA calibration procedure. The most common of VNA calibrations is short-open-load-thru (SOLT) calibration algorithm, and it removes the systematic errors that may be produced by imperfections in the VNA and mismatch between VNA and input and output ports. In SOLT calibration, short, open and load standards shown in Fig. 5-3(a) is connected to the reference plane one by one and measured using VNA [Fig. 5-3(b)]. Then, two reference planes are connected using thru standard [Fig. 5-3(c)]. This calibration is susceptible to error since it involves many handling routines and also the calibration standards need to be well defined. Calibration-independent or less dependent technique is preferable to accurate and easy material measurements. The present material assessment procedure does not use the absolute value of S_{21} but use the difference between the loaded and unloaded transmission parameter S_{21} and it cancels out or reduces the error included in the uncalibrated measured S_{21} 's. Also, the use of the differences of S_{21} mitigates systematic errors caused by conductor loss on the waveguide-wall and the transition between the coaxial cable and waveguide.



(a) Calibration standards.



(b) Measurement of short, open and load standards.



(c) Measurement of thru standards.

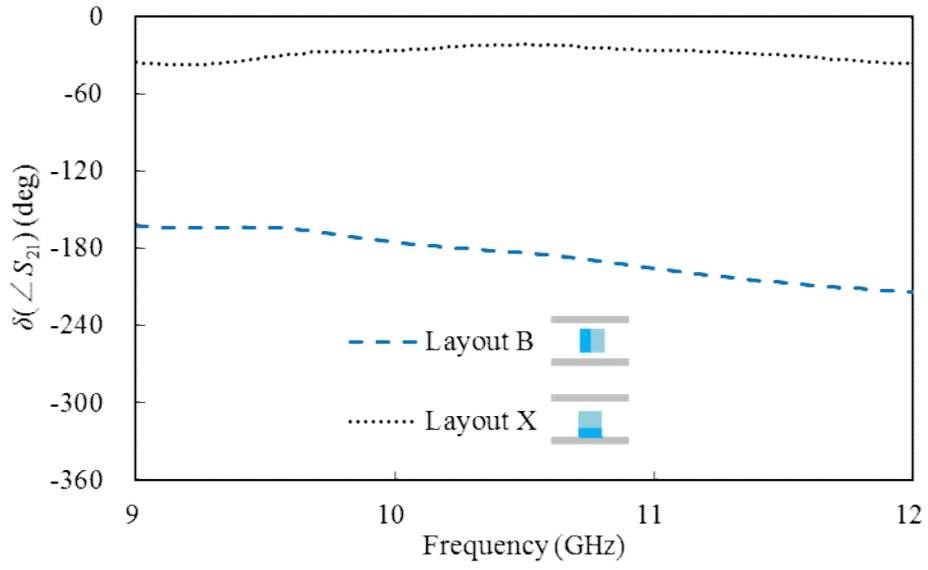
Fig. 5-3 SOLT calibration.

5.3 Measured results

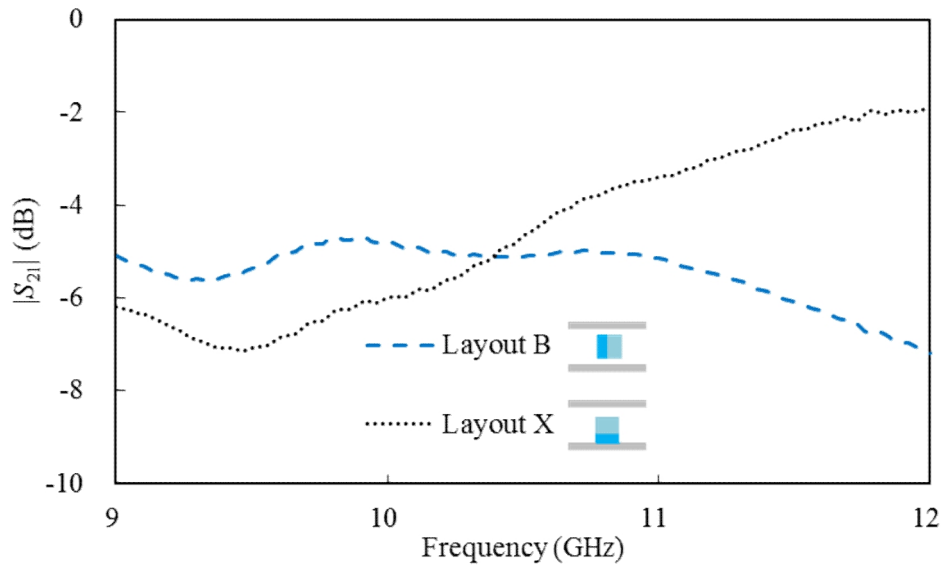
The frequency dependencies of complex transmission parameters of two-layer sample placed in the waveguide are measured for layouts B and X as shown in Fig. 5-4. 151 frequency points are measured spanning 9-12 GHz with steps of 0.02 GHz. No significance resonant is observed over broad frequency for both measured phase delay and amplitude of complex transmission parameter. These measured complex parameters are used to determine the complex permittivities of each layer of the sample by resorting to the material evaluation procedure explained in Fig. 4-6. The frequency dependencies of the complex permittivities $\dot{\epsilon}_{r1}$ and $\dot{\epsilon}_{r2}$ of each layer are shown in Fig. 5-5 (solid line). Total computational time to estimate the permittivities over frequency 9 to 12 GHz with 151 frequency points is 57496.63 secs. The sample is not cut into layers but the complex permittivities $\dot{\epsilon}_{r1}$ and $\dot{\epsilon}_{r2}$ of two-layer sample are evaluated simultaneously in the present method. For comparison, the sample is cut into layers, and $\dot{\epsilon}_{r1}$ and $\dot{\epsilon}_{r2}$ of each layer are measured separately as one-layer dielectric sample. The measured results are included in Fig. 5-5(a) ('×' mark). A good agreement is observed between the measured results over the frequency range except for ϵ''_{r2} , as expected from the virtual experiments in Figs. 4-9 – 4-11. The resolution limit observed in the characterization of low-loss materials is a common drawback of transmission-line techniques using coaxial cable, waveguide, and striplines. The complex permittivities $\dot{\epsilon}_{r1}$ and $\dot{\epsilon}_{r2}$ of each layer are also measured by using the resonant method (mono-frequency method) [34], [35], and the results are included in Fig. 5-5(a) ('•' mark). In conventional resonant method, it is difficult to evaluate the lossy sample precisely. In [34], sample is loaded partially in resonator similar to the present method,

and the evaluation of lossy material is available by resonant method but the measurement is limited to only single-layer material at one frequency. This is another confirmation of accuracy of the present method.

The principle of the present method is calibration-independent as explained in section 5.2. The material assessment is performed using uncalibrated and calibrated complex transmission parameters, and both results are in good agreement though slight differences exist in the higher frequencies as shown in Fig. 5-5(b).

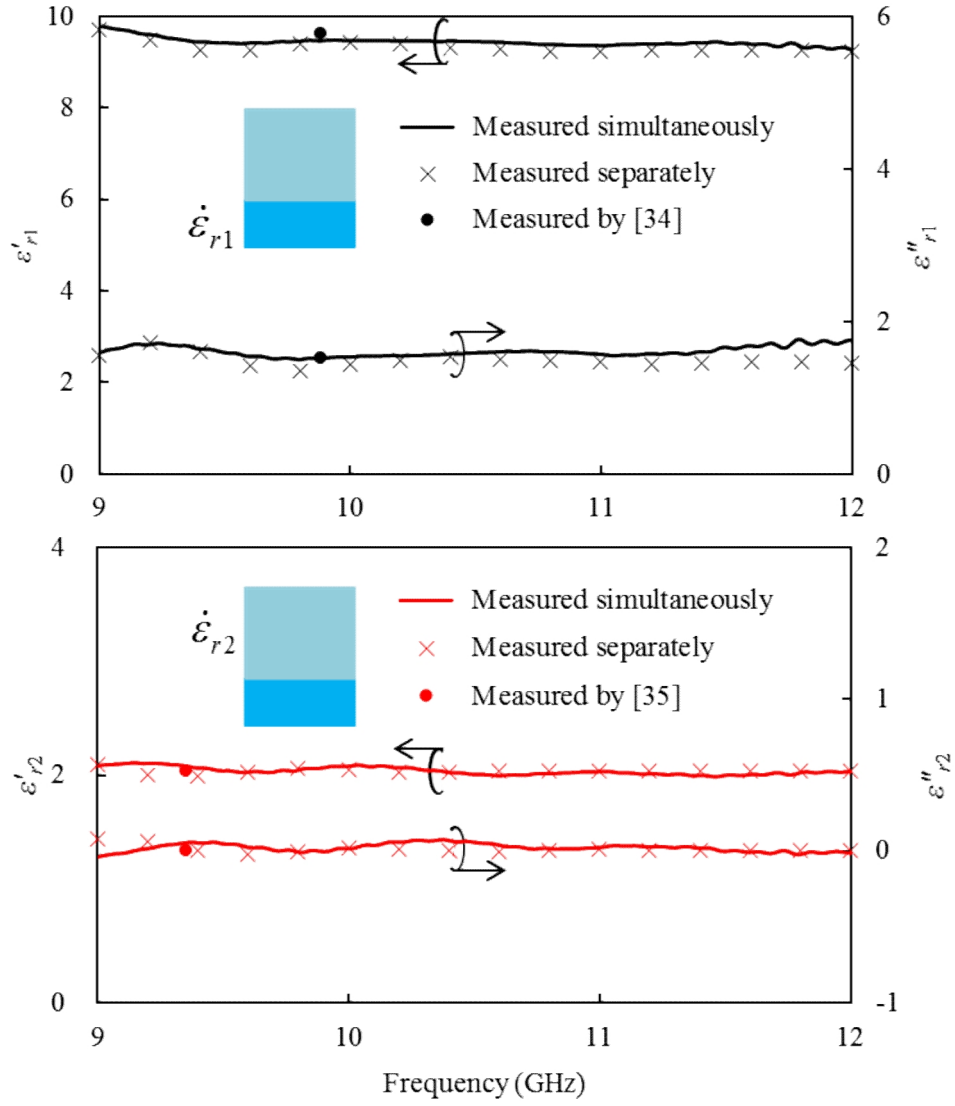


(a) Phase delay of complex transmission parameter.

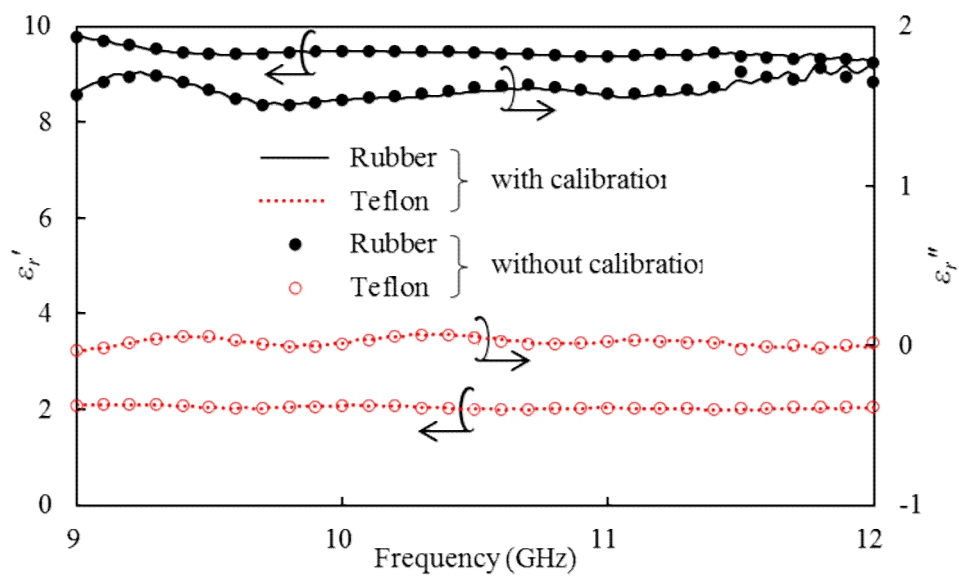


(b) Amplitude of complex transmission parameter.

Fig. 5-4 Measured complex transmission parameter of a two-layer sample loaded in the waveguide.



(a) Comparison with values of divided sample. Two-layer sample is divided into homogeneous layers and each layer is measured separately by the resonant method.



(b) Comparison of calibrated and uncalibrated measured permittivities.

Fig. 5-5 Frequency dependencies of measured permittivities.

5.4 Discussion of applicability of present material assessment

The material evaluation is based on the accurate electromagnetic formulation procedure explained. It does not include any approximation for simplicity as explained in chapter 2 and is able to evaluate the scattering characteristics of wide variety of two-layer samples of electrically large or small with the high or low permittivities, and high or low losses. The usefulness and versatility of the present method is investigated numerically in Figs. 5-6 and 5-7. Fig. 5-6 shows the scattering characteristics of the two-layer sample whose size and permittivities are the same as sample 3 in Table 4-1, except for the complex permittivity of layer 2, ϵ_{r2} , which is changed from lossless ($\tan \delta = 0$) to highly lossy ($\tan \delta = 2$) cases. When the layer with high loss is placed near the center of waveguide, the amplitude of the complex transmission parameter becomes very weak ($|S_{21}| < -40$ dB) and reduces the accuracy of the evaluation results (solid line in Fig. 5-6). This can be solved by using layout Z turning over the sample and placing the layer with higher loss next to the waveguide sidewall as shown in Fig. 5-6. S_{21} is affected more by ϵ_{r1} and influenced less by ϵ_{r2} of highly lossy layer 2 for this layout (dotted line). ϵ_{r2} can be assessed mainly by using the complex transmission parameter S_{21} for layout B (broken line).

If both layers of the sample are very thin and placed next to the waveguide sidewall (layout X), where the electric field is weakest, then the difference between the loaded and unloaded complex transmission parameter S_{21} is too small to perform the accurate material evaluation. However, close contact to the sidewall is not necessarily required in the material evaluation, but the sample is placed parallel to the guide wall leaving an appropriate space between the sample and sidewall. Fig. 5-7 shows the phase

delay of S_{21} between the loaded and unloaded waveguide $\delta(\angle S_{21}) = \angle S_{21}^L - \angle S_{21}^U$ for the sample with very thin layers changing the space between the sample and sidewall, D_1 . When the sample is placed next to the waveguide sidewall ($D_1 = 0$ mm), $\delta(\angle S_{21})$ is negligibly small, but it becomes appreciable with increase in space D_1 .

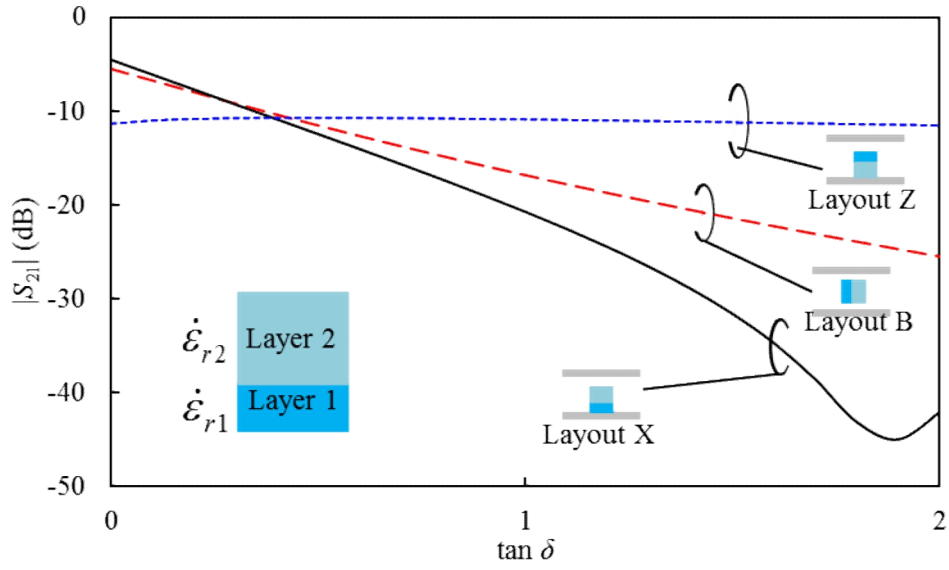


Fig. 5-6 Amplitude of scattering parameters of a sample with lossy layers.

$$\dot{\epsilon}_{r1} = 10.0 - j2.0, \quad \dot{\epsilon}_{r2} = 2.0(1 - j \tan \delta), \quad f = 10 \text{ GHz}.$$

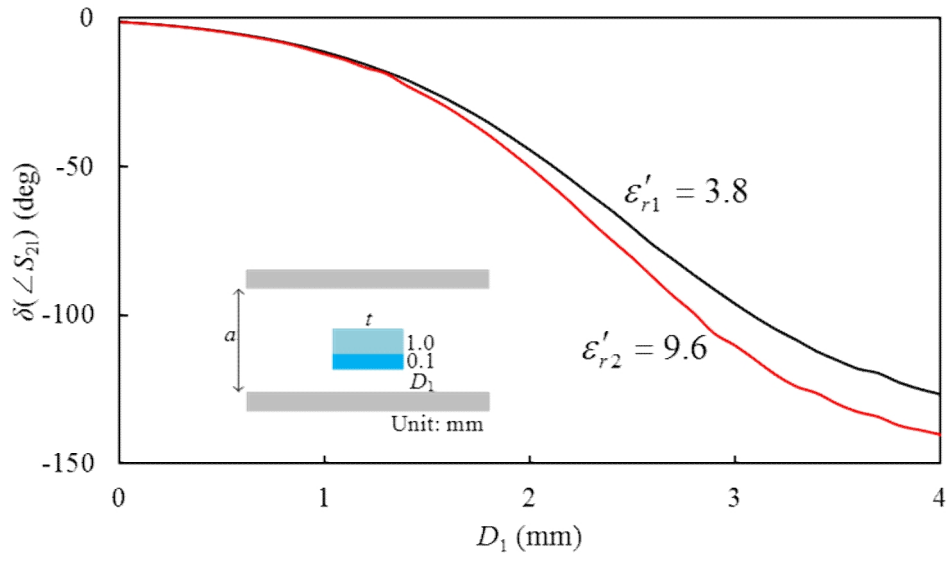


Fig. 5-7 Phase delay of scattering parameters of a sample with thin layers.

$\epsilon'_{r1} = 3.8, \epsilon'_{r2} = 9.6, t = 20.0$ mm, $a = 22.86$ mm, $f = 10$ GHz.

Chapter 6 Conclusions

A frequency-dependent measurement method has been proposed to determine the individual complex permittivities of a two-layer lossy sample accurately and efficiently. In this method, the sample fills only a part of the waveguide cross-section and thus precise machining of the sample is not required. Unknown complex permittivities of a two-layer sample are evaluated by measuring transmission parameters for two different locations and/or orientations of the sample in the waveguide cross-section.

The inhomogeneous field distribution of the waveguide mode is utilized advantageously and only the transmission parameter, S_{21} , is measured for the material evaluation. The complex reflection parameter, S_{11} , which is more difficult to measure, is not required in this evaluation method. The proposed method is used to characterize samples with a high-loss layer, as the partial loading of lossy samples makes the measured S_{21} at adequate level.

This material estimation is based on the accurate and numerically efficient hybrid electromagnetic method. Analytical formulation of this method has adopted the aperture electric fields as source quantities but the aperture magnetic fields are introduced and dual electromagnetic formulation is developed in this work. Any approximation is not included in these formulation procedures, the precision of solution

can be systematically improved as the number of basis functions which express the source quantities. The values using the complementary source quantities approach the limiting value from above and below for a wide variety of materials with various size and layout of samples. This results can be used to limit the error range of the numerical computations. The computed value with a sufficient number of basis functions is compared with rigorous solution when available and if not, it is compared with FEM, and good agreement is observed in all structures. The matrix size used to calculate the transmission parameters is much smaller than those in FEM and the conventional mode-matching method. The high-precision and numerically efficient hybrid electromagnetic method is suitable to versatile material assessment.

A material evaluation algorithm is developed based on the hybrid electromagnetic analysis method. The procedure uses an efficient and stable iterative algorithm to determine the complex permittivities of two-layer sample from the measured complex transmission parameters for two different locations and/or orientations of single sample.

The proposed material evaluation algorithm is verified by virtual and actual experiments. Various materials are tested in virtual experiment to evaluate the permittivities and the prescribed complex permittivities of tested materials are reconstructed accurately by the material evaluation algorithm revealing high accuracy and versatility of the present method. Also various initial values are tested in virtual experiment and accurate reproduction is observed even with a significant mismatch initial value confirming the robustness of the material evaluation algorithm. The iterative procedure to obtain the complex permittivities shows a rapid convergence with

only several repetition even when the initial value largely mismatches from the true value. Virtual experiments demonstrate the accuracy, versatility, efficiency and robustness of the present method. Virtual experiments also clarify the errors due to the uncertainties during material evaluation such as deviation in sample location, length and thickness and show that these errors are less affected in the present measurement method.

The real measurement is performed for two-layer sample. The sample including a high-loss layer is prepared and the complex permittivities are measured over X -band frequencies. The measurement shows the accuracy of the present and also demonstrates that the present method is calibration-independent.

References

- [1] J. Zhong, S. Liang, Q. Xiong, Y. Yuan, and C. Zeng, "A State Space Representation for One-Dimensional Microwave Heating Temperature Model," *SICE Annual Conference*, Hokkaido University, Sapporo, Japan, 2014, pp. 1366-1371.
- [2] H. Zhang, A. K. Datta, I. A. Taub, C. Doona, "Electromagnetics, Heat Transfer, and Thermokinetics in Microwave Sterilization," *AIChE J.*, vol. 47, no. 9, Sep. 2001, pp. 1957-1968.
- [3] M. Kinoshita, K. Shimaoka, and K. Komiyama, "Atomic microwave power standard based on the Rabi frequency," *IEEE Trans. Instrum. Meas.*, vol. 60, no. 7, Jul. 2011, pp. 2696–2701.
- [4] J. T. Senise and L. A. Jermolovicius, "Microwave chemistry – a fertile field for scientific research and industrial applications", *J. Microwaves, Optoelectronics and Electromagnetic Applications*, vol 3, Sep. 2003, pp. 97-112.
- [5] A. W. Kraszewski and S. O. Nelson, "Application of microwave techniques in agricultural research," in *Proc. SBMO/IEEE MTT-S Int. Microw. Optoelectron. Conf.*, vol. 1, Athens, GA, 1995, pp. 117–126.
- [6] F. Sterzer, "Microwave medical devices," *IEEE Microw. Mag.*, vol. 3, no. 1, Mar. 2002, pp. 65–70.
- [7] A. M. Nicolson and G. F. Ross, "Measurement of the intrinsic properties of materials by time domain techniques," *IEEE Trans. Instrum. Meas.*, vol. IM-19, no. 4, Nov. 1970, pp. 377-382.
- [8] W. B. Weir, "Automatic measurement of complex dielectric constant and permeability at microwave frequencies," *Proc. IEEE*, vol. 62, no. 1, Jan. 1974, pp. 33-36.
- [9] U. C. Hasar, "A new calibration-independent method for complex permittivity extraction of solid dielectric materials," *IEEE Microw. Wireless Compon. Lett.*, vol. 18, no. 12, Dec. 2008, pp. 788-790.
- [10] K. S. Champlin and G. H. Glover, " 'Gap effect' in measurement of large permittivities," *IEEE Trans. Microwave Theory Techn.*, vol. 14, Aug. 1966, pp. 397–398.
- [11] J. M. Catalá-Civera, A. J. Canós, F. L. Peñaranda-Foix, and E. R. Davó, "Accurate determination of the complex permittivity of materials with transmission reflection measurements in partially filled rectangular waveguides," *IEEE Trans. Microwave Theory Techn.*, vol. 51, no. 1, Jan. 2003, pp. 16-24.
- [12] A. Nishikata, "A swept-frequency measurement of complex permittivity and complex permeability of a columnar specimen inserted in a rectangular waveguide," *IEEE Trans. Microwave Theory Techn.*, vol. 55, no. 7, July 2007, pp. 1554-1567.
- [13] S. Yoshikado and I. Taniguchi, "Microwave complex conductivity of a square post in rectangular waveguide," *IEEE Trans. Microwave Theory Techn.*, vol. 37, no. 6, Jun. 1989, pp. 984–992.

- [14] H. Miyagawa, T. Sawai, K. Wakino, Y. D. Lin, and T. Kitazawa, "Simultaneous Determination of Complex Permittivity and Permeability of Columnar Materials with Arbitrarily Shaped Cross-Section," *IEEE Trans. Microwave Theory Techn.*, vol. 57, no. 9, Aug 2009, pp. 2249-2256.
- [15] J. Baker-Jarvis, M. D. Janezic, B. F. Riddle, R. T. Johnk, P. Kabos, C. L. Holloway, R. G. Geyer, and C. A. Grosvenor, "Measuring the permittivity and permeability of lossy materials: Solids, liquids, metals, building materials and negative-index materials," National Institute of Standards and Technology, Boulder, CO, Tech. Note 1536, 2004.
- [16] J. Baker-Jarvis, "Transmission/reflection and short-circuit line permittivity measurements," National Institute of Standards and Technology, Boulder, CO, Tech. Note 1341; 1990.
- [17] D. L. Faircloth, M. E. Baginski, and S. M. Wentworth, "Complex Permittivity and Permeability Extraction for Multilayered Samples Using S-Parameter Waveguide Measurements," *IEEE Trans. Microw. Theory Techn.*, vol. 54, no. 3, Mar. 2006, pp. 1201-1209.
- [18] F. Akleman, "Reconstruction of complex permittivity of a longitudinally inhomogeneous material loaded in a rectangular waveguide," *IEEE Microw. Wireless Compon. Lett.*, vol. 18, no. 3, Mar. 2008, pp. 158–160.
- [19] E. Kılıç, U. Siart and T. F. Eibert, "Regularized 1-D Dielectric Profile Inversion in a Uniform Metallic Waveguide by Measurement and Simulation," *IEEE Trans. Microw. Theory Techn.*, vol. 60, no. 5, May 2012, pp. 1437-1443.
- [20] M. W. Hyde and M. J. Havrilla, "Electromagnetic characterization of two-layer dielectrics using two flanged rectangular waveguides," in *IEEE Instrumentation and Measurement Technology Conf. Proc.*, May 2008, pp. 1648 - 1652.
- [21] P. Queffelec, V. Laur, A. Chevalier, J.-M. Le Floch, D. Passerieux, D. Cros, V. Madrangeas, A. Le Febvrier, S. Députier, M. Guilloux-Viry, G. Houzet, T. Lacrevez, C. Bermond and B. Fléchet, "Intercomparison of permittivity measurement techniques for ferroelectric thin layer," *J. Appl. Phys.*, vol. 115, no. 2, 2014, pp. 024103-1 - 024103-9.
- [22] T. Kitazawa, "Nonreciprocity of phase constants, characteristics impedances, and conductor losses in planar transmission lines with layered anisotropic media," *IEEE Trans. Microw. Theory Tech.*, vol. 43, no. 2, Feb. 1995, pp. 445–451.
- [23] T. Kitazawa, Y. Hayashi, and M. Suzuki, "Analysis of the dispersion characteristics of slot line with thick metal coating," *IEEE Trans. Microw. Theory Tech.*, vol. MTT-28, no. 4, Apr. 1980, pp. 387–392.
- [24] T. Shiraishi, T. Nishikawa, K. Wakino, and T. Kitazawa, "An efficient analysis of lossless and lossy discontinuities in waveguide using hybrid numerical method," *IEICE Trans. Electron.*, vol. E86-C, no. 11, Nov. 2003, pp. 2184–2190.

- [25] M. S. B. A. Karim, Y. Konishi, K. Harafuji, and T. Kitazawa, "Determination of complex permittivities of layered materials using waveguide measurements," *IEEE Trans. Microwave Theory Techn.*, vol. 62, no. 9, Sep. 2014, pp. 2140-2148.
- [26] M. S. B. A. Karim and T. Kitazawa, "Determination of material parameters based on hybrid numerical methods using complementary source quantities," *IEICE Trans. Electron.*, vol. J98-C, no. 12, Dec. 2015, pp. 356 - 365.
- [27] M. S. B. A. Karim, Y. Konishi, and T. Kitazawa, "Robustness analysis of simultaneous determination method of complex permittivity and permeability," in *IEEE NEMO 2014 Proc.*, Italy, May 2014, pp. 171-174.
- [28] S. Gaál, E. Lörincz, P. I. Ritcher, M. Barabás, "Assessment of the point matching method for waves in uniaxially anisotropic materials," *Optics Communications*, vol. 155, Oct. 1998, pp. 368-375.
- [29] H. Esteban, S. Cogollos, A. Vidal, V. E. Boria, and M. Ferrando, "A new hybrid mode-matching method for the analysis of inductive obstacles and discontinuities," in *Proc. IEEE AP-S Int. Symp.*, vol. 2, Jul. 1999, pp. 966-969.
- [30] C-K. C. Tzuang, C-D. Chen, and S-T. Peng, "Full-wave analysis of lossy quasi-planar transmission line incorporating the metal modes," *IEEE Trans. Microw. Theory Tech.*, vol. MTT-38, Dec. 1990, pp. 1792-1799.
- [31] R. F. Harrington, *Time-Harmonic Electromagnetic Fields*, New York, NY, USA: *IEEE Press*, ch. 3, sec. 3-5, 2001, pp. 106-110.
- [32] M. S. B. A. Karim, T. Kitazawa, K. Wakino, H. H. Su and C-W. Kuo, "Design of rectangular cavity by extended spectral domain approach," in *PIERS 2012 Proc.*, Kuala Lumpur, Mar. 2012, p. 676.
- [33] M. D. Deshpande and K. Dudley, "Estimation of complex permittivity of composite multilayer material at microwave frequency using waveguide measurements," NASA Langley Research Center, Hampton, VA, USA, NASA Technical Memorandum 212398, 2003.
- [34] M. Kinoshita, H. Kinouchi, M. S. B. A. Karim, K. Wakino, T. Kitazawa, "A method of evaluating high-permittivity and lossy materials using a cylindrical cavity based on hybrid electromagnetic theory," *J. Appl. Phys.*, vol. 51, no. 9, 2012, pp. 09LF03-1 - 09LF03-5.
- [35] N. Nakao, Y. Morishita, K. Wakino, T. Kitazawa, S. Imai, K. Taguchi, T. Kashiwa, M. Suzuki, K. Fujii, "An adaptive evaluation method of material with complex permittivity in a cylindrical cavity," *International Symposium on Antennas and Propagation*, Macau, 2010, pp. 1025-1028.

Appendix

Appendix 1 Derivation of amplitudes R , T , A_m and D_m

Eqs. (8) and (11) are modal expansions of electromagnetic field with amplitudes R , T , A_m and D_m . These amplitudes R , T , A_m and D_m are derived from eq. (12-a) as follows.

$$(-1 + R) \frac{\beta_1}{\omega\mu_0} E_0 F_1(x) + \sum_{m=2}^{\infty} A_m E_0 \frac{\gamma_m}{j\omega\mu_0} F_m(x) = h_a(x) \quad (\text{A-1})$$

By multiplying both sides of eq. (A-1) with $F_1(x)$ and integrating it over $0 \leq x \leq a$,

$$\begin{aligned} (-1 + R) \frac{\beta_1}{\omega\mu_0} E_0 \int_0^a F_1(x) F_1(x) dx + \sum_{m=2}^{\infty} A_m E_0 \frac{\gamma_m}{j\omega\mu_0} \int_0^a F_m(x) F_1(x) dx \\ = \int_0^a h_a(x) F_1(x) dx. \end{aligned} \quad (\text{A-2})$$

Then by applying the orthogonality of $F_m(x)$ shown in eq. (7),

$$(-1 + R) \frac{\beta_1}{\omega\mu_0} E_0 = \int_0^a h_a(x) F_1(x) dx. \quad (\text{A-3})$$

R can be obtained as

$$R = \frac{\omega\mu_0}{\beta_1 E_0} \int_0^a h_a(x) F_1(x) dx + 1. \quad (\text{A-4})$$

T , A_m and D_m can be derived from eqs. 13(b)-13(d) by using similar procedure.

Appendix 2 Derivation of eq. (14)

Amplitudes R , T , A_m and D_m of modal expansions of electromagnetic fields [eqs. (8) and (11)] are derived in Appendix 1. Electromagnetic field are expressed in terms of aperture fields by substituting these amplitudes R , T , A_m and D_m into eqs. (8) and (11). Integral variable x in eq. (13) is denoted as x' to distinguish it from variable x in eqs. (8) and (11) in the substitution. As an example, $E_y^{(I)}(x, z)$ in eq. (8-a) can be rewritten as

$$\begin{aligned}
 E_y^{(I)}(x, z) &= E_0 F_1(x) e^{-j\beta_1(z-z_1)} + E_0 F_1(x) e^{+j\beta_1(z-z_1)} \\
 &\quad + \int_0^a \left\{ E_0 \frac{\omega\mu_0}{\beta_1 E_0} F_1(x) F_1(x') e^{+j\beta_1(z-z_1)} \right\} h_a(x') dx \\
 &\quad + \int_0^a \sum_{m=2}^{\infty} \left\{ E_0 \frac{j\omega\mu_0}{\gamma_m E_0} F_m(x) F_m(x') e^{+\gamma_m(z-z_1)} \right\} h_a(x') dx \\
 &= E^{in}(x, z) + \int_0^a Z^{(I)}(x, z | x', z_1) h_a(x') dx'.
 \end{aligned} \tag{A-5}$$

Other electromagnetic fields can be derived similarly [eqs. 14(b)-14(d)].

Appendix 3 Derivation of determinantal equation of eigenvalues [eq. (22)] and continuity of phase at the boundaries

Electromagnetic fields in region (II) are expressed in terms of eigenfunctions

$\Phi_m(x)$ as [see eq. (20)]

$$E_y(x, z) = \sum_{m=1}^{\infty} \Phi_m(x) \tilde{E}_m(z), \quad (\text{A-6})$$

$$H_z(x, z) = \frac{-1}{j\omega\mu_i} \frac{\partial}{\partial x} E_y = \sum_{m=1}^{\infty} \left\{ \frac{-1}{j\omega\mu_i} \frac{\partial}{\partial x} \Phi_m(x) \right\} \tilde{E}_m(z), \quad (\text{A-7})$$

$$\Phi_m(x) = \begin{cases} c_{1m} \frac{\sin(\alpha_{1m}x)}{\cos(\alpha_{1m}W_1)} & (0 \leq x \leq W_1), \\ \frac{c_{21m} \cos\{\alpha_{2m}(x-W_1)\} + c_{22m} \sin\{\alpha_{2m}(x-W_1)\}}{\cos(\alpha_{2m}W_2)} & (W_1 \leq x \leq W_1+W_2), \\ \frac{c_{31m} \cos\{\alpha_{3m}(x-W_1-W_2)\} + c_{32m} \sin\{\alpha_{3m}(x-W_1-W_2)\}}{\cos(\alpha_{3m}W_3)} & (W_1+W_2 \leq x \leq a-W_4), \\ c_{4m} \frac{\sin\{\alpha_{4m}(x-a)\}}{\cos(\alpha_{4m}W_4)} & (a-W_4 \leq x \leq a), \end{cases} \quad (\text{A-8})$$

where c_{1m} , c_{21m} , c_{22m} , c_{31m} , c_{32m} and c_{4m} are unknown coefficients and α_{1m} , α_{2m} , α_{3m} and α_{4m} are unknown eigenvalues. The eigenvalue equations are derived from the continuity conditions at the interfaces between the subregions. By applying the boundary condition of $E_y(x, z)$ and $H_z(x, z)$ at $x = W_1$, then

$$\begin{aligned} c_{1m} \frac{\sin(\alpha_{1m}W_1)}{\cos(\alpha_{1m}W_1)} &= \frac{c_{21m}}{\cos(\alpha_{2m}W_2)} \\ c_{1m} \frac{\sin(\alpha_{1m}W_1)}{\cos(\alpha_{1m}W_1)} - c_{21m} \frac{1}{\cos(\alpha_{2m}W_2)} &= 0, \end{aligned} \quad (\text{A-9})$$

and

$$\begin{aligned} \frac{\alpha_{1m} c_{1m}}{\mu_1} \frac{\cos(\alpha_{1m} W_1)}{\cos(\alpha_{1m} W_1)} &= \frac{\alpha_{2m} c_{22m}}{\mu_2} \frac{1}{\cos(\alpha_{2m} W_2)} \\ \frac{\alpha_{1m} c_{1m}}{\mu_1} - \frac{\alpha_{2m} c_{22m}}{\mu_2} \frac{1}{\cos(\alpha_{2m} W_2)} &= 0. \end{aligned} \quad (\text{A-10})$$

These equations are corresponding to the first and fourth row of eq. (22), respectively.

By applying the boundary condition of $E_y(x, z)$ and $H_z(x, z)$ at $x = W_1 + W_2$ and $x = a - W_4$, other elements in matrix $[A]$ of eq. (22) can be obtained.

Propagation constant along the z -direction in subregion i with (ε_i, μ_i) and eigenvalue α_{im} can be written as

$$\beta_{im} = \sqrt{(\alpha_{im})^2 - \omega^2 \varepsilon_i \mu_i}. \quad (\text{A-11})$$

Electromagnetic fields in all subregion have to propagate coincidentally along the z -direction, then

$$\sqrt{(\alpha_{1m})^2 - \omega^2 \varepsilon_1 \mu_1} = \sqrt{(\alpha_{2m})^2 - \omega^2 \varepsilon_2 \mu_2} = \sqrt{(\alpha_{3m})^2 - \omega^2 \varepsilon_3 \mu_3} = \sqrt{(\alpha_{4m})^2 - \omega^2 \varepsilon_4 \mu_4}. \quad (\text{A-12})$$

Appendix 4 Orthogonality and normalization of eigenfunction $\Phi_m(x)$.

It is proved in the following that eigenfunctions $\Phi_m(x)$ in sample holding region satisfy bi-orthogonal relation with the permeabilities in subregions μ_{ri} as the weight function

$$\int_0^a \frac{\Phi_m(x) \Phi_n(x)}{\mu_{ri}} dx = 0 \quad (m \neq n). \quad (\text{A-13})$$

Eigenfunctions (A-8) are substituted into the left hand of above equation as

$$\begin{aligned} & \int_0^a \frac{\Phi_m(x) \Phi_n(x)}{\mu_{ri}} dx \quad (m \neq n) \\ &= \int_0^{W_1} \frac{\Phi_m(x) \Phi_n(x)}{\mu_{r1}} dx + \int_{W_1}^{W_1+W_2} \frac{\Phi_m(x) \Phi_n(x)}{\mu_{r2}} dx + \int_{W_1+W_2}^{a-W_4} \frac{\Phi_m(x) \Phi_n(x)}{\mu_{r3}} dx + \int_{a-W_4}^a \frac{\Phi_m(x) \Phi_n(x)}{\mu_{r4}} dx \\ &= \frac{c_{1m} c_{1n}}{\mu_{r1} \cos(\alpha_{1m} W_1) \cos(\alpha_{1n} W_1)} \int_0^{W_1} \sin(\alpha_{1m} x) \sin(\alpha_{1n} x) dx \\ &+ \frac{1}{\mu_{r2} \cos(\alpha_{2m} W_2) \cos(\alpha_{2n} W_2)} \int_{W_1}^{W_1+W_2} \left[c_{21m} \cos\{\alpha_{2m}(x-W_1)\} + c_{22m} \sin\{\alpha_{2m}(x-W_1)\} \right] \\ &\quad \left[c_{21n} \cos\{\alpha_{2n}(x-W_1)\} + c_{22n} \sin\{\alpha_{2n}(x-W_1)\} \right] dx \\ &+ \frac{1}{\mu_{r3} \cos(\alpha_{3m} W_3) \cos(\alpha_{3n} W_3)} \int_{W_1+W_2}^{a-W_4} \left[c_{31m} \cos\{\alpha_{3m}(x-W_1-W_2)\} + c_{32m} \sin\{\alpha_{3m}(x-W_1-W_2)\} \right] \\ &\quad \left[c_{31n} \cos\{\alpha_{3n}(x-W_1-W_2)\} + c_{32n} \sin\{\alpha_{3n}(x-W_1-W_2)\} \right] dx \\ &+ \frac{c_{4m} c_{4n}}{\mu_{r4} \cos(\alpha_{4m} W_4) \cos(\alpha_{4n} W_4)} \int_{a-W_4}^a \sin\{\alpha_{4m}(x-a)\} \sin\{\alpha_{4n}(x-a)\} dx. \end{aligned} \quad (\text{A-14})$$

The integrals in (A-14) are performed easily as

$$\begin{aligned}
& \int_0^a \frac{\Phi_m(x) \Phi_n(x)}{\mu_{ri}} dx \quad (m \neq n) \\
&= \frac{1}{\alpha_{1m}^2 - \alpha_{1n}^2} \frac{c_{1m} c_{1n}}{\mu_{r1}} [\alpha_{1n} \tan(\alpha_{1m} W_1) - \alpha_{1m} \tan(\alpha_{1n} W_1)] \\
&\quad - \frac{1}{\alpha_{3m}^2 - \alpha_{3n}^2} \frac{\alpha_{3m} c_{32m} c_{31n}}{\mu_{r3} \cos(\alpha_{3m} W_3) \cos(\alpha_{3n} W_3)} \\
&\quad + \frac{1}{\alpha_{3m}^2 - \alpha_{3n}^2} \frac{\alpha_{3n} c_{31m} c_{32n}}{\mu_{r3} \cos(\alpha_{3m} W_3) \cos(\alpha_{3n} W_3)} \\
&\quad + \frac{1}{\alpha_{2m}^2 - \alpha_{2n}^2} \frac{c_{1m} c_{1n}}{\mu_{r1}} [\alpha_{1m} \tan(\alpha_{1n} W_1) - \alpha_{1n} \tan(\alpha_{1m} W_1)] \\
&\quad + \frac{1}{\alpha_{3m}^2 - \alpha_{3n}^2} \frac{c_{4m} c_{4n}}{\mu_{r4}} [\alpha_{4m} \tan(\alpha_{4n} W_4) - \alpha_{4n} \tan(\alpha_{4m} W_4)] \\
&\quad + \frac{1}{\alpha_{3m}^2 - \alpha_{3n}^2} \frac{\alpha_{3m} c_{32m} c_{31n}}{\mu_{r3} \cos(\alpha_{3m} W_3) \cos(\alpha_{3n} W_3)} \\
&\quad - \frac{1}{\alpha_{3m}^2 - \alpha_{3n}^2} \frac{\alpha_{3n} c_{31m} c_{32n}}{\mu_{r3} \cos(\alpha_{3m} W_3) \cos(\alpha_{3n} W_3)} \\
&\quad + \frac{1}{\alpha_{4m}^2 - \alpha_{4n}^2} \frac{c_{4m} c_{4n}}{\mu_{r4}} [\alpha_{4n} \tan(\alpha_{4m} W_4) - \alpha_{4m} \tan(\alpha_{4n} W_4)], \tag{A-15}
\end{aligned}$$

where c_{mn} are coefficients of eigenfunctions in each subregions and they are related by

the boundary conditions between subregions as

$$\begin{aligned}
c_{1m} \tan(\alpha_{1m} W_1) - \frac{c_{21m}}{\cos(\alpha_{2m} W_2)} &= 0 \quad (x = W_1), \\
c_{21m} + c_{22m} \tan(\alpha_{2m} W_2) - \frac{c_{31m}}{\cos(\alpha_{3m} W_3)} &= 0 \quad (x = W_1 + W_2), \\
c_{31m} + c_{32m} \tan(\alpha_{3m} W_3) + c_{4m} \tan(\alpha_{4m} W_4) &= 0 \quad (x = a - W_4), \tag{A-16}
\end{aligned}$$

and eigen values in each subregions α_{im} satisfy the phase continuity across subregions

$$\sqrt{(\alpha_{1m})^2 - \omega^2 \varepsilon_1 \mu_1} = \sqrt{(\alpha_{2m})^2 - \omega^2 \varepsilon_2 \mu_2} = \sqrt{(\alpha_{3m})^2 - \omega^2 \varepsilon_3 \mu_3} = \sqrt{(\alpha_{4m})^2 - \omega^2 \varepsilon_4 \mu_4}. \tag{A-17}$$

(A-15) vanishes to zero after substitution of (A-16) and (A-17).

When $m = n$, eq. (A-3) is not zero.

$$\int_0^a \frac{\{\Phi_m(x)\}^2}{\mu_{ri}} dx \neq 0. \quad (\text{A-18})$$

The value of integral can be unity by determining the coefficients of eigenfunctions

c_{mn} as follows

$$\begin{aligned} & \int_0^a \frac{\{\Phi_m(x)\}^2}{\mu_{ri}} dx \\ &= \int_0^{W_1} \frac{\{\Phi_m(x)\}^2}{\mu_{r1}} dx + \int_{W_1}^{W_1+W_2} \frac{\{\Phi_m(x)\}^2}{\mu_{r2}} dx + \int_{W_1+W_2}^{a-W_4} \frac{\{\Phi_m(x)\}^2}{\mu_{r3}} dx + \int_{a-W_4}^a \frac{\{\Phi_m(x)\}^2}{\mu_{r4}} dx \\ &= \frac{c_{1m}^2}{2\mu_{r1}} \left\{ \frac{W_1}{\cos^2(\alpha_{1m}W_1)} - \frac{\tan(\alpha_{1m}W_1)}{\alpha_{1m}} \right\} \\ &+ \frac{c_{21m}^2}{2\mu_{r2}} \left\{ \frac{W_2}{\cos^2(\alpha_{2m}W_2)} + \frac{\tan(\alpha_{2m}W_2)}{\alpha_{2m}} \right\} + \frac{c_{22m}^2}{2\mu_{r2}} \left\{ \frac{W_2}{\cos^2(\alpha_{2m}W_2)} - \frac{\tan(\alpha_{2m}W_2)}{\alpha_{2m}} \right\} \\ &+ \frac{1}{\mu_{r2}} \frac{c_{21m}c_{22m}}{\alpha_{2m}} \tan^2(\alpha_{2m}W_2) \\ &+ \frac{c_{31m}^2}{2\mu_{r3}} \left\{ \frac{W_3}{\cos^2(\alpha_{3m}W_3)} + \frac{\tan(\alpha_{3m}W_3)}{\alpha_{3m}} \right\} + \frac{c_{32m}^2}{2\mu_{r3}} \left\{ \frac{W_3}{\cos^2(\alpha_{3m}W_3)} - \frac{\tan(\alpha_{3m}W_3)}{\alpha_{3m}} \right\} \\ &+ \frac{1}{\mu_{r3}} \frac{c_{31m}c_{32m}}{\alpha_{3m}} \tan^2(\alpha_{3m}W_3) \\ &+ \frac{c_{4m}^2}{2\mu_{r4}} \left\{ \frac{W_4}{\cos^2(\alpha_{4m}W_4)} - \frac{\tan(\alpha_{4m}W_4)}{\alpha_{4m}} \right\} = 1 \end{aligned} \quad (\text{A-19})$$

All coefficients can be expressed in terms of c_{1m} as

$$c_{21m} = c_{1m} \tan(\alpha_{1m}W_1) \cos(\alpha_{2m}W_2),$$

$$c_{22m} = c_{1m} \frac{\alpha_{1m}\mu_{r2}}{\alpha_{2m}\mu_{r1}} \cos(\alpha_{2m}W_2),$$

$$c_{31m} = c_{1m} \tan(\alpha_{1m}W_1) \cos(\alpha_{2m}W_2) \cos(\alpha_{3m}W_3)$$

$$+ c_{1m} \frac{\alpha_{1m}\mu_{r2}}{\alpha_{2m}\mu_{r1}} \cos(\alpha_{2m}W_2) \tan(\alpha_{2m}W_2) \cos(\alpha_{3m}W_3)$$

$$= c_{1m} \cos(\alpha_{2m}W_2) \cos(\alpha_{3m}W_3) \left\{ \tan(\alpha_{1m}W_1) + \frac{\alpha_{1m}\mu_{r2}}{\alpha_{2m}\mu_{r1}} \tan(\alpha_{2m}W_2) \right\},$$

$$\begin{aligned}
c_{32m} &= -\frac{\alpha_{2m}c_{1m}\mu_{r3}\tan(\alpha_{1m}W_1)\cos(\alpha_{2m}W_2)\tan(\alpha_{2m}W_2)\cos(\alpha_{3m}W_3)}{\alpha_{3m}\mu_{r2}} \\
&\quad + \frac{\alpha_{1m}c_{1m}\mu_{r3}\cos(\alpha_{2m}W_2)\cos(\alpha_{3m}W_3)}{\alpha_{3m}\mu_{r1}} \\
&= c_{1m}\frac{\alpha_{2m}\mu_{r3}}{\alpha_{3m}\mu_{r2}}\cos(\alpha_{2m}W_2)\cos(\alpha_{3m}W_3)\left\{\frac{\alpha_{1m}\mu_{r2}}{\alpha_{2m}\mu_{r1}} - \tan(\alpha_{1m}W_1)\tan(\alpha_{2m}W_2)\right\}, \\
-c_{4m} &= c_{1m}\frac{\cos(\alpha_{2m}W_2)\cos(\alpha_{3m}W_3)}{\tan(\alpha_{4m}W_4)}\left\{\tan(\alpha_{1m}W_1) + \frac{\alpha_{1m}\mu_{r2}}{\alpha_{2m}\mu_{r1}}\tan(\alpha_{2m}W_2)\right\} \\
&\quad + c_{1m}\frac{\alpha_{2m}\mu_{r3}}{\alpha_{3m}\mu_{r2}}\frac{\cos(\alpha_{2m}W_2)\cos(\alpha_{3m}W_3)\tan(\alpha_{3m}W_3)}{\tan(\alpha_{4m}W_4)}\left\{\frac{\alpha_{1m}\mu_{r2}}{\alpha_{2m}\mu_{r1}} - \tan(\alpha_{1m}W_1)\tan(\alpha_{2m}W_2)\right\}.
\end{aligned} \tag{A-20}$$

The above relations are substituted into (A-19) to determine c_{1m} .

Appendix 5 Derivation of eq. (34)

Transformed fields in region (II) are given as [eqs. (28) and (30)]

$$\tilde{E}_m(z) = P_m \frac{\cosh\{\gamma_m(z - z_1)\}}{\cosh(\gamma_m L_s)} + Q_m \frac{\sinh\{\gamma_m(z - z_1)\}}{\sinh(\gamma_m L_s)}, \quad (\text{A-21})$$

$$\tilde{H}_m(z) = \frac{\gamma_m}{j\omega\dot{\mu}_i} \left[P_m \frac{\sinh\{\gamma_m(z - z_1)\}}{\cosh(\gamma_m L_s)} + Q_m \frac{\cosh\{\gamma_m(z - z_1)\}}{\sinh(\gamma_m L_s)} \right]. \quad (\text{A-22})$$

Coefficients P_m and Q_m are obtained in eq. (33), and they are substituted into eqs.

(A-21) and (A-22), then

$$\begin{aligned} \tilde{E}_m(z) = & -\frac{j\omega\dot{\mu}_i}{\gamma_m} \frac{\cosh\{\gamma_m(z - L_s)\}}{\sinh(\gamma_m t)} \int_0^a h_a(x) \frac{\Phi_m(x)}{\mu_i} dx \\ & + \frac{j\omega\dot{\mu}_i}{\gamma_m} \frac{\cosh\{\gamma_m(z - z_1)\}}{\sinh(\gamma_m L_s)} \int_0^a h_b(x) \frac{\Phi_m(x)}{\mu_i} dx, \end{aligned} \quad (\text{A-23})$$

$$\begin{aligned} \tilde{H}_m(z) = & -\frac{\sinh\{\gamma_m(z - z_2)\}}{\sinh(\gamma_m L_s)} \int_0^a h_a(x) \frac{\Phi_m(x)}{\mu_i} dx \\ & + \frac{\sinh\{\gamma_m(z - z_1)\}}{\sinh(\gamma_m L_s)} \int_0^a h_b(x) \frac{\Phi_m(x)}{\mu_i} dx. \end{aligned} \quad (\text{A-24})$$

These transformed fields are transformed inversely by substituting above equations into eqs. (20-a) and (20-b), and electromagnetic fields in region (II) are expressed in terms of aperture magnetic fields as

$$\begin{aligned} E_y^{(II)}(x, z) = & \sum_{m=1}^{\infty} \Phi_m(x) \tilde{E}_m(z) \\ = & -\int_0^a \sum_{m=1}^{\infty} \frac{j\omega\dot{\mu}_i}{\gamma_m} \frac{\cosh\{\gamma_m(z - z_1 - L_s)\}}{\sinh(\gamma_m L_s)} \Phi_m(x) \Phi_m(x') \frac{h_a(x')}{\mu_i} dx' \\ & + \int_0^a \sum_{m=1}^{\infty} \frac{j\omega\dot{\mu}_i}{\gamma_m} \frac{\cosh\{\gamma_m(z - z_2 + L_s)\}}{\sinh(\gamma_m L_s)} \Phi_m(x) \Phi_m(x') \frac{h_b(x')}{\mu_i} dx' \\ = & -\int_0^a Z^{(II)}(x, z | x', z_1) \frac{h_a(x')}{\mu_i} dx' + \int_0^a Z^{(II)}(x, z | x', z_2) \frac{h_b(x')}{\mu_i} dx', \end{aligned} \quad (\text{A-25})$$

$$\begin{aligned}
H_x^{(II)}(x, z) &= \sum_{m=1}^{\infty} \Phi_m(x) \tilde{H}_m(z) \\
&= -\int_0^a \sum_{m=1}^{\infty} \frac{\sinh\{\gamma_m(z - z_1 - L_s)\}}{\sinh(\gamma_m L_s)} \Phi_m(x) \Phi_m(x') \frac{h_a(x')}{\mu_i} dx' \\
&\quad + \int_0^a \sum_{m=1}^{\infty} \frac{\sinh\{\gamma_m(z - z_2 + L_s)\}}{\sinh(\gamma_m L_s)} \Phi_m(x) \Phi_m(x') \frac{h_b(x')}{\mu_i} dx' \\
&= \int_0^a T_m^{(II)}(x, z | x', z_1) \frac{h_a(x')}{\mu_i} dx' + \int_0^a T_m^{(II)}(x, z | x', z_2) \frac{h_b(x')}{\mu_i} dx'. \tag{A-26}
\end{aligned}$$